UNIVERSITY OF CALIFORNIA

Santa Barbara

Sub-Terahertz Traveling-Wave Low-Temperature Grown-GaAs P-I-N Photodetector

By

Yi-Jen Chiu

ECE Technical Report

May 1999

A dissertation submitted in partial satisfaction
of the requirements for the degree of
Doctor of Philosophy

In

Electrical and Computer Engineering

Committee in Charge

Professor John E. Bowers, chairperson
Professor Nadir Dagli
Professor Arthur C. Gossard
Professor Umesh K. Mishra

Sub-Terahertz Traveling-Wave Low-Temperature Grown-GaAs
P-I-N Photodetector

Copyright © by

Yi-Jen Chiu

All rights reserved
May 1999

ACKNOWLEDGEMENTS

This dissertation gives the summary of my research over the past four years. From the first time stay in U.S., I had a very good time doing my graduate work at UCSB. Working with many researchers in this wonderful research environment, I would like to thank for all the people who contributed to this work.

My advisor, Prof. John Bowers, deserves my sincerest thanks for giving me much independence that I could enjoy my research, guiding me to the valuable directions and supporting me with patient encouragement in the years ahead.

I also benefited much from Prof. Arthur C. Gossard for his excellent class, which gave me perspective views on the MBE growth. Professor Umesh K. Mishra gave me some constructive suggestions on the current transport problems. Professor Nadir Dagli helped and conducted me onto the microwave transmission. Discussing with Prof. Mark Rodwell about the EO-sampling measurement gave me more insights on the device performance.

I owed a lot to my co-workers, who directly contributed to this work. I would like to thank Dr. Siegfried B. Fleischer for helping me the EO-sampling measurement and valuable discussion. Dr. Sheng Z. Zhang and Volkan Kaman helped me the 1550nm light measurement on the device and system performance. From Dr. Kirk Giboney, I learned much about the high-speed photodetectors. I'd like to acknowledge the discussion with Dr. James Ibbetson to help me clarify many LT-GaAs material aspects. Working in MBE lab of UCSB, John English's technical help (and sense of humor) teaches me what to do the right things in MBE growth and makes the work more efficiently. Thanks all system-A co-workers (especially Dr. Jack Ko , Dr. Rich Mirin and Ryne Naone) for keeping machine running and sharing the growth experiences.

I am indebted to all the members in Prof. John Bowers's group: Dr. Siegfried B Fleishcer, Dr. Kirk Giboney, Dr. Sheng Zhang, Prof. Chi-Kuang Sun, Bin Liu, Tom Reynolds, Daniel Lasaosa and Gerry Robinson, Dr. Dan Tauber, Dr. Near Marglit, Alexis Black, Adil Karim, Dr. Jaochim Piprek, Dr. Patrick Abraham, Helen Reese, Dr. Ali Shakouri, Dr. Weishu Wu, Dr. Rajeev Ram, Dr. Pat Corvini, and other members. Dairly interaction and weekly meeting help me do the measurement, fabricate device and get many new ideas. Owing to their efforts, the work is successfully done.

I would further thank Dr. Yu-Heng Jan, Dr. Ching-Hui Chen, Dr. Michelle Lee, Dr. Nick Cheng and Bob Hill and James Guthrie for their help in processing, high-speed measurement and friendship.

Finally, I would like to thank my family for the support and encouragement. Without them, I would not have finished this dissertation.

Dedicate to my parents for their love.

VITA

July 1989-June 1991	B.S., Electrical Engineering, National Cheng-Kung University, Tainan, Taiwan
July 1991-June 1993	M.S. Electrical Engineering, National Taiwan University, Taipei, Taiwan
July 1991-May 1993	R.O.C. Army, Officer in Communication
Sep. 1994- May 1999	Ph.D. student in U. of California Santa Barbara

Publication

1. Yi-Jen Chiu; Fleischer, S.B.; Lasaosa, D.; Bowers, J.E. "Ultrafast (370 GHz bandwidth) p-i-n traveling wave photodetector using low-temperature-grown GaAs." *Applied Physics Letters,* vol.71, (no.17), 27 Oct. 1997. p.2508-10

2. Yi-Jen Chiu; Fleischer, S.B.; Bowers, J.E. "High-speed low-temperature-grown GaAs p-i-n traveling-wave photodetector." *IEEE Photonics Technology Letters*, vol.10, (no.7), IEEE, July 1998. p.1012-14.

3. Yi-Jen Chiu, S.Z. Zhang, S. B. Fleischer, J.E. Bowers and U.K. Mishra, "GaAs-based, 1.55 μm high speed, high saturation power, low-temperature grown GaAs p-i-n photodetector," *Electron. Lett.*, vol.34, pp.1253-1255, 1998.

4. Yi-Jen Chiu, S.B. Fleischer and J.E. Bowers, " Subpicosecond (570 fs) response of p-i-n traveling wave photodetector using low-temperatur-grown GaAs," *IEEE Topical Meeting on Microwave Photonics ,*Duisburg/Essen, Germany,1997

5.Yi-Jen Chiu, S.B. Fleischer and J.E. Bowers, "Low-temperature grown GaAs traveling wave pin photodetector with high bandwidth," *IEEE LEOS'97* , San Francisco, Nov. 1997

6 Yi-Jen Chiu, Sheng Z. Zhang, Siegfried B. Fleischer, John E. Bowers and Umesh K. Mishra, "1.55 um absorption, high speed, high saturation power, p-i-n photodetector using low-temperature grown GaAs", *IEEE Topical Meeting on Microwave Photonics*, Paper TuD3, Princeton, New Jersey, 1998.

7. Yi-Jen Chiu, Volkan Kaman, Sheng Z. Zhang, John E. Bowers and Umesh K. Mishra "A novel 1.54 μm n-i-n photodetector based on low-temperature grown GaAs", *IEEE LEOS'98,* Orlando, Florida, 1998

8. Yi-Jen Chiu, Siegfried B. Fleischer, John E. Bowers, Arthur C. Gossard, and Umesh K. Mishra, "High power, high speed, low-temperature -grown GaAs p-i-n traveling wave photodetector", Invited paper, CLEO'98, San Fancisco, 1998

9. J.E. Bowers, Y. Chiu, S.B. Fleischer, and A. Gossard, 'High Power Characteristics of 560 GHz Bandwidth Traveling Wave Photodetectors,' PSAA, Jan. 1998
10. S. Z. Zhang, Y. J. Chiu, P. Abraham and J. E. Bowers, "Polarization-insensitive multiple-quantum-well traveling-wave electroabsorption modulators with 18 GHz bandwidth and 1.2 V driving voltage at 1.55 μm," *IEEE Topical Meeting on Microwave Photonics*, Paper MC2, 1998.
11. Sheng Z. Zhang, Yi-Jen Chiu, Patrick Abraham, and John E. Bowers, "25 GHz polarization-insensitive electroabsorption modulators with traveling-wave electrodes," *IEEE Photon. Technol. Lett*. Vol 11, number 2, p191
12. Sheng Z. Zhang, Volkan Kaman, Patrick Abraham, Yi-Jen Chiu, Adrian Keating, and John E. Bowers, "30 Gbit/s operation of a traveling-wave electroabsorption modulator," submitted to *Optical Fiber Communication Conference*, OFC'99.
13. J.E. Bowers, S.Z. Zhang, P. Abraham, Y-J. Chiu, V. Kaman , 'Low Drive Voltage, High Speed Traveling-Wave Electroabsorption Modulators,' PSAA, February, 1999 University of California, Santa Barbara
14. Holmes, A.L., Jr.; Mirin, R.P.; Chiu, Y.J.; Denbaars, S.P.; Bowers, J.E. "1.55 micron in-plane lasers with p-$Al_{0.7}Ga_{0.3}As$ cladding layers". Conference Proceedings. LEOS '97, 10th Annual Meeting.
15. Margalit, N.M.; Black, K.A.; Chiu, Y.J. ; Hegblom, E.R.; Streubel, K.; Abraham, P.; Anzlowar, M.; Bowers, J.E.; Hu, E.L, "Top-emitting double-fused 1.5 mu m vertical cavity lasers". *Electronic Letters*, vol.34, (no.3), IEE, 5 Feb. 1998. p.285-7.
16. Margalit, N.M.; Streubel, K.; Chiu, Y.; Hegblom, E.R.; Hou, H.Q.; Bowers, J.E.; Hu, E.L. "High-temperature 1.55 mu m vertical-cavity lasers through wafer fusion". Proceedings of the SPIE - The International Society for Optical Engineering, vol.3003, (Vertical-Cavity Surface-Emitting Lasers, San Jose, CA, USA, 13-14 Feb. 1997.) SPIE-Int. Soc. Opt. Eng, 1997. p.169-75.
17. Margalit, N.; Yijen Chiu; Hegblom, E.; Abraham, P.; Black, A.; Wesselmann, J.; Bowers, J.E.; Hu, E.L.; Streubel, K. "120 degrees C pulsed operation from a 1.55 mu m vertical-cavity laser". 1997 Digest of the IEEE/LEOS Summer Topical Meetings
18. N. Margalit, Y.J. Chiu, E. Hegblom, P. Abraham, K.A. Black, J. Wesselman, J.E. Bowers and E.L. Hu, "Vertical cavity surface emitting lasers". Mini-symposium on Devices and Systems for optical interconnects and Data link, Grasmere, England Sep. 1-4, 1997

20. N. Margalit, Y.J. Chiu, J.E. Bowers and E.L. Hu, "Long wavelength vertical-cavity lasers through wafer fusion.", CLEO Pacific Rim'97 , Chiba, Japan, July 14-18

21. K.A. Black, N.M. Margalit, E.R. Hegblom, P. Abraham, Y-J Chiu , J. Piprek, J.E. Bowers, and E. L. Hu, " Double-fused 1.5μm vertical cavity lasers operating continuous wave up to 71°C", IEEE 16th International Semiconductor Laser Conference, Oct. 4-8 1998

22.Black, K.A.; Abraham, P.; Margalit, N.M.; Hegblom, E.R.; Chiu, Y.-J.; Piprek, J.; Bowers, J.E.; Hu, E.L. "Double-fused 1.5 mu m vertical cavity lasers with record high T/sub o/ of 132 K at room temperature [Al(Ga)As/GaAs]. Electronics Letters, vol.34, (no.20), IEE, 1 Oct. 1998. p.1947-9

23. Black, K.A.; Margalit, N.M.; Hegblom, E.R.; Abraham, P.; Chiu, Y.-J.; Piprek, J.; Bowers, J.E.; Hu, E.L. "Double-fused 1.5 mu m vertical cavity lasers operating continuous wave up to 71 degrees C". (Conference Digest. ISLC 1998 NARA. 1998 IEEE 16th International Semiconductor Laser Conference (Cat. No. 98CH361130), Conference Digest. ISLC 1998 NARA. 1998Nara, Japan, 4-8 Oct. 1998.) New York, NY, USA: IEEE, 1998. p.247-8.

25 A. Keating, A. Black, A. Karim, Y.-J. Chiu, P. Abraham, C. Harder1, E. Hu and J. Bowers "High temperature, optically pumped, 1.55 mm VCSEL operating at 6 Gb/s", DRC of 1999

26 P. Abraham, K.A. Black, A. Karim, J. Piprek, Y.J. Chiu, B. Liu, A. Shakouri, S.K. Mathis, E.L. Hu, J.E. Bowers, "VCSEL and High-Performance Photonics Enabled by Wafer Bonding", International Symposium on Semiconductor Wafer Bonding Science, Technology and Applications (October 17-22, 1999, Honolulu, Hawai).

27. B. Liu, A. Shakouri, P.Abraham, Y.J. Chiu, S. Zhang, and J.E. Bowers, " InP/GaAs fused vertical coupler filters". *IEEE LEOS'98,* Orlando, Florida, 1998

28. B. Liu, A. Shakouri, P.Abraham, Y.J. Chiu, S.Zhang, and J.E. Bowers, "Fused InP-GaAs vertical coupler filters". *IEEE Photonics Technology Letters*, vol.11, (no.1), Jan. 1999. p-93-95

29. B. Liu; Shakouri, A.; Abraham, P.; Chiu, Y.J.; Bowers, J.E. "Fused III-V vertical coupler filter with reduced polarisation sensitivity". Electronics Letters, vol.35, (no.6), IEE, 18 March 1999. p.481-2.

30. Ching-Hui Chen; Yi-Jen Chiu; Hu, E.L. "Characterization of the radiation-enhanced diffusion of dry-etch damage in n-GaAs". vol.15, (no.6) *Journal of Vacuum Science & Technology B* (Microelectronics and Nanometer Structures), , 1997. p.2648-51. 20 references.

31. H. Reese, Y.J. Chiu, A. Shakouri, E. Hu, and J.E. Bowers " Wet Oxidation of low temperature $Al_{0.98}Ga_{0.02}As$," *EMC'97,* Fort Collins, CO, June 25-27 1997

32. H. Reese, Y.J. Chiu, E. Hu, " Low temperature grown GaAs enhanced wet thermal oxidation of $Al_{0.98}Ga_{0.02}As$ ", Applied Physics Lett.Vol73, No. 18, Nov.2 , p2624 1998

33. Ali Shakouri, Chris LaBounty, Patrick Abraham, Yi-Jen Chiu and John E. Bowers, ' Temperature dependence of thermionic emission cooling in single barrier and superlattice heterostructure'. *EMC'99*, Santa Barbara , CA, June 30-July 2, 1999.

34. M. Kozhevnikov, V. Narayanamurti, C. Zheng, Yi-jen Chiu and D.L. Smith, 'Effect of electron scattering on second derivative ballistic electron emission spectroscopy in Au/GaAs/AlgaAs heterostructures'. *Physic Review Letters*, Vol. 82, No. 18, p3677, 1999

Abstract

Sub-Terahertz Traveling-wave Low-Temperature Grown-GaAs P-I-N Photodetector

by

Yi-Jen Chiu

High-speed photodetectors are very important components for fiber communication. In conventional photodetectors, the bandwidth is limited by the carrier transit time across the intrinsic region. As the transit time decreases by thinning intrinsic region, the higher RC roll-off frequency, however, limits the device speed. The inevitable trade-off between RC-circuit and carrier transit time limits this kind of photodetector bandwidth. Although the traveling wave photodetector (TWPD) can overcome the RC-imposed limitation by impedance and velocity matching, the design of the intrinsic region is restricted by the geometry of transmission line. By using low-temperature grown GaAs (LT-GaAs), the material response is dominated by the carrier-trapping instead of carrier-transit time. The design of material limits to bandwidth can thus be independent from the RC-distributed effects. In this dissertation, a novel p-i-n photodetector incorporating the LT-GaAs and TWPD circuit structure is demonstrated. The performance is found to be enhanced by the taking advantage of LT-GaAs and TWPD structure.

A distributed photodetector model is used to optimize and design the waveguide structure. The microwave loss and dispersion, velocity mismatcing, and the microwave reflection on waveguide are considered in this model. An equivalent circuit model is used to calculate the properties of microwave propagation. The optimum performance can be achieved at the impedance matching, velocity matching and the low loss microwave transmission.

An impulse response with 530 fs FWHM is measured by an electro-optic sampling technique. The corresponding –3dB bandwidth is as high as 560GHz. The optical power dependent and bias dependent measurement reveals that the high-speed performance is mainly attributed to the short carrier trapping time in LT-GaAs.

Long wavelength (1300nm~1550nm) light can be absorbed in the LT-GaAs due to the subbandgap defects and As precipitates. An LT-GaAs waveguide photodetector is used to improve the quantum efficiency by increasing the device length. High speed (18GHz bandwidth) with 1% quantum efficiency was demonstrated at long wavelength absorption on GaAs-based material. This opens up the possibility for long wavelength communication using AlGaAs material.

Outline

Chapter 1 Introduction	1
1.1 Background	1
1.2 Bandwidth limitation	5
1.3 Organization of the Dissertation	12
Chapter 2 Theory and distributed photocurrent model	17
2.1. Model to calculate the bandwidth limitation	17
2.2 Summary	45
Chapter 3 Device design and fabrication	47
3.1 TWPD circiut design	48
3.2 Material design	58
3.3 Device fabrication	66
3.4 Summary	75
Chapter 4 Experiment results and discussion	79
4.1 The p-i-n waveguide characteristics	79
4.2 High speed measurement of photodetectors	90
4.3 Bias dependence response	111
4.4 The power dependence response	112
4.5 Summary	115

Chapter 5 Long wavelength detection 119
- 5.1 Characteristics of short length device 121
- 5.2 Long device performance 125
- 5.3 Bias dependent efficiency 127
- 5.4 Carrier transport effects at high electric field 129
- 5.5 Discussion and summary 132

Chapter 6 Conclusion 135
- 6.1 Summary 135
- 6.2 Future work 137
- 6.3 Applicatoin 141

Chapter 1

Introduction

1.1 Background

The demand in the speed and capacity of information processing has been increasing higher and higher. Optical fiber communication systems will be required to have a high capacity of information transmission. Therefore, optoelectronic devices used in communication systems must keep the pace with this requirement or be developed even further. Various techniques for optical fiber and wireless communication links, an example shown in Figure 1.1, have been widely used [1~5]. In optical fiber transmission systems, bit rates with Tera-bits/s have been demonstrated [6] by using WDM (wavelength division multiplexing) or OTDM (optical time division multiplexing) techniques. The performance of optoelectronic devices, like photodetectors, lasers and modulators, are challenged by the demands of optical fiber links. This increases the need for higher bandwidth optoelectronic instruments.

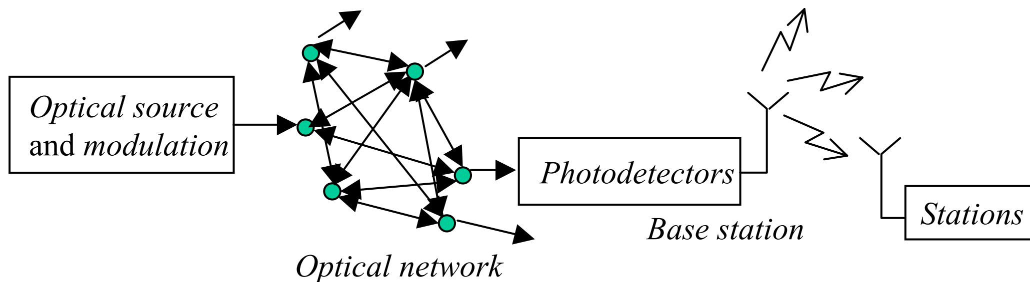

Figure 1.1. The schematic diagram of optical fiber and microwave links

High-speed photodetectors are needed in optical fiber communication links. As shown in Figure 1.2, photodetectors are capable of transferring the time-modulated optical power ($P_{optical}(A.C.)$) to the microwave power ($P_{R.F.}$). The

transfer function is expressed as Equation 1.1. Based on the linear operation, the input optical power ($P_{optical}(A.C.)$) reveals a quadratic relation to the output microwave power ($P_{R.F.}$).

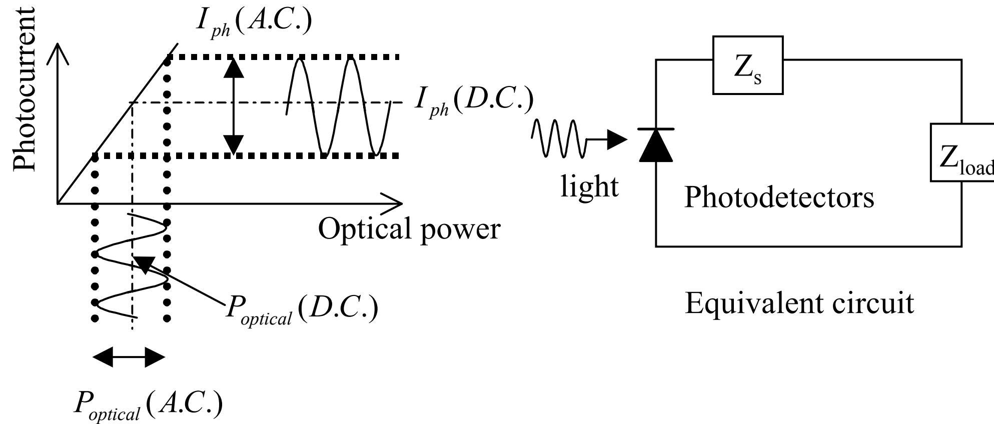

Figure1.2. The transfer of optical power to microwave power

$$P_{R.F.} = \frac{\eta_{ext}{}^2 \cdot P_{optical}{}^2(A.C.)}{16} \cdot \left(\frac{Z_{load}}{Z_{load} + Z_s}\right) \qquad (1.1)$$

Typically, there are three aspects for measuring photodetectors, namely (1) *broad bandwidth* (2) *high efficiency* and (3) *high saturation power*. (1) *The broad bandwidth* photodetectors are capable of responding to high optical modulation rates. (2) A detector with *high efficiency* (η_{ext}) can convert a high portion of optical power to electrical current. Due to the limitation of the instrument sensitivity, highly efficient photodetectors are necessary. (3) To get high RF gain, increase the signal-to-noise ratio or obtain a large spurious-free dynamic range, photodetectors should be operated at high saturation power, i.e. photodetectors can sustain a high optical power without distorting the output electrical signal. Photodetectors with low efficiency can be pumped with high optical power to get a high current.

High-speed photodetectors have been developed in the past few decades. Due to the bandgaps, the wavelength dependence of absorption is quite different for different materials. Generally, it can be divided into two kinds of material for high speed performance, GaAs for below 870nm light (short wavelength) and InGaAs for 1300 nm ~1600 nm light (long wavelength). Since 1980, the claimed record bandwidths of photodetectors are described below. And Figure 1.3 summarizes the bandwidths as a function of years published.

In short wavelength regime : In 1983, Wang and Bloom [7], reported the first GaAs Schottky photodiode above 100 GHz bandwidth. By combining the GaAs Schottky photodiode and sampler circuits, Li and Ozbay [8], in 1991, reported performance with bandwidth higher than 150 GHz. Using LT-GaAs material and a MSM structure, Chen et. al. [9] in 1991 and Chou et. al. [10] in 1992 reported 375 and 510 GHz bandwidth of photodetectors respectively. In 1995, Giboney et. al. demonstrated a 176 GHz bandwidth photodetector using a traveling wave structure. In 1998, we reported a p-i-n LT-GaAs photodetector with 560GHz –3dB bandwidth [12].

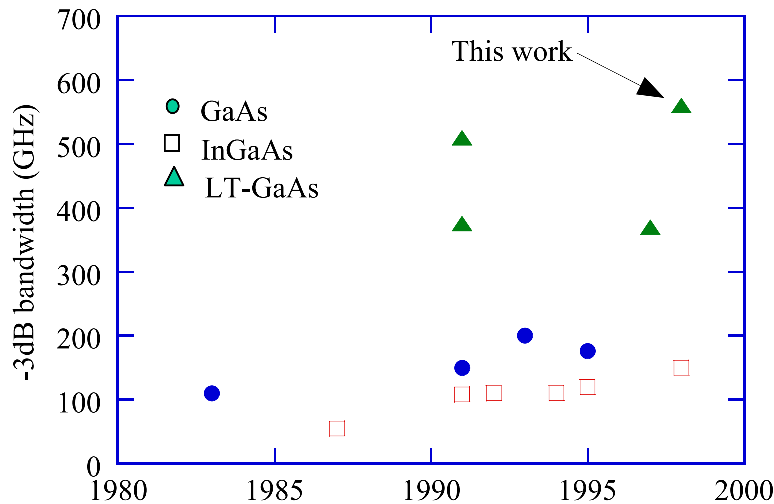

Figure 1.3. The recorded -3dB bandwidths of photodetectors since 1983.

In the long wavelength regime : Bowers and Burrus [13] reported an InGaAs p-i-n photodetector with a bandwidth above 50 GHz in 1987. In 1990, Wey et al. [14] reported a 16 ps response instrument limited photodiode. Also, in 1991, Wey et al. [15] demonstrated the first long wavelength photodetector above 100 GHz bandwidth, in which the double graded layers were used to improve the device speed. In 1994, Kato et. al. [16] reported a 110 GHz bandwidth of mushroom type waveguide photodetector. Using air-bridge and undercut mesa to reduce the RC-time constant, in 1995, Tan et. al. [17] reported a 120 GHz bandwidth p-i-n photodetector. In 1998, Shimizu et. al. [18] used a uni-taveling-carrier technique to enhance the bandwidth up to 150 GHz.

Figure 1.3 historically plots the advance of –3dB bandwidths of recorded photodetectors since 1983. With the general semiconductor materials (GaAs or InGaAs), the speed is always limited by the carrier transit time, while the photodetector circuit is optimized by either RC-time constant or traveling wave structures [11,13,17]. The intrinsic capacitance and transit time should be minimized to improve the device speed. However, the trade-off between the carrier-transit time and the intrinsic capactance makes the photodector speed hard to overcome 200 GHz. On the other hand, as shown in figure 1.3, the LT-GaAs material photodetectors statistically show 200~300GHz of bandwidth larger than the general GaAs (circle) and InGaAs (square) photodetectors. The success in using LT-GaAs is based on the short carrier trapping time (< 1ps) in the material itself. With high carrier recombination rate of the material, the circuit effects on photodetectors can be minimized independently from the material response. Consequently, with optimal design in circuits, the detectors can be made by carrier trapping time limitation [12]. Several high speed photodetectors have been shown with bandwidths above 500 GHz or have been demonstrated with THz radiation using low-temperature grown GaAs (LT-GaAs) [9,10,12,19]. The one drawback of the LT-GaAs photodetector is its relatively low quantum efficiency [10,12,20],

because the high portions of carriers are lost by the high carrier-trapping rate. However, from the power dependent measurement [21,22], it was found that LT-GaAs can have higher saturation power over general GaAs, in which the low efficiency can be compensated by higher pumping power.

By distributing the RC elements and impedance matching to external circuits, the edge-couple traveling-wave p-i-n and MSM type photodetectors [11,20] overcome the limitation due to the trade-off between speed and efficiency in vertical illumination type. In this dissertation, we optimized the device structure by incorporating the LT-GaAs and traveling-wave structure [11,12]. The performance of a novel photodetector is demonstrated with a recorded bandwidth (560 GHz). It reveals that LT-GaAs material for the application of above 500 GHz bandwidth communication is plausible.

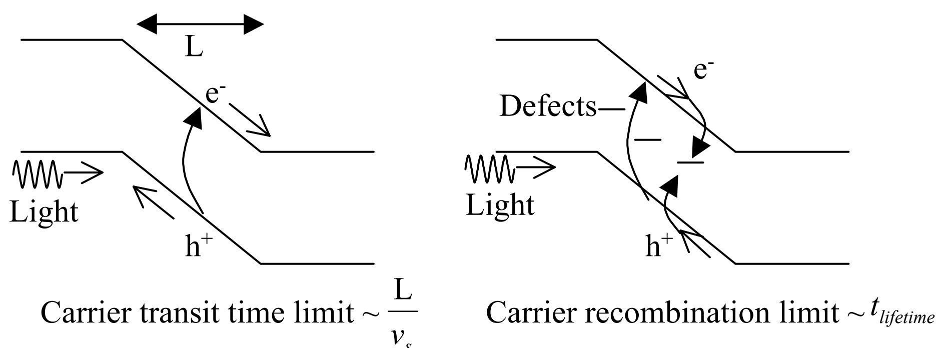

Carrier transit time limit $\sim \frac{L}{v_s}$ Carrier recombination limit $\sim t_{lifetime}$

Figure 1.4. The schematic diagram of carrier transit and recombination limits

1.2 Bandwidth limitation

1.2.1 Material and circuit effects

Theoretically, there are two aspects in determining the high-speed performance of photodetectors, namely the *material* (the conduction current) and *circuit* responses. Because the photocurrent is generated in the intrinsic region, the two main responses can be represented by Equation 1.2 [24]. (the photocurrent density $J_{\mathrm{int}rinsic}$):

$$J_{\text{intrinsic}}(t) = \frac{1}{L}\int_L [J_{conduction}(t) + \frac{\partial}{\partial t}(\varepsilon \cdot E(t))] \quad (1.2)$$

where L: intrinsic region thickness. $\frac{\partial}{\partial t}(\varepsilon E(t))$ is the displacement current. $J_{conduction}$ is the photocarriers conduction current which is the *material* response. With the optical impulse excitation, to get a high speed response of $J_{conduction}$, the excess photocarriers should be swept out by the strong electric fields built-up in the intrinsic region (left of figure 1.4.) or should be removed by the recombination centers in the material (right of figure1.4.). The limitation in the first case is dominated by the carrier transit time across the intrinsic region. The other is by the carrier recombination limitation (right of figure1.4.).

When the optical power is modulated in time, the charge and discharge processes ($\frac{\partial}{\partial t}(\varepsilon E(t))$ on the intrinsic capacitance will involve the photodetector response in equation 1.2). The intrinsic capacitance combining with the parasitic capacitance and inductance of metalization surrounding the photodetectors forms the overall *circuits*. These circuit effects depend on the geometry of photodetector, i.e. the RC time constant or the microwave distributed effects.

1.2.2 Photodetector structures:

Figure 1.5 (top) schematically plots a common vertical-illuminated p-i-n photodetector (VP) and the corresponding equivalent circuit. The incident optical power is perpendicular to the detector plan. Assuming the carrier recombination rate is much lower than carrier transit time, the speed limitation due to the material response can be given by [13] :

$$f_{transit} \approx 0.5 \cdot \frac{v_s}{\text{L}} \quad (1.3)$$

where v_s is the saturation velocity. Obviously, the shorter depletion region (L is small) can obtain a higher transit limit. The external quantum efficiency η_{ext} of this structure is expressed by [13]:

$$\eta_{ext} \propto (1-\exp(-\Gamma \alpha L)) \qquad (1.4)$$

where Γ is the optical modal confinement factor, α : optical absorption coefficient. Γ can be assumed as one in the vertical-illumination. Equation 1.4 gives the fraction of optical power absorbed in the intrinsic region. According to equation 1.3, in the general material (GaAs, InGaAs), the intrinsic region should be less than 0.3 μm to get above 100 GHz (the saturation velocity < $7\times10^{6} cm/\sec$). However, less than 30% of light is absorbed in the intrinsic region according to Equation 1.4. ($\alpha \approx 0.7\mu m^{-1}$ for InGaAs and $\alpha \approx 1\mu m^{-1}$ for GaAs). In order to get high speed, a photodetector has to be thin, but the efficiency will be reduced since $\alpha \cdot L << 1$. Due to this trade-off, the bandwidth-efficiency product of VP is limited. The limitation is expressed as:

$$f_{transit} \cdot \eta_{ext} \approx 0.5 \cdot v_s \cdot L \qquad (1.5)$$

The product is about 40 GHz in GaAs and 30 GHz in InGaAs [13,17,18]. Although the avalanche photodetector can improve this product by current gain, its speed is still limited to 20 GHz by the avalanche built time [27,28].

As shown in Figure 1.5, both p-i-n and MSM vertical-illumination photodetectors have similar equivalent circuits. R is the series resistance including the semiconductor's and the metal's resistivities. C is the intrinsic capacitance ($\mathrm{C} = \varepsilon \cdot \mathrm{A/L}$ in p-i-n structure and $\mathrm{C} = a \cdot \varepsilon \cdot \mathrm{A/S}$, ε is the dielectric constant of intrinsic region, A is the device area, S is the electrode separation of MSM, *a* is some constant related to the electrode width and separation in MSM). The corresponding RC-lump limitation is :

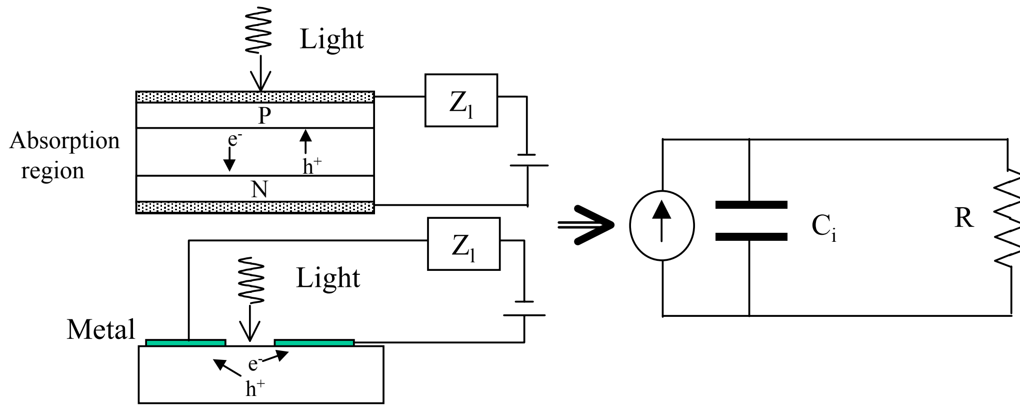

Figure 1.5. The schematic plots of top-illumination photodetectors (p-i-n and MSM) and the equivalent circuit model

$$f_{RC} = \frac{1}{2\pi \cdot \mathrm{RC}} \propto \mathrm{L} \quad \text{(or S in MSM)} \tag{1.6}$$

Compared to equation 1.3, the RC-lump limitation inevitably trades-off with the transit limit in the vertical-illumination type.

The waveguide photodetector (WGPD) structure is designed to improve the bandwidth-efficiency product. Figure 1.6 plots the schematic diagram of waveguide structures in p-i-n or MSM. The optical waveguide is formed by the absorption material, which is surrounded by the low refractive index and transparent cladding layers. As shown in Figure1.6, the edge-coupled optical power is absorbed either in the peak of the optical guiding mode (p-i-n) or the tailor of mode (MSM). Since the direction of optical wave transmission is perpendicular to the carrier transit, the efficiency (Equation 1.4) and the transit limit (Equation 1.3) can be determined separately. So, the bandwidth-efficiency product can be improved. The p-i-n and MSM waveguide photodetectors [11,16,29] have achieved high bandwidth and have overcome the limitation of the bandwidth-efficiency product in the vertical-illumination type (30 GHz for InGaAs, 40 GHz for GaAs).

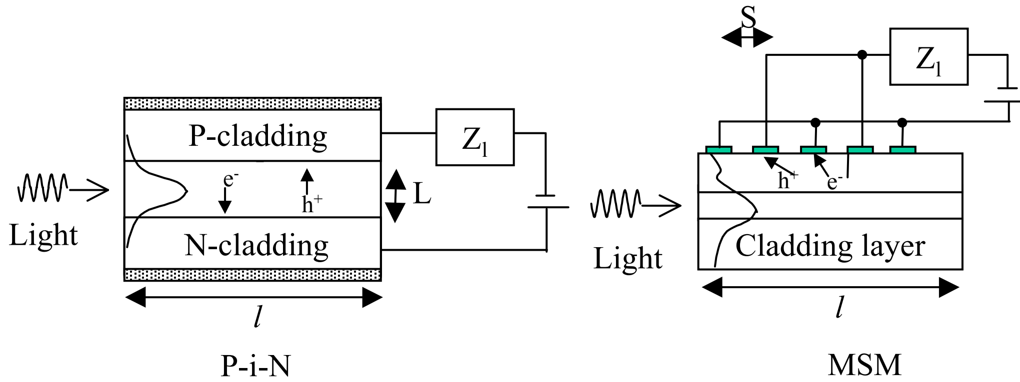

Figure 1.6. The schematic plots of p-i-n (left) and MSM (right) waveguide photodetectors (WGPD)

As for the electrical waves generated in WGPD, Figure 1.7 plots the schematic diagram. Optical wave propagates through the p-i-n structure and excites the distributed photocurrent along the waveguide, over which the electrical wave transmits. Therefore the optical and electrical waves interact along the transmission line. The characteristic impedance in the WGPD structure is generally not matched to the output load circuits. The resultant microwave signal is formed by the high multi-reflections on the both ends of the waveguide, so that the RC-lump effects influence the total response. Consequently, the speed of WGPD depends on the sizes of photodetectors.

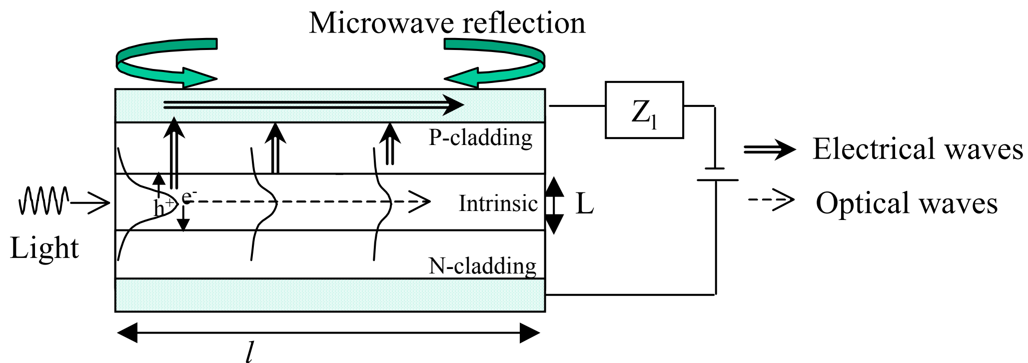

Figure 1.7. The schematic plots of distributed microwave generated by optical wave in waveguide photodetectors (WGPD).

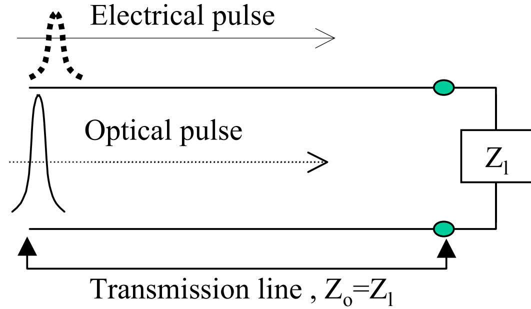

Figure 1.8 . The schematic plot of traveling wave photodetector. The transmission line is designed to match to output circuit.

The traveling–wave photodetector (TWPD) structure is a fully distributed type, which is designed to optimize the waveguide photodetectors. By distributing the RC elements on the transmission line and matching characteristic impedance to the loaded circuits, there are no reflection waves feeding back to the output load circuit to slow the output signal, thus the RC-lump element can be eliminated. Furthermore, by matching the electrical velocity on the transmission line to the optical velocity, the pulse broadening due to walk-off problems is avoided. In principle, without considering the material response and loss in the transmission line, the electrical pulses from the TWPD will resemble the optical pulse, and hence the electrical bandwidth can be made as high as possible. In the practical view, however, the ideal TWPD can not be made due to the inherent dispersion and loss in microwave transmission line, i.e. the impedance and velocity mismatching depends on the frequency. In contrast to the RC limitation, to design a high speed TWPD, the effects of the microwave transmission line and the optical absorption coefficient need to be optimized (chapter 2 and chapter 3).

Historically, the TWPD concept was proposed in 1990 [30], in which the phase matching between the optical and electrical waves was mentioned. In [31], a velocity match structure is made by the p-i-n slow waveguide, and also a transmission line model for distributed photodetectors is used. Unfortunately, the experiment didn't fit the theory and the measured bandwidth is only 4.8 GHz,

which is quite slower than other types of photodetectors. Bottcher et al. [32,33] proposed the distributed theory and the fabrication of the interdigital-MSM slow wave waveguide to analyze the distributed traveling wave photodetector. However, only 78 GHz bandwidth was obtained [29].

In 1994 at UCSB, Giboney et. al. [11] demonstrated the first traveling wave photodetector with an approximately 174 GHz bandwidth and a 76 GHz bandwidth-efficient product. The speed is limited by the carrier transit limitation, and bandwidth-efficiency product significantly overcames the limitation (40 GHz, equation 1.5). In this device, the carrier transit limitation ($\propto 1/L$, L: intrinsic region thickness) is still related to other parameters influencing the bandwidth performance, such as the intrinsic capacitance. The speed is still hard to overcome 200 GHz.

The advantage of LT-GaAs is the high carrier-trapping rate. Using this carrier trapping time limited material, the design of bandwidth due to the intrinsic region thickness (carrier transit effect, L) can be separated. At UCSB, we designed a novel type p-i-n LT-GaAs TWPD. Compared to the GaAs TWPD, the speed is enhanced by about 3 times. The distributed photodetectors model in the frequency domain is used to realize the LT-GaAs TWPD performance. It has been found that the bandwidth limitation is due to short carrier trapping time in the LT-GaAs. Furthermore, the power-dependent measurement reveals that LT-GaAs has a higher saturation power, in which the photocurrent can be compensated by the higher optical power without sacrificing bandwidth performance. The experimental results show that the performance of LT-GaAs TWPD is enhanced by taking advantage of both the short carrier lifetime and the TWPD structure. On the other hand, due to the midgap defects and As-precipitates, LT-GaAs is capable to absorb the long wavelength light (1.3~1.6 μm). The first high-speed 1.55 μm LT-GaAs photodetector is then fabricated. The measured bandwidth (about 18 GHz) and considerably high efficiency (~1%) shows that this kind of detectors has opened a

possibility for the application of long wavelength communication on GaAs-based material.

1.3 Organization of the Dissertation

This dissertation covers the theory of device design, the fabrication of traveling-wave photodetectors and analysis of EO-sampling results and long-wavelength absorption.

Chapter one provides the motivation and background of this work. Comparing the speed and efficiency of other structures of photodetectors, the concept of LT-GaAs traveling wave photodetector is thus followed.

Chapter two gives the theory of the traveling wave photodetector. A distributed photodetector model (in frequency domain) is used to analyze the response. The electrical wave characteristics are extracted from the equivalent circuit model of the transmission line. The total response includes the velocity mismatch, lossy transmission line effects and the reflection on the boundaries.

Chapter three presents the design and fabrication of the TWPD. By the practical view in the processing and measurement, the geometry of the TWPD (waveguide width, length and depletion thickness) is optimized for the design. The electro-optic sampling (EO) measurement and the fabrication process are also explained.

Chapter four gives the measurement results. First, the D.C. measurement and network analyzer are used to characterize a p-i-n waveguide. The loss and dispersion properties of the waveguide are addressed. Second, the impulse response is measured and characterized by EO-sampling techniques on $LiTaO_3$ crystal. The transmission line properties are extracted by two different lengths of devices and agree with the theoretic prediction. In contrast to general photodetectors, the bias and power dependent measurement exhibits a different behavior. All the EO-sampling (power and bias dependent measurement) results

indicate that the high speed is attributed to the high carrier recombination rate in LT-GaAs.

Chapter five presents the measurement on the long wavelength regime. LT-GaAs can absorb 1.55 μm light due to the midgap defects and As-precipitates. The D.C. photocurrent on different lengths of devices are measured to obtain optical absorption length. A high-speed (above 20 GHz) measurement by an optical component analyzer is obtained. Owing to low absorption coefficient, the frequency response shows a linear dependence on input optical power level (high unsaturated properties). To increase quantum efficiency, a n-i-n structure is also proposed.

Reference:

(1)Schmuck, H.; Heidemann, R. 'High capacity hybrid fibre-radio field experiments at 60 GHz'. Technical Digest. Proceedings of International Topical Meeting on Microwave Photonics, Kyoto, Japan, IEEE, p.65-8. 1996.

(2)Wake, D.; Lima, C.R.; Davies, P.A. 'Transmission of 60-GHz signals over 100 km of optical fiber using a dual-mode semiconductor laser source'. IEEE Photonics Technology Letters, vol.8, (no.4), IEEE, April 1996. p.578-80.

(3)Boch, E. 'High bandwidth MM-wave indoor wireless local area networks'. Microwave Journal, vol.39, (no.1), p.152-158, Jan. 1996.

(4)Braun, R.-P.; Grosskopf, G.; Heidrich, H.; von Helmolt, C.; Kaiser, R.; Kruger, K.; Kruger, U.; Rohde, D.; Schmidt, F.; Stenzel, R.; Trommer, D. 'Optical microwave generation and transmission experiments in the 12- and 60-GHz region for wireless communications'. IEEE Transactions on Microwave Theory and Techniques, vol.46, (no.4), IEEE, p.320-30 April 1998..

(5)Smith, G.H.; Novak, D. 'Full-duplex fiber-wireless system using electrical and optical SSB modulation for efficient broadband millimeter-wave transport'. Proceedings of 1997 International Topical Meeting on Microwave Photonics, Germany, 3-5 Sept. p.223-6, 1997.

(6)Onaka, H.; Miyata, H.; Ishikawa, G.; Otsuka, K.; Ooi, H.; Kai, Y.; Kinoshita, S.; Seino, M.; Nishimoto, H.; Chikama, T. '1.1 Tb/s WDM transmission over a 150 km 1.3 μm zero-dispersion single-mode fiber. Optical Fiber Communication Conference. Vol.2 1996 Technical Digest Series. San Jose, CA, USA, p.403-6, 1996..

(7)Wang, S.Y.; Bloom, D.M. '100 GHz bandwidth planar GaAs Schottky photodiode'. Electronics Letters, vol.19, (no.14), 7 July 1983.
(8) Ozbay, E.; Li, K.D.; Bloom, D.M. '2.0 ps, 150 GHz GaAs monolithic photodiode and all-electronic sampler'. IEEE Photonics Technology Letters, vol.3, (no.6), June 1991. p.570-2.
(9)Yi Chen; Williamson, S.; Brock, T.; Smith, F.W.; Calawa, A.R. '375-GHz-bandwidth photoconductive detector'. Applied Physics Letters, vol.59, (no.16), 14 Oct. 1991. p.1984-6.
(10)Chou, S.Y.; Liu, M.Y. 'Nanoscale tera-hertz metal-semiconductor-metal photodetectors'. IEEE Journal of Quantum Electronics, vol.28, (no.10), Oct. 1992. p.2358-68.
(11)Giboney, K.S.; Nagarajan, R.L.; Reynolds, T.E.; Allen, S.T.; Mirin, R.P.; Rodwell, M.J.W.; Bowers, J.E. 'Travelling-wave photodetectors with 172-GHz bandwidth and 76-GHz bandwidth-efficiency product '. IEEE Photonics Technology Letters, vol.7, (no.4), April 1995. p.412-14.
(12)Yi-Jen Chiu; Fleischer, S.B.; Bowers, J.E. 'High-speed low-temperature-grown GaAs p-i-n traveling-wave photodetector'. IEEE Photonics Technology Letters, vol.10, (no.7), IEEE, July 1998. p.1012-14.
(13)Bowers, J.E.; Burrus, C.A., Jr. 'Ultrawide-band long-wavelength p-i-n photodetectors'. Journal of Lightwave Technology, vol.LT-5, (no.10), Oct. 1987. p.1339-50.
(14) Crawford, D.L.; Wey, Y.G.; Mar, A.; Bowqers, J.E.; Hafich, M.J.; Robinson, G.Y. 'High speed InGaAs/InP p-i-n photodiodes fabricated on a semi-insulating substrate. IEEE Photonics Technology Letters, vol.2, (no.9), Sept. 1990. p.647-9.
(15)Wey, Y.G.; Crawford, D.L.; Giboney, K.; Bowers, J.E.; Rodwell, M.J.; Silvestre, P.; Hafich, M.J.; Robinson, G.Y. 'Ultrafast graded double-heterostructure GaInAs/InP photodiode'. Applied Physics Letters, vol.58, (no.19), 13 May 1991. p.2156-8.
(16)Kato, K.; Kozen, A.; Muramoto, Y.; Itaya, Y.; Nagatsuma, T.; Yaita, M. '110-GHz, 50%-efficiency mushroom-mesa waveguide p-i-n photodiode for a 1.55-μm wavelength '. IEEE Photonics Technology Letters, vol.6, (no.6), June 1994. p.719-21.
(17)I-Hsing Tan; Chi-Kuang Sun; Giboney, K.S.; Bowers, J.E.; Hu, E.L.; Miller, B.I.; Capik, R.J. '120-GHz long-wavelength low-capacitance photodetector with an air-bridged coplanar metal waveguide'. IEEE Photonics Technology Letters, vol.7, (no.12), IEEE, Dec. 1995. p.1477-9.
(18)Shimizu, N.; Watanabe, N.; Furuta, T.; Ishibashi, T. 'InP-InGaAs uni-traveling-carrier photodiode with improved 3-dB bandwidth of over 150 GHz '. IEEE Photonics Technology Letters, vol.10, (no.3), IEEE, March 1998. p.412-14.

(19)Brown, E.R.; McIntosh, K.A.; Nichols, K.B.; Dennis, C.L. ‘Photomixing up to 3.8 THz in low-temperature-grown GaAs’. Applied Physics Letters, vol.66, (no.3), 16 Jan. p.285-7,1995.

(20)Lin, L.Y.; Wu, M.C.; Itoh, T.; Vang, T.A.; Muller, R.E.; Sivco, D.L.; Cho, A.Y. ‘Velocity-matched distributed photodetectors with high-saturation power and large bandwidth’. IEEE Photonics Technology Letters, vol.8, (no.10), IEEE, Oct. 1996. p.1376-8.

(21)Yi-Jen Chiu; Fleischer, S.B.; Bowers, J.E.; Gossard, A.C.; Mishra, U.K. ‘High-power, high-speed, low-temperature-grown GaAs p-i-n traveling-wave photodetector’. Technical Digest Summaries of papers presented at the Conference on Lasers and Electro-Optics Conference Edition. 1998 Technical Digest Series, Vol.6, San Francisco, CA, p.501-2, 1998.

(22)Giboney, K.S.; Rodwell, M.J.W.; Bowers, J.E. ‘Traveling-wave photodetector design and measurements’. IEEE Journal of Selected Topics in Quantum Electronics, vol.2, (no.3), Sept. 1996. p.622-9.

(23) Harmon, E.S.; Melloch, M.R.; Woodall, J.M.; Nolte, D.D.; Otsuka, N.; Chang, C.L. ‘Carrier lifetime versus anneal in low temperature growth GaAs’. Applied Physics Letters, vol.63, (no.16), 18 Oct. 1993. p.2248-50

(24) Sze, S.M. ‘Physics of semiconductor devices’ 2nd edition.

(25) Bowers, J.E.; Burrus, C.A. High-speed zero-bias waveguide photodetectors. Electronics Letters, vol.22, (no.17), 14 Aug. 1986. p.905-6.

(26) S. Adachi, “Properties of Aluminium Gallium Arsenide”. INSPEC 3th edition 1993.

(27)Hsieh, H.C.; Sargeant, W. ‘Avalanche buildup time of an InP/InGaAsP/InGaAs APD at high gain’. IEEE Journal of Quantum Electronics, vol.25, (no.9), Sept. 1989. p.2027-35.

(28) Weishu Wu; Hawkins, A.R.; Bowers, J.E. ‘Design of silicon hetero-interface photodetectors’. Journal of Lightwave Technology, vol.15, (no.8), IEEE, Aug. 1997. p.1608-15.

(29) Droge, E.; Bottcher, E.H.; Kollakowski, S.; Strittmatter, A.; Bimberg, D.; Reimann, O.; Steingruber, R. ‘78 GHz distributed InGaAs MSM photodetector ‘. Electronics Letters, vol.34, (no.23), IEE, 12 Nov. 1998. p.2241-3..

(30)Taylor, H.F.; Eknoyan, O.; Park, C.S.; Choi, K.N.; Chang, K. Traveling wave photodetectors. Proceedings of the SPIE - The International Society for Optical Engineering, vol.1217, (Optoelectronic Signal Processing for Phased-Array Antennas II, Los Angeles, CA, USA, 16-17 Jan. 1990.) 1990. p.59-63.

(31) Hietala, V.M.; Vawter, G.A.; Brennan, T.M.; Hammons, B.E. ‘Traveling-wave photodetectors for high-power, large-bandwidth applications’. IEEE Transactions on Microwave Theory and Techniques, vol.43, (no.9, pt.2), Sept. 1995. p.2291-8.

(32)Bottcher, E.H.; Bimberg, D. ‘Millimeter wave distributed metal-semiconductor-metal photodetectors’. Applied Physics Letters, vol.66, (no.26), 26 June 1995. p.3648-50.
(33)Bottcher, E.H.; Pfitzenmaier, H.; Droge, E.; Bimberg, D. ‘Millimetre-wave coplanar waveguide slow wave transmission lines on InP’. Electronics Letters, vol.32, (no.15), IEE, 18 July 1996. p.1377-8.

Chapter 2

Theory and Model of Distributed Photocurrent

The traveling wave photodetector (TWPD) is one kind of waveguide photodetector (WGPD) (Figure 2.1). Light is edge coupled into the optical waveguide. The electrical wave is generated by the distributive point sources. The optical wave and the generated electrical wave travel in the same direction. The bandwidth is determined by the interaction of optical and electrical waves along the propagation line and the intrinsic region response. With suitable design (TWPD) in the structure, the speed can be optimized. For the fastest traveling wave photodetectors, the velocities of the optical wave should match the electrical wave such that there are no walk-off problems. And also, the matching of microwave impedance to the load circuit is needed to overcome the reflection from the load, which mainly causes the RC lump element limitation. Ideally, the TWPD bandwidth limitation can be made as high as possible. However, waveguide photodetectors generally are not TWPD since the electrical wave is slower than the optical wave. Generally, the waveguide always suffers microwave loss and dispersion from non-ideal metalization and the doping material, such that the bandwidth will dramatically drop down once waveguide length is increased. Therefore, if the optical and electrical waves interact in the coherent distance such that bandwidth is not degraded by velocity mismatch, the photodetectors are defined as TWPDs.

2.1 Model to calculate the bandwidth limitation

To realize the bandwidth performance of a TWPD [1,2], fully distributed photocurrents are modeled to describe the device response. Figure 2.2 shows the schematic diagram of the material and the device. The model assumes that the

optical waveguide is made of a p-i-n AlGaAs heterostructure. The active region is low-temperature grown GaAs (LT-GaAs) or GaAs. The thickness is on the order of 100 nm. In order to obtain a short carrier lifetime, we use LT-GaAs [3,4] with an effective carrier trapping time on the order of one picosecond to subpiccosecond [5,6]. This length and the properties of the intrinsic material determine the current source response. In the theory of distributive effects, the total current is collected from the small current point sources, and this point element is based on the p-i-n structure. All the devices discussed in this dissertation are based on this structure.

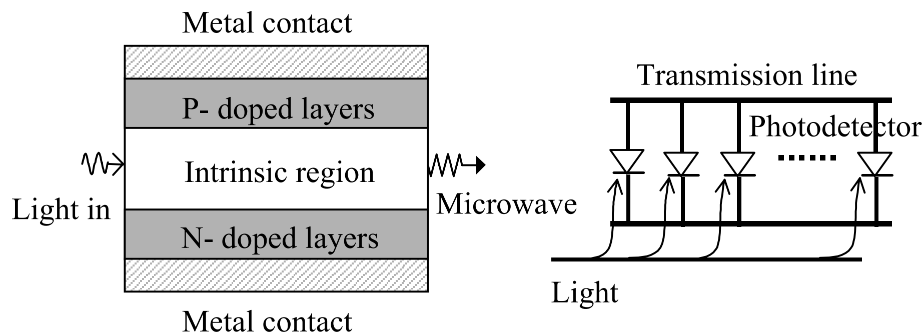

Figure 2.1. Waveguide photodetectors are formed by the distributed photodiodes

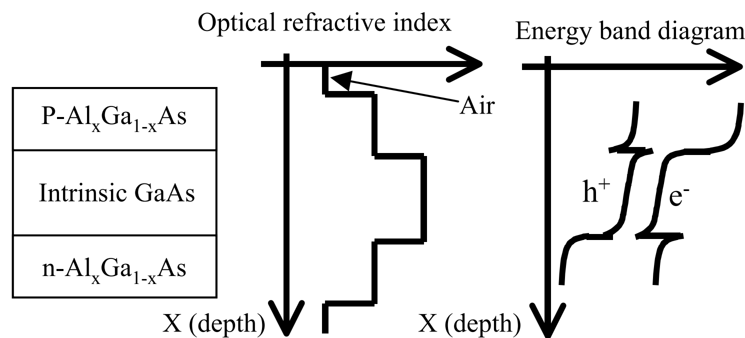

Figure 2.2. The p-i-n heterostructure supports the optical waveguide guiding also the selective optical absorption region

The p-i-n structure is also used as a microwave transmission line [7,8], which combines the metal-insulator-semiconductor (MIS) and coplanar waveguide

(CPW) structures. In this transmission line structure, the equivalent circuit model is adopted to simplify the calculation of the frequency response.

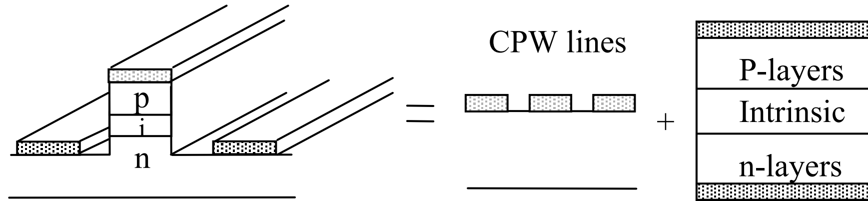

Figure2.3. The hybrid coplanar waveguide is equivalently composed by the CPW line and microstrip lines

2.1.1. Equivalent circuit model:

After the optical pulse travels through the detectors, a series of distributed photocharges will be generated along the transmission line. The photocharge is accelerated by the field in the intrinsic region and forms the distributive current pulses. By the effects of the transmission line, these current pulses will be the source of the microwave signal, which travels and is collected in the output. The propagation properties of transmission lines will affect the collected microwave signal. The pulse will be broadened due to the loss and dispersion and the reflection effects by the impedance mismatch between the line and output load circuits. A good TWPD should have good transmission characteristics, i.e. low loss and dispersion. The analysis and calculation to investigate the microwave transmission line are based on the p-i-n structure, as shown in figure 2.3. Basically, a coplanar-TWPD is formed by one intrinsic semiconductor layer sandwiched by two doped conductive layers (n or p doping). The CPW gold layers connect the n- and p- doped conductive layers to convey the microwave signal. In such kind of line, the transverse field of microwave signal is much larger than the longitudinal field due to the boundary conditions. The microwave can thus be approximately transverse-electromagnetic (TEM) mode or quasi-TEM [8,9]. In references [2,10], the full wave analysis is compared with the equivalent circuit model and it is found

that the transmission line properties can be accurately approximated by the equivalent circuit model up to sub-THz and THz regime. The simpler equivalent circuit model is used to analyze transmission line effects.

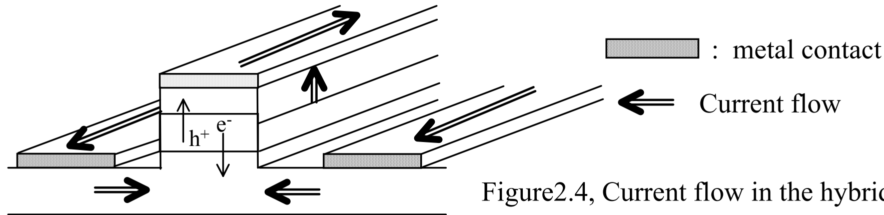

Figure2.4, Current flow in the hybrid CPW line

To begin with an equivalent circuit model, the physical elements of the coplanar TWPD should be defined to extract the corresponding circuit. As shown in Figure 2.3, it includes CPW metal plates, which includes two ground pads and one center signal pad. The difference between coplanar TWPD and CPW is that the metal pads are contacted with high doping semiconductor material (n- or p-doped) to connect to the intrinsic region (i-layer). The micro-strip (MS) and the CPW line metalization structures are then combined. This kind of hybrid waveguide structure has advantages: due to the coplanar CPW structure, it has high bandwidth performance and the capability to be compatible with general CPW lines for transmitting signal and connecting other microwave devices, such as, electrical amplifiers, and electronic circuits. Since all the metalization is coplanar, the processing is easy to make by general semiconductor fabrication. The series resistance in the material can be engineered by the growth of n- or p- type layers.

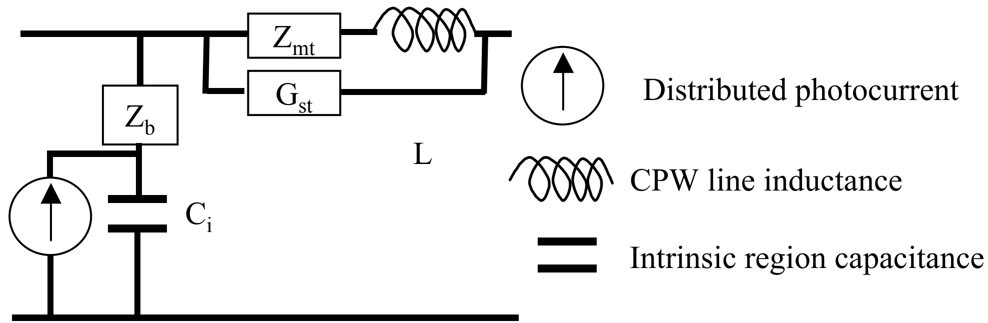

Figure 2.5, the corresponding equivalent circuit of Figure 2.4

The device dimensions and the material properties are used to accurately calculate the transmission line propagation. As shown in Figure 2.4 (cross section of device), the intrinsic region (i-layer) is the main capacitance contributed to the circuit and also it is the region that generated the photocurrent. In the transmission line, it is convenient to define the unit of circuit as the quantities per unit length. The intrinsic capacitance C_i is the capacitance per unit length, which is in proportion to the waveguide width w times the intrinsic permitivity of the i-layer (here is the LT-GaAs material) and divided by the i-layer thickness d_i. There are two aspects relating the device performance to the capacitance.

First: it is the place where the carriers are generated. The photocurrent is dependent on the velocity and the applied voltage, and also the loss of carriers during the transit across the active region (i-layer). So, the bandwidth limitation and the quantum efficiency of the photodetector are partially determined by the intrinsic material properties. For example, high quality material will have high mobility and low recombination rate by an imperfect center. Or, the high recombination rate in the material easily causes the high-speed response of the photocurrent. The current can be expressed by the form of current source in the circuit (Figure 2.5) and separately defined by the material properties.

Second : the capacitance C_i correlating the inductance L_m determines the propagation properties of the transmission line, for example, the characteristic

impedance and the propagation constant. Generally, in the TWPD structure, a large capacitance (C_i) results in a slow microwave transmission, which will walk off the optical signal and then broaden the photodetector impulse response. On the other hand, high quantum efficiency requires a thin active region to reduce the carrier transit time to obtain a high ration of carrier lifetime to carrier transit time [14]. As discussed in Chapter 1, the high capacitance (from the thin active region) will inevitably limit the RC-lump response in the perpendicular illumination structure, or, the walk–off factor will decrease the device bandwidth in the waveguide structure. Therefore, in the designing the device structure, the capacitance should be optimized.

The microwave travels through the transmission line by the interaction of electrical and magnetic fields. The electrical field is mainly controlled by the capacitance. The magnetic field can be represented by the inductance L_m. When the current is driven on the metal plates (usually gold metal), it generates the magnetic field surrounding the metal plates. In the simple case of the parallel plate transmission line, the inductance can be expressed by $L_m = \mu \frac{D}{w}$, where D is the distance between two plates, w is the width of plates and μ is the permeability of the material.

In the coplanar TWPD structure, however, the geometry of metal plates are quite different from the parallel, the calculation of inductance is thus more complicated. But, in the first order of approximation, the inductance L_m is in proportion to the value of $\frac{D}{w}$. Because the AlGaAs material is not a magnetic material, the inductance L_m is equal to that of a CPW line of the same size. This value can be calculated from the reference [11] or softwave like LineCalc [12].

The series resistance Z_t and Z_b is the resistance for conduction current flowing through the top and bottom semiconductor layers (n- or p- doped region) and the contact resistance of metal and semiconductor. In this circuit model, the frequency of interest is ranged up to several hundred GHz. The series resistance of the contact and the doping semiconductor layers should be modified by the displacement current in high frequency, this means that the resistance is frequency dependent. So, the imaginary part of Y is not only determined by the intrinsic capacitance. All the displacement current will contribute to the loss and dispersion of transmission.

The Z_{mt} part is coming from the finite conductivity of metal plate. Once the longitudinal time-varying current flows through the metalization, it builds up not only the magnetical fields that result in the inductance L_m and the ohmic loss, but also the skin effects in the metal. The effective cross area of current flows due to the skin effects can be expressed as in proportion to skin depth ($\delta_m = 1/\sqrt{2\pi f \mu_0 \sigma_m}$, f: the microwave frequency, μ_0: the magnetic permitivity and σ_m: the conductivity of metal). As the frequency is higher, the transmission line gets more resistance and larger inductance due to the metal skin effects. Therefore the loss and dispersion will change the electrical pulse transmission on the line. At the low frequency regime, the finite thickness d_m of metal is much smaller than the skin depth (δ_m), so the impedance is limited by the metal itself (approaching to $1/\sigma_m d_m$). In the reverse way, at high frequency regime, $d_m >> 1/\sqrt{\omega \mu_0 \sigma_m}$, the impedance will be terminated by $\sqrt{j\omega\mu_0 / \sigma_m}$ [7,13].

The longitudinal conductance G_s represents the longitudinal conductance current flowing through semiconductor layers due to the small amount of longitudinal electrical field (E_z).

All the parameters used in calculating the propagation impedance are listed in Table 2.1.

Table 2.1

$$C_i = \varepsilon_i \cdot \frac{w}{d_i}$$

$L =$ The inductance of CPW line [11,12]

$$Z_y = (\frac{1}{1 + j\omega\rho_{st}\varepsilon_{st}})\frac{\rho_{st} d_{st}}{w} + (\frac{1}{1 + j\omega\rho_{sb}\varepsilon_{sb}})(\frac{\rho_{sb} w_g}{2d_{sb}} + \frac{w}{6d_{sb}})$$

$$Z_s = \sqrt{j\omega\mu_0 / \sigma_m} \cdot \coth[(1 + j) \cdot d_m \cdot \sqrt{\omega\mu_0\sigma_m}]$$

$$G_s = \frac{\sigma_m}{3} \cdot \frac{w_c \cdot d_{st}}{1 + j\omega\rho_{st}\varepsilon_{st}}$$

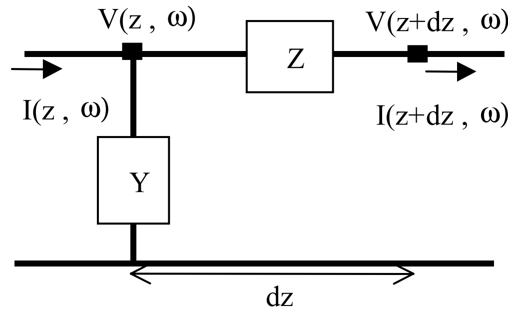

Figure 2.6. The generalized equivalent circuit model

To sum up the total circuit characteristics, it is helpful to use a generalized configuration, as shown in Figure 2.6, to calculate the current and the voltage distribution along the transmission line. Assuming the passive waveguide (without considering the current source), the generalized equation can be expressed as:

$$\begin{matrix} I(z+dz,\omega) - I(z) \approx V(z,\omega) \cdot Y(\omega) \cdot dz \\ V(z+dz,\omega) - V(z) \approx I(z,\omega) \cdot Z(\omega) \cdot dz \end{matrix} \overset{dz \to 0}{\Rightarrow} \begin{matrix} \frac{dI}{dz} = -V \cdot Y \\ \frac{dV}{dz} = -I \cdot Z \end{matrix} \Rightarrow \begin{matrix} \frac{d^2V}{dz^2} = \gamma^2 \cdot V \\ \frac{d^2I}{dz^2} = \gamma^2 \cdot I \end{matrix} \quad (1)$$

where $\gamma = \alpha_m + j\beta_m$, α_m: microwave field attenuation constant, β_m: microwave propagation constant. The microwave loss can be directly calculated by $-20 \cdot \log(\alpha_m \cdot l)$ (unit dB) and the microwave phase velocity is $v_m(\omega) = \omega / \beta_m$. The solutions of wave equation (1) are in the forms of $A^+ \cdot e^{-\gamma \cdot z} + A^- \cdot e^{\gamma \cdot z}$, where A^+ and A^- represent the forward and backward wave amplitudes. The wave amplitudes depend on the boundary conditions and the distributed current sources. The relation between voltage and current can be calculated by characteristic impedance $Z_0 = \sqrt{Z/Y}$.

In the calculation, the dimensions and materials of device are set as reasonable conditions of the AlGaAs p-i-n diode. It assumes 1 μm width and 2 μm gap of CPW metalization, the intrinsic layer is 100 nm of GaAs, and the cladding layers are n- and p- doped of $Al_{0.2}Ga_{0.8}As$. Figure 2.7 shows the microwave index (dispersion effects) and field attenuation coefficient of the transmission line. Figure 2.8 plots the impedance of real, imaginary and absolute part of impedance. The ideal transmission line in Figures 2.7 and 2.8 is calculated by the equations:

$$v_m = \sqrt{1/LC_i}$$

$$Z_0 = \sqrt{L/C_i} \quad (2)$$

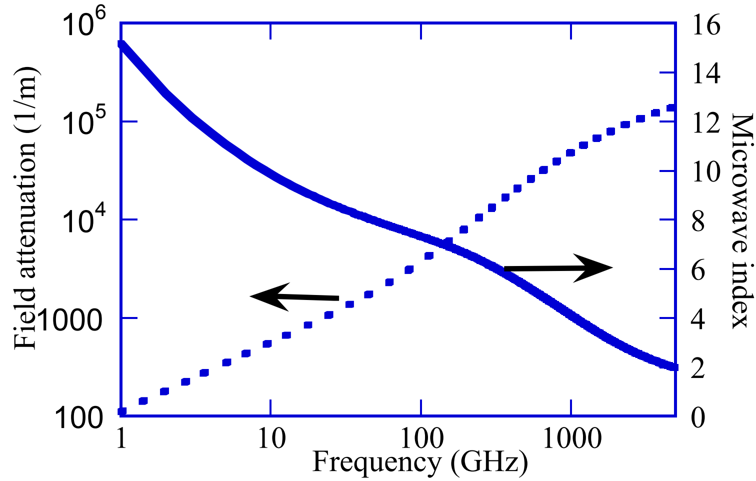

Figure 2.7, The microwave field attenuation and index with frequency. The dashed curve is the microwave field attenuation, the solid curve is the microwave index (dispersion).

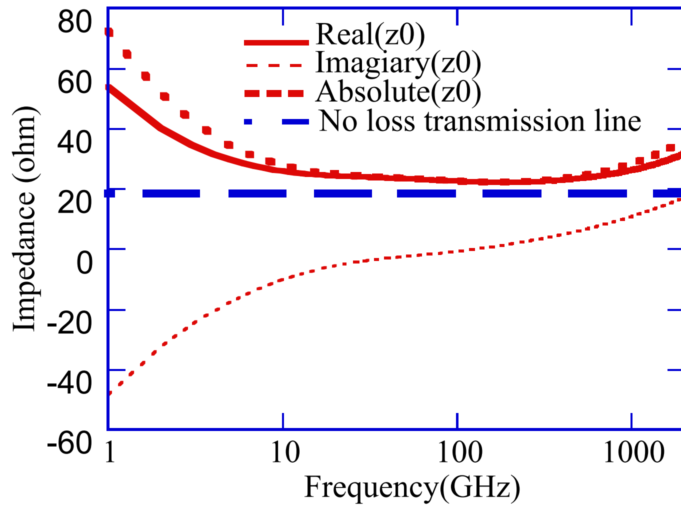

Figure 2.8. The characteristic impedance o f p-i-n waveguide.

As shown in the plots, in the frequency region of 10 GHz ~1000 GHz, the lossy transmission line approaches the ideal case quite well. This is because as in the middle frequency (10 GHz ~1000 GHz in this case), the conditions of $\omega L >> Gs$, $\omega L >> |Zmt|$ and $\omega C_i << 1/|Z_t + Z_b|$ are satisfied so that the dispersion due to metal skin effects and resistive material can be neglected. In Al $_{0.2}$Ga$_{0.8}$As

material (doped with $5\times10^{18} cm^{-3}$), the resistivity ρ_s is around 70 $\Omega\cdot\mu m$. The corresponding $1/\omega C_i$ is in the order of $10^{-3}(\Omega\cdot m)^{-1}$, Z_s is $10^{-4}(\Omega\cdot m)^{-1}$, $\omega\cdot L$ is $10^{6}(\Omega\cdot m)^{-1}$, and Z_{mt} is $10^{5}(\Omega\cdot m)^{-1}$. At this point, the performance of ideal transmission (equation (1)) can approximately describe the microwave velocity and the characteristic impedance. However, regarding the microwave loss, as shown in Figure 2.7, it is monotonously increasing from low to high frequency. For example, from 500 GHz to 1 THz, the field attenuation is around 0.01 μm^{-1}, this means that after 50 μm of propagation, the electrical signal will get about –10 dB loss, which almost terminates the bandwidth performance. In the design of TWPD structure, the microwave loss effects need to be considered.

In the low frequency regime ($\omega L << Z_{mt}$, $\omega L G_{st} << 1$, $\omega C_i << 1/Z_b$), the skin effects and the impedance of metalization inductance can be neglected. The term *Z* (Figure2.6) is thus determined by the finite resistivity of metalization. The intrinsic capacitance impedance is much larger than bulk AlGaAs resistance. Therefore, the transmission line is like a periodic RC circuit, where the R is mainly contributed by the metalization, C is mainly from the intrinsic region. In this case, the propagation constant is in proportion to $\sqrt{\omega}\cdot(1+j)$ and the characteristic impedance is $1/\sqrt{\omega}\cdot(1-j)$. The corresponding microwave phase velocity will diverge as $\omega\rightarrow 0$ and also the impedance. These low frequency behaviors can be seen in Figures 2.7 and 2.8. The increase of microwave index and impedance as at the low frequency were also observed in the experiment (Chapter 4).

At high frequency regime ($\omega\rho\varepsilon >> 1$, generally > THz), the semiconductor turns out to be capacitance-like behavior rather than resistivity, due to the material relaxation. The overall capacitance of transmission line is the series connection of material capacitance and the intrinsic capacitance. The inductance is dominated by

the metal impedance (skin effects) at the frequency. So, the microwave phase velocity and characteristic impedance are not low.

2.1.2 Bandwidth limitation of material response

The distributed nature of the TWPD is modeled as a series of photodetectors. The photocurrent is generated by optical excitation charges. The photocharges are then drifted by the electric field in the intrinsic region to form the photocurrent. While in the high electric field, the diffusion current can be neglected. So, generally, the current can be expressed by the amount of photocharge times the velocity. As mentioned in Chapter 1, to make a high speed photodetector, the key point is how fast these excess photocharges can be removed after the optical pulse. Typically, without considering the RC circuit effects, there are two ways to do this: (1) Making a short intrinsic region or getting high carrier mobility material to sweep out the photocharge in the short transit time. This is the *transit time limitation*. (2) Using a specific intrinsic material to trap the photogenerated electron and hole in a short period. This is the *recombination limitation*. The material properties decide which way the detector will be. In the distributed structure, the speeds of the small photodiodes (shown in Figure 2.1) give the material response. The thin intrinsic region or high carrier velocity has a short transit time. In this case, designing the geometric structures of intrinsic region, selecting material or material growth is important to achieve high speed material response. By the alternative way, for example, the LT-GaAs material has a short carrier lifetime and can be used to reach high-speed performance.

In the point view of a circuit, it can be assumed that the p-i-n photodiode is an ideal current source parallel connected with capacitance. To probe the speed of p-i-n detector, it is usual to use an δ-function of pumping optical power. The frequency response of optical signal is flat over the frequency of interest. Therefore, it can precisely detect the photodetector bandwidth. In the response of

detector, let us suppose the detector is operated in linear regime (i.e. without power-dependent response, field screening effects). The decay rate of carrier concentration after a sharp optical pulse can be described as a simple exponential decay form i.e.

$$I(t) = I_0 \cdot \exp(-\frac{t}{t_{decay}}) \qquad (3)$$

As mentioned above, the removal of photocharge from an active region is based on two mechanisms. The decay rates can be expressed by carrier transit time $t_{transit}$ and carrier lifetime $t_{lifetime}$. After combining these effects in the response of photodetectors, the current source can be expressed as:

$$I_{st}(t) = I_{so} \cdot \exp(-\frac{t}{t_{transit}}) \cdot \exp(-\frac{t}{t_{lifetime}}) = I_{so} \cdot \exp(-\frac{t}{t_{eff}}) \quad \text{if } t \geq 0$$

$$= 0 \quad \text{if } t < 0 \qquad (4)$$

, where $t_{transit}, t_{lifetime}$ are the carrier transit time across the intrinsic layer and the carrier lifetime. $\frac{1}{t_{eff}} = \frac{1}{t_{transit}} + \frac{1}{t_{lifetime}}$, t_{eff}: the carrier effective lifetime. If $t_{transit} >> t_{lifetime}$, the speed is dominated by recombination limitation; reversibly, by transit limitation.

In the frequency domain (by Fourier transform), equation(4) becomes:

$$I_{sf}(\omega) = \frac{A}{1 + j\omega \cdot t_{eff}} \qquad (5)$$

where ω is the microwave frequency, A is a constant proportion to the D.C. photocurrent response, which depends on on the pumping power level, optical wavelength and the ratio of $\frac{t_{lifetime}}{t_{transit}}$ [14].

2.1.3 Model for distributive photocurrent

After generating the electrical pulse by optical impulse pumping in the local material, the total response of the photodetetor composes all signals excited by the small current sources distributed along the waveguide. Figure 2.9 shows the schematic diagram how the distributive current is generated and propagated. When the electrical signal is collected in the load circuit, there are several factors affecting the impulse response of TWPD : (1) the velocity mismatch between optical and electrical waves, (2) the loss and dispersion of the microwave transmission line, (3) the reflection at the input end of the optical waveguide, (4) the output reflection at the load circuit causing the impedance mismatching of TWPD and load circuit, (5) the intrinsic material response (section 2.1.2), the carrier recombination and the carrier transit across the active region. In designing or calculating the pulse response, all these factors should be considered.

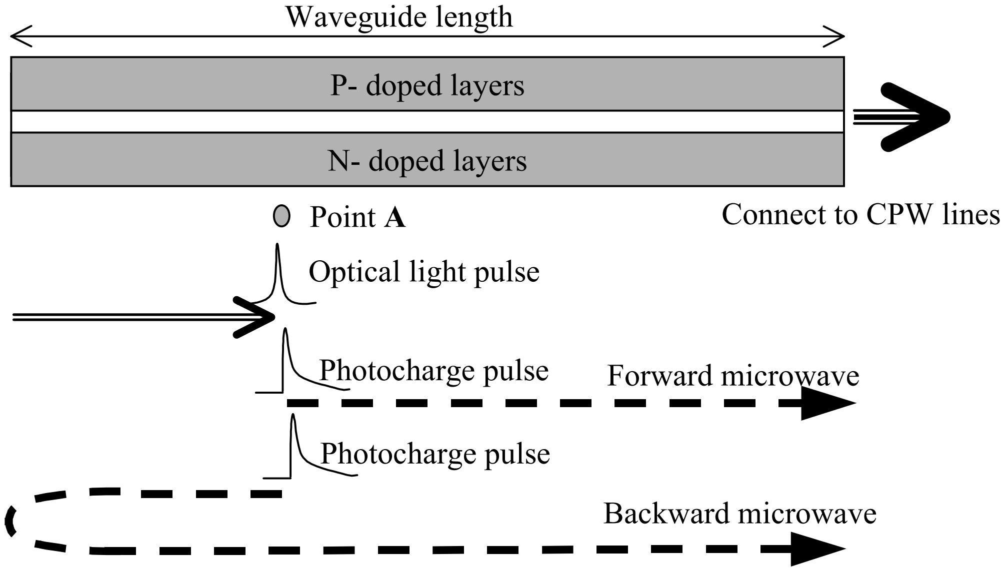

Figure 2.9, The schematic plot how the distributed photocurrent generated

Consider that the input optical impulse comes from the left side and is absorbed to generate the photocurrent along the transmission line. So, the optical pulse train can be described as:

$$P_o(x,t) = \frac{P_o}{\alpha_o} \cdot e^{-\alpha_o z} \cdot \delta(z - v_o \cdot t) \qquad (6)$$

where P_o : the total input power ; α_o : optical absorption coefficient ; z : the propagation direction, $v_o = \frac{c_o}{n_o}$: the optical group velocity, n_o :optical index. The optical input is assumed to be modulated by two different frequencies of laser beams, so the optical group velocity and index is used to describe the optical wave. After applying the Fourier transform, Equation (6) becomes:

$$P_o(z,\omega) = \frac{P_o}{v_o \cdot \alpha_o} \cdot \exp(-\alpha_o \cdot z - j\omega \cdot \frac{z}{v_o}) \qquad (7)$$

In Equation (7), it is presumed that the optical dispersion effect is neglected in the microwave frequency region (D.C. to several THz).

To convert the optical pulse to electrical pulse, we suppose the optical pulse travels through one point A (position z), as shown in Figure 2.9. And, the amount of optical power density $\frac{dP_o(z,t)}{dz}$ is absorbed in this point (which is in proportion to $\exp(-\alpha_o \cdot z)$). The time reference is set at optic input point (z = 0). The photoexcited electrical signal of this point A will experience a phase shift of $-\omega\frac{z}{v_0}$ (in time domain, it is a time delay of $\frac{z}{v_0}$). By the material properties of the intrinsic region, the electrical pulse will be in exponential decay, as described by Equation (5). Because the electrical pulse is excited in the microwave transmission line, it will travel in two opposite directions (noted by forward and backward waves) but with the same amplitude. If describing in the time domain, these two pulses will experience different time delays with respect to the optical pulse train (the walk-off problem) and also different electrical loss and dispersion, which will further broaden the pulses. It is complicated to do the analysis in time domain. Here, for convenience of calculation, the model is followed by the frequency domain. In the frequency domain, the backward and forward waves will experience different loss and phase shifts with respect to the optical phase:

Forward current: $I_{ff}(\omega,z) = I_{sf}(\omega)\cdot\exp(-\overline{\gamma_o}(\omega)\cdot z)\cdot\exp(-\overline{\gamma_m}(\omega)\cdot(l-z))$ (8)

Backward current: $I_{bf}(\omega,z) = I_{sf}(\omega)\cdot\exp(-\overline{\gamma_o}(\omega)\cdot z)\cdot\exp(-\overline{\gamma_m}(\omega)\cdot(z+l))$ (9)

, where , $\overline{\gamma_o} = \alpha_o + j\cdot\omega\cdot\frac{z}{v_o}$: optical complex propagation constant. $\overline{\gamma_m}$: microwave complex propagation constant, l : the device length. The notation of first subscript, f is the forward wave; b is the backward wave. And the second

subscript, f is the frequency domain and t is the time domain. The microwave response in the optical input is assumed to be an open circuit.

After calculating the response of a specific distributive photodetector at the receiving end, the total current is just the integral of the Equations (8) and (9) with respect to z over $z = 0 \sim l$. If the load impedance is matched to the transmission line, the total response will be :

$$I_f(\omega) = \int_0^l (I_{ff} + I_{bf}) \cdot dz = \frac{A \cdot \exp(-\overline{\gamma_m} \cdot l)}{1 + j\omega \cdot t_{eff}} \cdot \left(\frac{1 - \exp(-(\overline{\gamma_o} - \overline{\gamma_m}) \cdot l)}{\overline{\gamma_o} - \overline{\gamma_m}} + \frac{1 - \exp(-(\overline{\gamma_o} + \overline{\gamma_m}) \cdot l)}{\overline{\gamma_o} + \overline{\gamma_m}}\right)$$

-----A----- **-----B-----** **-----C----** (10)

To consider the case when the line is not matched to the load circuit, the total response should be taken into account about the multiple reflections on the device. The response is:

$$I_f(\omega) = \left(\frac{\mathrm{T}_b(\omega)}{1 - \Gamma_b(\omega) \cdot \exp(j\overline{\gamma_m} \cdot l)}\right) \cdot \int_0^l (I_{ff} + I_{bf}) \cdot dz \qquad (11)$$

where the $\Gamma_b(\omega) = \frac{Z_l - Z_o}{Z_l + Z_o}$ is the reflection coefficiency of transmission line Z_o to load impedance Z_l, and $\mathrm{T}_b(\omega) = \frac{2Z_l}{Z_l + Z_o}$ is the transmission coefficient to the load circuit.

If the photodetector is a conventional vertical-illumination photodetector, as shown in Figure 2.10, the device is RC-time limited. From the equivalent circuit 2.10, the total frequency performance is the combination of the material properties and also the RC circuit. The response will be [15]:

$$I_f(\omega) = \frac{A}{(1 + j\omega \cdot t_{eff}) \cdot (1 + j\omega \cdot (R_s + Z_l) \cdot C)} \qquad (12)$$

--- **D** ---

where the R_s is the series resistance of p-i-n photodiode.

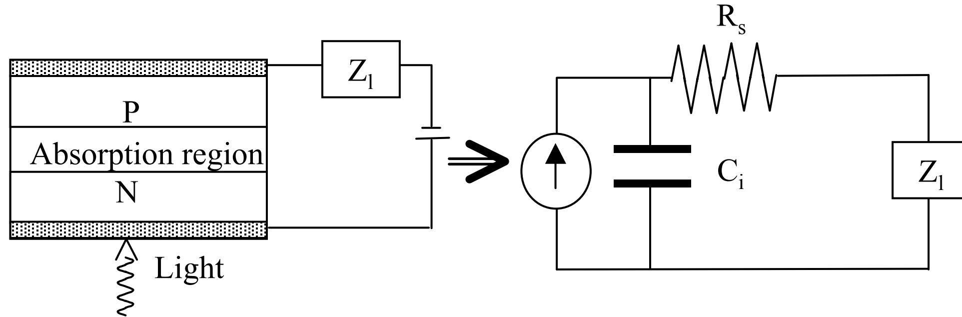

Figure 2.10, the schematic plot of top-illumination photodiode and the equivalent circuit model

The total frequency response of distributed photocurrent is given in Equations (10) and (11). A WGPD structure composes of highly position dependent photodetectors. The total response is composed of small photodetectors' current and the multiple reflections in the output load circuit (the term **D** of equation (11)). If high impedance mismatch (high reflection at the load, the term **D)**, the entire area of waveguide will participate the total response. The speed of WGPD is better represented by the lump-element (Equation (12)).

The distributive model (Equation (10) and (11)) and RC lump model (Equation (12)) have the same term of material response (the term with t_{eff}). The difference is only in the distributed effects. Equations (10),(11) show that the performance of photodetectors depends on the factors of $\overline{\gamma_o} - \overline{\gamma_m}$ and $\overline{\gamma_o} + \overline{\gamma_m}$, which includes the velocity, the microwave loss and dispersion effects, and the reflection in the input (the term **C**). Does the TWPD have the advantages over the conventional RC lump type (or WGPD)? What is the bandwidth limitation of the p-i-n TWPD ? What are the factors dominating the speed? To determine the performance of TWPD, more calculations are needed.

To begin the calculation, let's define the device structure. As shown in Figure 2.3, the device dimensions and material properties are listed below:

Waveguide width $w_c = 1\mu m$, CPW line gap $w_g = 2\mu m$, waveguide length $l = 100\mu m$. N-type and p-type cladding layers (AlGaAs) are assumed $d_{st} = d_{sb} = 0.7\mu m$ and with $\rho_s = 50(\Omega \cdot \mu m)$. The active region is $d_i = 100$ nm. The microwave reflection in the optical input end is set as $\gamma = 1$ (open circuit) or $\gamma = 0$ (loaded circuit).

A reasonable value of modal optical absorption coefficient $\Gamma\alpha_o = 0.1 \times 1\mu m^{-1}$ is used in the calculation. In this parameter, it is assumed that the modal confinement factor is constant for different waveguide structures. For convenience of analysis, it's better to keep it constant, although it changes while the active thickness or the waveguide width varies. The influence of that, in this case, will be discussed in the design of waveguide structure (Chapter 3). The optical propagation constant is given by $\beta_o = \omega \cdot n_o / c_0$, with optical group velocity $n_o = 3.45$. As mentioned, the dispersion effect of the optical wave can be neglected over the microwave frequency. So, the value of n_o is kept as constant.

(a) Ideal microwave transmission line response:

First of all, it is instructive to know how the velocity mismatch influences the device speed. To extract the mismatch problem, it is more helpful and convenient to neglect other effects. Let us assume an ideal p-i-n microwave waveguide is made. In the ideal transmission line, there will be no loss and dispersion for the microwave propagation. The microwave velocities ($v_m = 1/\sqrt{LC_i}$) and transmission line impedance ($Z_0 = \sqrt{L/C_i}$) are the inductance of CPW line and intrinsic capacitance dependent only, so Equation (2) is enough to describe the microwave transmission.

Consider a lossless transmission line matching to output circuit (no reflection), the length of line is long enough ($\Gamma\alpha_o \cdot L >> 1$) so that the optical power is completely converted to electrical signal, and no material response is involved (set $t_{eff} = 0$). From Equation (10), the output microwave signal becomes:

$$I_f(\omega) = A \cdot \exp(-j\omega / v_m \cdot l) \cdot (\underbrace{\frac{1}{\alpha_o + j(\omega / v_o - \omega / v_m)}}_{\mathbf{A}} + \underbrace{\frac{1}{\alpha_o + j(\omega / v_o + \omega / v_m)}}_{\mathbf{B}}) \qquad (12)$$

The term **A** is from the forward wave and **B** the backward wave (figure 2.9). It is simpler to look at the wave propagation in time. After the inverse Fourier transform of Equation (12), the response gives :

If $v_m < v_o$

$$I_t(t) = \frac{A}{2\pi}(\frac{v_m}{1 - v_m / v_o} \cdot e^{(\frac{\Gamma\alpha_o \cdot v_m}{1 - v_m / v_o}(t - l / v_m))} \cdot u(l - v_m t) + \frac{v_m}{1 + v_m / v_o} \cdot e^{(\frac{\Gamma\alpha_o \cdot v_m}{1 + v_m / v_o}(t - l / v_m))} \cdot u(v_m t - l))$$

If $v_m > v_o$

$$I_t(t) = \frac{A}{2\pi}(\frac{v_m}{v_m / v_o - 1} \cdot e^{-\frac{\Gamma\alpha_o \cdot v_m}{v_m / v_o - 1}(t - l / v_m)} + \frac{v_m}{1 + v_m / v_o} \cdot e^{-\frac{\Gamma\alpha_o \cdot v_m}{1 + v_m / v_o}(t - l / v_m)}) \cdot u(v_m t - l) \qquad (13)$$

where $u(t)$ is the unit step function.

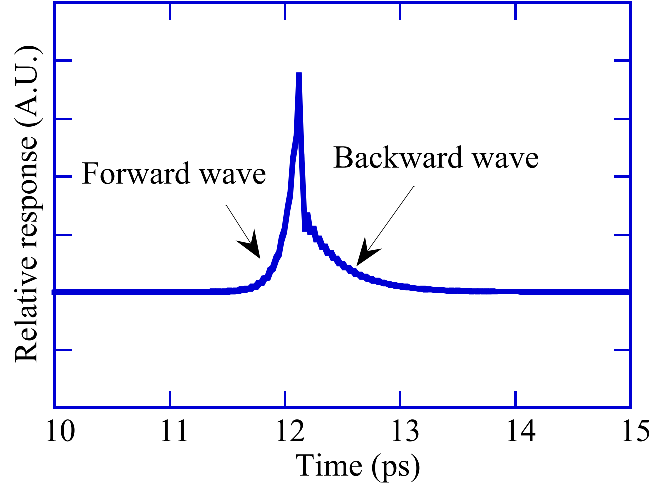

Figure 2.11. The ideal TWPD performance. The reflection in the optical input end is set as 1. The leading portion is the forward wave, and the tailor portion is from the backward wave.

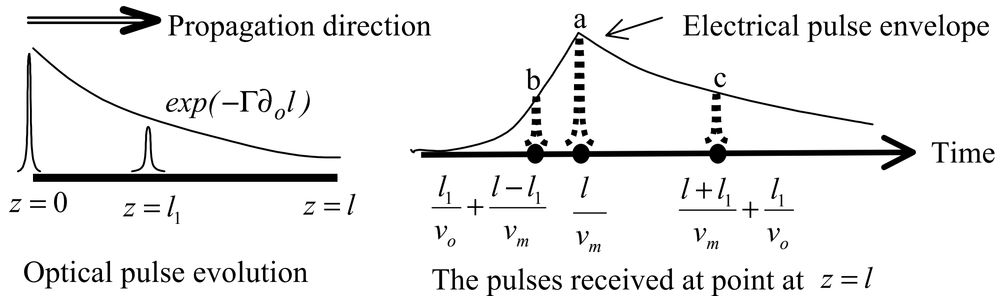

Figure2.12. The electrical pulse generation due to the walk-off of optical wave

From the device dimension, the inductance is $L = 4\cdot10^{-7}\,H/m$. It turns out that the microwave index is 6.4, which is larger than the optical index, (v_m is smaller than v_o). Figure 2.11 shows the output signal calculated from Equation (13). Basically, it composes two back to back exponential curves, which are the duplicates of optical pulse absorption but with different pulse broadening (walk off). The leading curve is coming from forward wave and the other one is the backward. Figure 2.12 depicts the schematic diagram how the distributive current

is collected at the output circuit. To figure out the electric pulse width, it is a good way to choose the e^{-1} drop as a figure of merit. Let's take a forward wave as an example. As shown in Figure 2.12, when the optical pulse inputs the waveguide, the peak distributive current happens in the optical input (point **a**). This small electrical pulse will spend the time of $\frac{l}{v_m}$ to the collected end. And the successive electric pulses will be generated after that. The point of e^{-1} drop occurs when the optical pulse travels to the position $z = 1/\Gamma\alpha_o$, where the optical light has been absorbed to e^{-1} of input. The small photocurrent excited at that point needs the time of $\frac{1/\Gamma\alpha_o}{v_o} + \frac{(l - 1/\Gamma\alpha_o)}{v_m}$ to arrive at the collected circuit (point **b**). Finally, the total accumulating signal pulse will expand to a pulse width of $(\frac{1}{v_o} - \frac{1}{v_m}) \cdot 1/\Gamma\alpha_o$. The only way to optimize the speed is to match the optical and the excited electrical waves ($v_o = v_m$) such that coherent optical-electrical interaction occurs (arriving at the collected point on the same time). Theoretically, the bandwidth of forward wave due to the matching design ($v_o = v_m$) in the distributed circuit is unlimited. This is the ideal approach of TWPD. As for the backward wave, the same analysis can be done. Suppose the optical input is an open circuit, the reflection is $\gamma = 1$. Due to the walk off problem, the pulse broadening by the reflection becomes $(\frac{1}{v_o} + \frac{1}{v_m}) \cdot 1/\Gamma\alpha_o$ (point **c**). The speed of backward wave can be enhanced by increasing the microwave velocity monotonously and be saturated by the optical velocity.

To check the velocity mismatch effects, Figure 2.13 shows the pulse response at a different velocity mismatch factor (v_m / v_o) which is defined as the relative velocity of microwave to optical wave. Here, the optical velocity is kept constant and the microwave velocity varies. The time reference point is set as in the optical input. Therefore, as shown in Figure 2.13, the time for receiving the signal is earlier as the microwave velocity increases. There are two cases in the forward wave transmission. If $v_m < v_o$ (the bottom two curves), the leading and trailing curves are from the forward and backward waves respectively. Both pulse widths (e^{-1} drop point) can be sharpened by increasing the microwave velocity. However, in the other case ($v_m > v_o$), by the higher relative velocities to the optical waves, the forward will be changed to the trailing edge and merge with the backward wave, as shown with the top two curves of Figure 2.13. As the microwave velocity increases, the forward wave is broadened but the backward wave is sharpened. So there will be one optimum condition to reach the highest bandwidth. This can be seen in the Figure 2.14. Figure 2.15 summarizes the TWPD by the ideal transmission line. It reveals that the ideal TWPD (without the backward reflection wave) can be obtained in the velocity matching point, $v_o = v_m$ (top curve of Figure 2.15). But, as the reflection is considered, the performance is dramatically dropped and the optimal condition is in some point of $v_m > v_o$. After the microwave velocity increase, the bandwidth will saturated and depends on the optical velocity only.

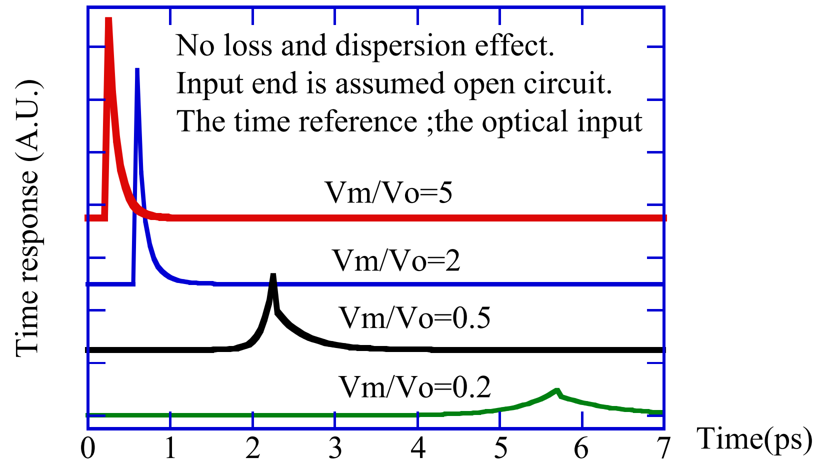

Figure 2.13. The electrical pulse at different velocity mismatching factors (v_m/v_o)

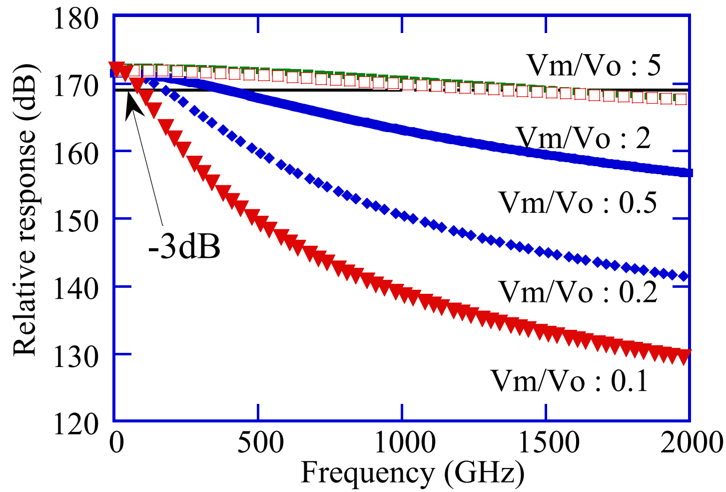

Figure 2.14. The frequency response of Figure2.13

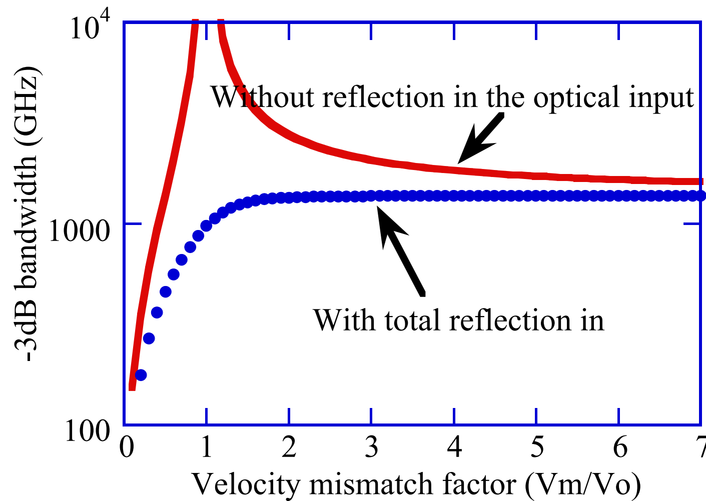

Figure 2.15. The -3dB bandwidth with velocity mismatch for the ideal TWPD (no loss and dispersion)

(b)The impedance mismatch effects :

When the mismatching of the load circuit has been considered, after the reflection on the output load, the signal will transmit along the line and feed back to the output. The bounce reflection waves will add to the original signal with round trip time delay. The detailed calculation of these effects can be seen in Equation (11). Due to the multiple reflections in both ends (here the optical input end is assumed as total reflection), the pulse amplitude is smaller and the pulsewidth is broadened by the successive delay pulses, which are the main reasons for resulting in the RC lump type. This means that the physical dimensions of photodetector are very important to device speed. In p-i-n WGPD, the electric field is almost concentrated in the active region. The larger area of photodetector (wide or long waveguide) has a slower microwave and lower characteristic impedance, which causes velocity or impedance mismatching. Assuming lossless and dispersionless transmission lines, two approaching ways are used to explain this: (1) keeping the waveguide length constant and varying the width. (2) keeping the waveguide width constant and changing the length.

In case (1), Figure 2.16 shows the bandwidth of TWPD structure for the impedance matching and mismatching. The load circuit is assumed 50 ohm. After putting the loading reflection, the bandwidth (the middle dash curve) is much less than impedance matching (the top curve). The microwave velocity and characteristic impedance are only dependent on the CPW line gap w_g and intrinsic layer thickness d_i in the p-i-n CPW ($L \approx \mu \frac{w_g}{w_c}, C \approx \varepsilon \frac{w_c}{d_i}$). Therefore the bandwidth of TWPD (either impedance match or mismatch) over the waveguide width range is flat. However, the bottom curve shows that the corresponding RC-limitation of the detector is much lower than the distributed effects.

Regarding case (2), Figure 2.17 plots the photodetector bandwidth with the device length. All parameters are set as in case (1) except the width is kept at $1 \mu m$ and the device length is changed. As shown, the impedance matching makes the TWPD have much higher speed performance over the mismatching, especially in the long device. In the time domain, the electrical pulse is broadened due to the impedance mismatching. The output amplitude is degraded due to successive pulses delayed by a round trip time of the waveguide. As shown in Figure 2.17, the time delays are neglected in the short devices, so the pulses are nearly coherently overlapped to still have a high bandwidth. Similarly, the RC-limitation is still much lower than the distributed effects.

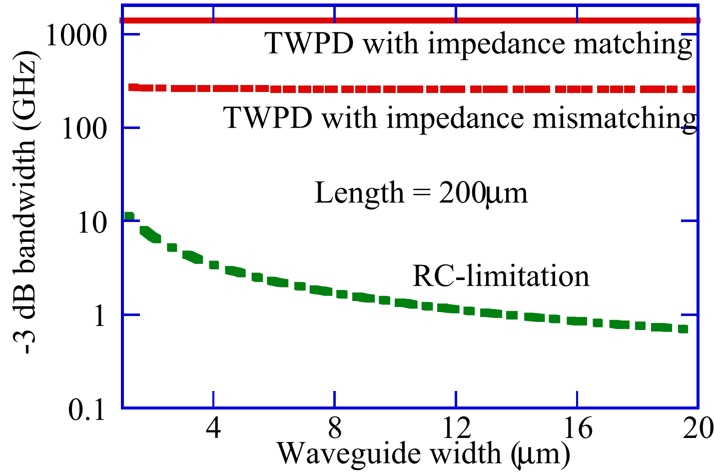

Figure2.16. -3dB bandwidth with the waveguide width.

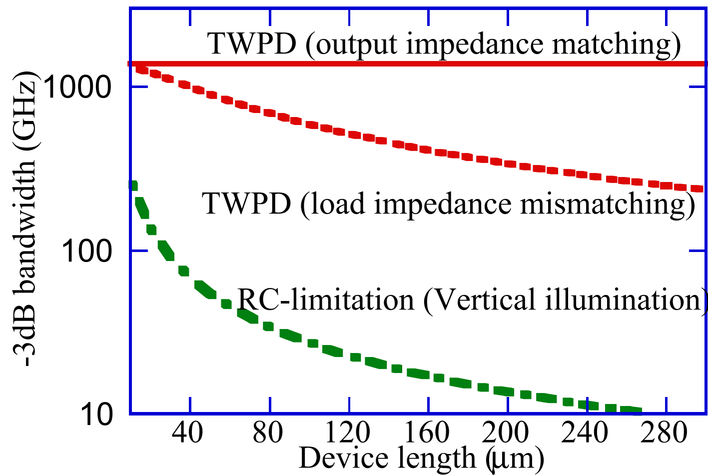

Figure 2.17. -3dB bandwidth with different device length.
Device width is set 1 µm

(c) Microwave loss effects:

As mentioned in Section 2.1.1, due to the doping layers and non-perfect metalization, the hybrid CPW transmission lines are inherently lossy and dispersive. By the distributive properties, the electrical pulses generated along the lines have different microwave loss and dispersion. Assuming no material response and optical power is completely absorbed ($\alpha_o \cdot l >> 1$) and $\alpha_o >> \alpha_m$

(typically optical field attenuation α_o is in the order of 1 or 0.1 μm^{-1}, and microwave field attenuation α_m is less than 0.01 μm^{-1} below the THz regime), Equation (10) becomes :

$$I_f(\omega) = A \cdot \exp(-\gamma_m \cdot l) \cdot \left(\frac{1}{\alpha_o + j(\beta_o - \beta_m(\omega))} + \frac{1}{\alpha_o + j(\beta_o + \beta_m(\omega))}\right) \quad (14)$$

---A--- ---B--- ---C---

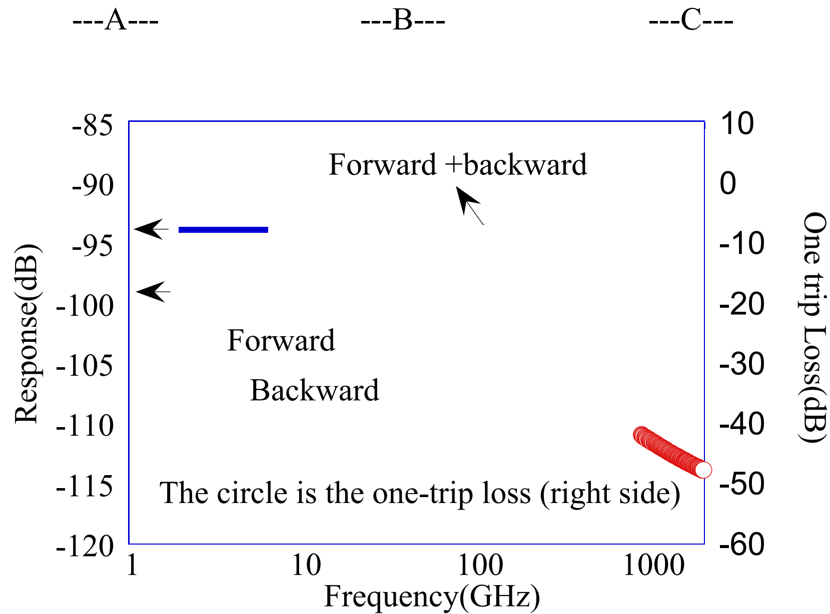

Figure2.18. Comparision of the response of forward and backward waves and the microwave loss.

Compared to Equation (12), the dependence on the response is not only the velocity mismatch but also the microwave loss (term A) and dispersion effects (term B). Based on the loss and dispersion curves (Figure 2.7), Figure 2.18 separately plots these effects on the forward and backward waves. As discussed in the Section 2.1.2, the velocity mismatch will influence the forward wave greatly. The best performance is when the optical velocity matches the microwave velocity. Because of the highly dispersive waveguide (the displacement current effects on material

and the skin effects of metalization), all the microwave velocities on frequency appear to speed up once the frequency becomes higher. The frequency response thus gets better for the forward waves (the solid curve). On the other hand, the backward (dashed curve) wave decreases. As mentioned in section 2.1.1, in the middle frequency response ($\omega L >> Gs$, $\omega L >> |Zmt|$ and $\omega C_i << 1/|Z_t + Z_b|$), the waveguide speed and impedance still can be approximated by the inductance and capacitance only. Therefore, the dependence of dispersion on the middle frequency range is quite flat. However, the loss is quite different. Since the strong skin effects of the metal on the high frequency range, the microwave loss becomes larger. In the middle frequency range, for example as shown in the figure 2.18, the total frequency response is almost dominated by the microwave loss term (circle one). In the design, eliminating microwave loss will be the most important part.

2.2 Summary

In this chapter, the bandwidth of the traveling wave photodetector is discussed. By using the equivalent circuits theory and the distributed effects as modeling the device performance, the bandwidth of photodetector is systematically analyzed. The analysis shows that not only the velocity impedance mismatching problems need to be considered but also the microwave loss.

Reference :

[1]Giboney, K.S.; Rodwell, M.J.W.; Bowers, J.E. 'Traveling-wave photodetectors'. IEEE Photonics Technology Letters, vol.4, (no.12), Dec. 1992. p.1363-5.

[2]Bottcher, E.H.; Pfitzenmaier, H.; Droge, E.; Bimberg, D. 'Millimetre-wave coplanar waveguide slow wave transmission lines on InP'. Electronics Letters, vol.32, (no.15), IEE, 18 July 1996. p.1377-8.

[3]Chou, S.Y.; Liu, M.Y. 'Nanoscale tera-hertz metal-semiconductor-metal photodetectors'. IEEE Journal of Quantum Electronics, vol.28, (no.10), Oct. 1992.

[4] Yi-Jen Chiu; Fleischer, S.B.; Lasaosa, D.; Bowers, J.E., 'Ultrafast (370 GHz bandwidth) p-i-n traveling wave photodetector using low-temperature-grown GaAs'. Applied Physics Letters, vol.71, (no.17), AIP, 27 Oct. 1997. p.2508-10.

[5]Harmon, E.S.; Melloch, M.R.; Woodall, J.M.; Nolte, D.D.; Otsuka, N.; Chang, C.L. 'Carrier lifetime versus anneal in low temperature growth GaAs'. Applied Physics Letters, vol.63, (no.16), 18 Oct. 1993. p.2248-50.
[6]Soole, J.B.D.; Schumacher, H. 'Transit-time limited frequency response of InGaAs MSM photodetectors'. IEEE Transactions on Electron Devices, vol.37, (no.11), Nov. 1990. p.2285-91.
[7]Jager, D. 'Slow-wave propagation along variable Schottky-contact microstrip line'. IEEE Transactions on Microwave Theory and Techniques, vol.MTT-24, (no.9), Sept. 1976. p.566-73.
[8]Kwon, Y.R.; Hietala, V.M.; Champlin, K.S. 'Quasi-TEM analysis of 'slow-wave mode propagation on coplanar microstructure MIS transmission lines'. IEEE Transactions on Microwave Theory and Techniques, vol.MTT-35, (no.6), June 1987.
[9]Dan Tauber's, ' Design and performance of semiconductor microstrip lasers', UCSB Ph.D. Dissertation March 1998
[10]Giboney, K.S.; Rodwell, J.W.; Bowers, J.E. 'Traveling-wave photodetector theory. IEEE Transactions on Microwave Theory and Techniques', vol.45, (no.8, pt.2), IEEE, Aug. 1997. p.1310-19.
[11]Reinmut K. Hoffmann, ' Handbook of microwave integrated circuits'
[12]Eesof, Inc. LineCalc Westlake Village, CA:Eesof,1991
[13]Henry Guckel, Pierce A. Brennan, and Istvan Palocz, ' A parallel-plate waveguide approach to micro-miniaturized , planar transmission lines for integrated circuits.', IEEE Transactions on Microwave Theory and Techniques', vol.15, (no.8) Aug. 1967. p.468-476.
[14]S.M. Sze , 'Physics of Semiconductor device'. 2nd edition, p746.
[15]Yih-Guei Wey, 'High-speed double heterostructure GaInAs/InP p-i-n photodetectors: Theory, fabrication, and measurement' , UCSB Ph.D. dissertation.

Chapter 3

Device Design and Fabrication

According to the previous discussion, the main factors influencing the speed of distributed photodetectors are velocity mismatching, impedance mismatching, and microwave loss. In a long p-i-n waveguide, the transmission line will suffer from the high microwave propagation loss. At high frequencies, no matter how much effort is done in the treatment of velocity and impedance matching, the device speed is limited by the microwave loss. From a design point of view, a traveling wave structure is used only when the devices are short enough so that the bandwidth is determined by the material response only. Over these length scales, the optical wave and the electrical wave interact coherently without any other loss penalty. In the design of a low-temperature grown GaAs (LT-GaAs) TWPD, the main emphasis is to have the bandwidth of the circuits for the distributed photodetectors higher than the limitation by the carrier trapping effects in the LT-GaAs. The work for designing the device structures includes:

(1) TWPD Circuit design: how to determine the device length and the depletion thickness? The input optical power should be completely absorbed to obtain high quantum efficiency. Also, the circuit bandwidth will not be degraded due to the high microwave loss of long device. Two important features are needed to consider in the design, namely, the quantum efficiency and the bandwidth. Increasing the intrinsic region thickness will enhance the speed due to the higher impedance, microwave velocity, optical confinement factor and the lower microwave loss; however, the quantum efficiency becomes lower due to longer transit time.

(2) Heterostructure design: what composition and structure of material should be grown in the heterojunction? With the AlAs/GaAs graded

heterjunctions, the carrier diffusion due to the homojunction and also the carrier trapping in the abrupt junction can be eliminated. In the intrinsic region, a low-temperature grown GaAs is used. This provides a high carrier-trapping rate in the active region to achieve a high bandwidth.

(3) Device fabrication: the device fabrication is based on the standard self-aligned ridge waveguide processing. The epilayers are grown on a semi-insulating GaAs wafer. Polyimide is used to passivate the etching surface. Ion-implantation is used to create insulating regions for the output loaded CPW lines.

3.1 TWPD circuit design:

The structure of the TWPD is a hybrid coplanar waveguide, which combines the micro-strip (MS) and coplanar waveguide (CPW) structures (as mentioned in Chapter 2). This structure has several advantages. It is easily fabricated with the general lithography process as high-speed laser [1] or high-speed modulator [2] because of the coplanar metalization. From an application viewpoint, the coplanar structure has the flexibility that it can be connected to the other compatible electronic circuits, for example, microwave amplifiers. Since CPW has lower capacitance and dispersion compared to microstriplines [3], signals are easily transmitted without distortion and with lower loss. The CPW structure also facilitates measurements by electro-optical sampling technique or by high bandwidth microwave probes for electrical sampling. Using the MS structure, the p-i-n device can be easily fabricated and connected to CPW lines.

For designing the TWPD, the equivalent circuits are derived from the geometry in Figure 2.4. Capacitance, inductance and resistance of the bulk material are listed in the Table 2.1. Here, we use the same notations for semiconductor material parameters as the ones in Table 2. As it was already mentioned the goal for the optimization of the photodetectors speeds is to *match microwave impedance to the output load CPW lines*, *match the velocity of microwave to the optical wave* and *reduce the microwave loss within the optical*

absorption length. Besides the bandwidth of the devices, the quantum efficiency is the another important figure-of-merit. The quantum efficiency η can be expressed by [4]:

$$\eta = \eta_g \cdot \frac{p_o}{h \cdot \nu} \cdot q \cdot (1 - e^{-\Gamma \cdot \alpha \cdot l}) \cdot \frac{t_l}{t_t} \qquad (3.1)$$

η_g : the coupling efficiency from the Fresnel reflection, optical mode mismatch and the scattering at the input end.

p_o : the total optical power

h : Plank's constant, ν : optical frequency, q: electrical charge.

α : optical absorption coefficient of the bulk material, Γ : the confinement factor in the intrinsic region. l : device length.

t_l : carrier lifetime, t_t : carrier transit time across the intrinsic region

In Equation 3.1, the factor of ${}^{t_l}/_{t_t}$ determines the ratio of the mobile photocharges lost in the intrinsic region. To increase the efficiency, one way is to have a thin intrinsic region to make the sweep time across the region small. But, it will slow down the photodetector speed due to the high intrinsic capacitance. To examine which factors dominate the device performance; it is necessary to calculate the speed and the efficiency of photodetector.

(a) Transmission line bandwidth:

In this work, the low-temperature grown GaAs (LT-GaAs) is primarily used for high-speed detector application due to its low carrier lifetime. The carrier lifetime in LT-GaAs is ranged from sub-picosecond to picosecond [5,6] depending on the different annealing temperatures. The carrier saturation velocity in the GaAs material is around 10^7 cm/second. Assuming the transit time is 1 ps to get a

reasonable value of t_l / t_t, the corresponding intrinsic region width is 100 nm. So, it is helpful to set the active region as in the order of 100 nm.

Figure 3.1a plots the real and imaginary parts of the p-i-n transmission line impedance as a function of frequency for waveguide width $w_c = 2\mu m$ and depletion region thickness $d_i = 200$ nm. As discussed in Section 2, in the middle frequency region (10 GHz to 1000 GHz), the microwave velocity and the characteristic impedance can approximately be treated as an ideal transmission line. In this middle frequency regime, the impedance is flat and the real part of characteristic impedance is much higher than the imaginary part. It is more convenient to use the absolute value of the impedance to estimate the impedance matching.

Figure 3.1.b shows the characteristic impedance for different widths w_c ($1\mu m$ and $2\mu m$) and the depletion region thickness d_i, ($100nm$ to $300nm$). Compared to the general instrument impedance of 50 Ω, all the impedance values are quite lower over the frequency regime of interest. The trend is that a wider waveguide and a thinner intrinsic region result in a higher impedance mismatch. If the waveguide width is narrowed below $1\mu m$, the impedance can be matched to the output circuit. However, the optical coupling efficiency into the waveguide will be dramatically reduced since the wavelength of light is around 0.85 μm (bandgap of GaAs). Due to the diffraction limits, the light cannot be focused to too much below the value. Therefore, in order to eliminate the reflection from the output loaded circuit, it is better to set the waveguide width as $1\mu m$.

Figure 3.2 shows the microwave index of the transmission line (from the dispersion of waveguide). The dispersion effects are mainly from the resistive semiconductor material and the non-ideal metal. The waveguide has quite different microwave velocities from D.C. to high frequency. As shown, the microwave

phase velocity is slower while the loaded capacitance of waveguide increases (*di* is smaller). As for the GaAs/AlAs material optical waveguide , the optical group velocity is in the range of 3.0 to 4.5 [7]. As shown in Figure 3.2, only the optical index with intrinsic region thicker than 300 nm can fit over the middle frequency region (10~1000 GHz).

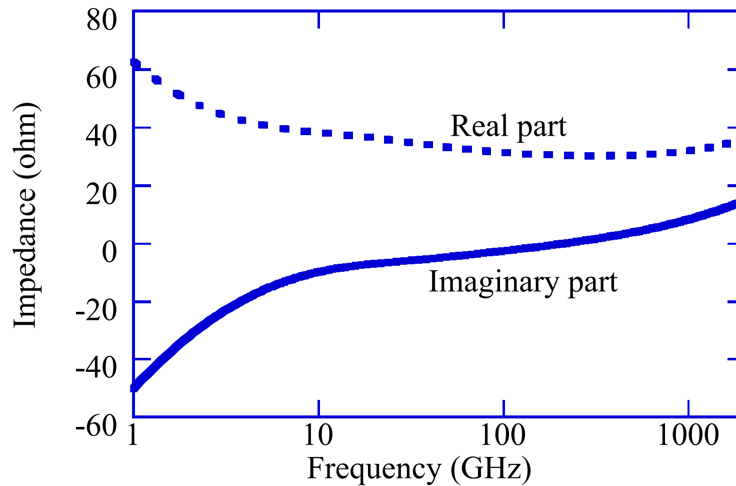

Figure3.1a. The characteristic impedance of p-i-n waveguide

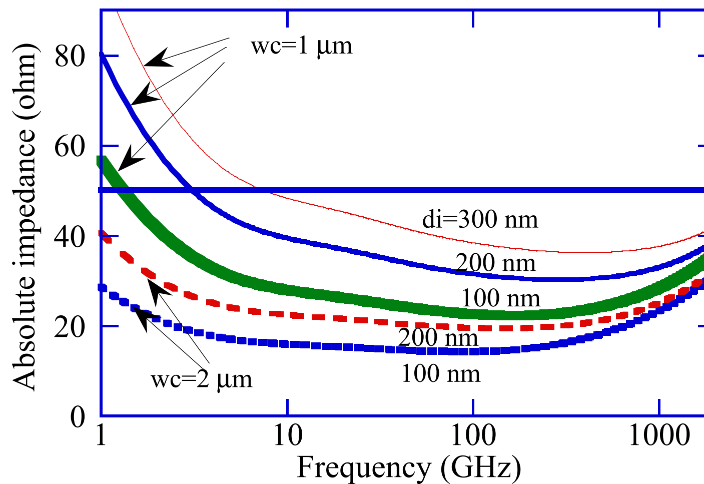

Figure3.1b. The characteristic impedance v.s. frequency at different waveguide width and depletion thickness

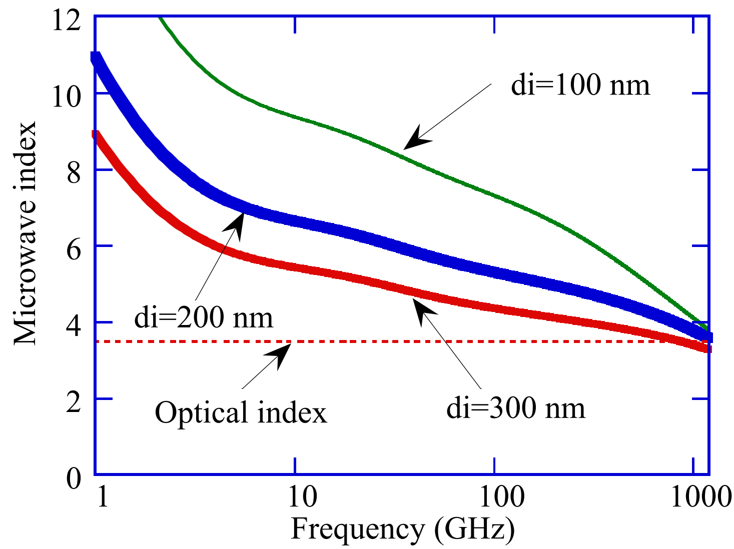

Figure3.2. The microwave index v.s. frequency for different waveguides

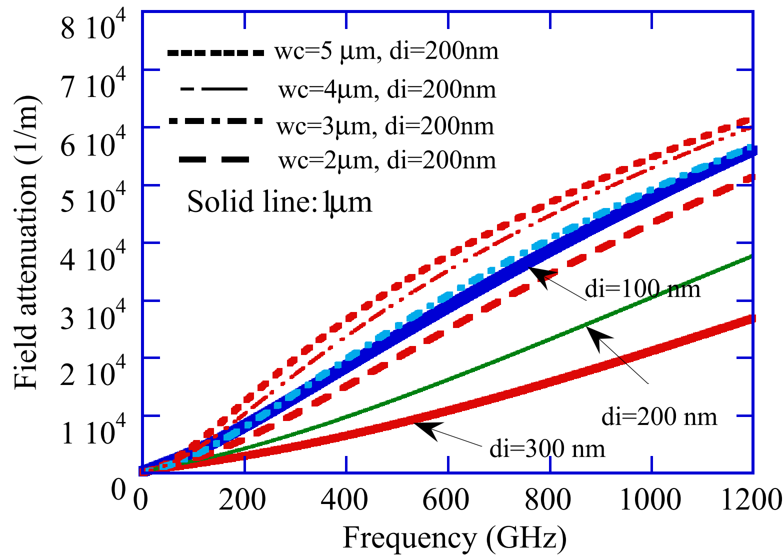

Figure3.3. The microwave field attenuation at different intrinsic region

As discussed in Chapter 2, the p-i-n microwave waveguide has high microwave loss due to the metal skin effects and the doped material. Figure 3.3 plots the field attenuation versus the frequency at different widths and intrinsic regions. The solid curves of Figure 3.3 represent the field attenuation for the

waveguide width $w_c = 1\mu m$ at different intrinsic region thickness $d_i = 100 \sim 300$ *nm*. The dashed curves depict the loss for the waveguide intrinsic region $d_i = 200$ *nm* at different widths $w_c = 2 \sim 5\mu m$. While the width increases or the depletion region becomes thinner, the higher load capacitance will bring up the higher electric field attenuation. The way to minimize the microwave loss is to decrease the load capacitance of the waveguide. The absorption coefficient of the bulk GaAs for the luminescence above the bandgap is around $1\mu m^{-1}$. From the optical confinement factor in Figure 3.4, the corresponding optical absorption length is in the order of 1 to 10 μm.

Let's take an example, (say $10\mu m$ long, $w_c = 1$ μm waveguide with intrinsic region thickness $d_i = 200$ *nm*), the bandwidth roll-off due to the microwave loss is near 3 dB up to 1000 GHz. Considering the dispersion effects, the pulse broadening due to the walk-off problem is below 300 fs (from Figure 3.3 and Equation 2.13). The loss problem is more serious than the dispersion effects in this case.

Regarding to the above discussion, lowering the load intrinsic capacitance is the key point to improve the device bandwidth by *matching velocities*, *matching impedance* and *making low loss*. Figures 3.1, 3.2 and 3.3, shows that to bring the bandwidth as high as possible without the optical diffraction limitation, the best way is to choose the waveguide as 1 μm wide.

(b) Determination of depletion thickness d_i

To determine the thickness of the depletion region, it is necessary to consider the problems coming from the quantum efficiency and bandwidth. Although setting the thicker intrinsic region can bring a higher bandwidth of the

transmission line, the factor of t_l / t_t (Equation 3.1) will be dropped due to the longer transit time across the intrinsic region. So, d_i need to be optimized.

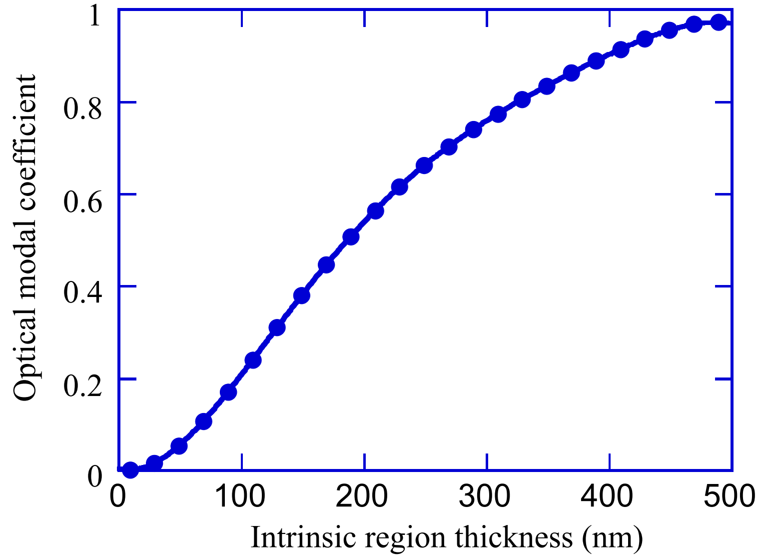

Figure3.4. The optical modal coefficient v.s. intrinsic region

By using the commercial software beam propagation (BPM)[8], Figure 3.4 draws the relation between the optical confinement factor Γ (TE polarization) and d_i. The optical light is TE polarized. The Γ factor shows quite a dependence on d_i such that the corresponding modal absorption length $(1/\alpha\Gamma)$ will have a large range over $d_i < 200\ nm$, i.e. the photodetector length should be long to get a high portion of light absorbed in the small Γ regime.

The bandwidth-efficiency product (Chapter 1) is a figure-of-merit to optimize device performance. Figure 3.5 plots the relative quantum efficiency (solid) and the –3dB bandwidth (point) of 1 μm wide, and 10 μm long TWPD. The LT-GaAs is assumed as the active region. The carrier lifetime is dominated in the response of the intrinsic region (Equation 4 of Chapter 2) instead of the carrier

transit time. The total optical coupling efficiency is assumed. As shown, a maximum value of efficient near $d_i \sim 80\ nm$, where the optimum condition is due to the compensation of two effects, namely the optical modal coefficient Γ and the t_l / t_t.

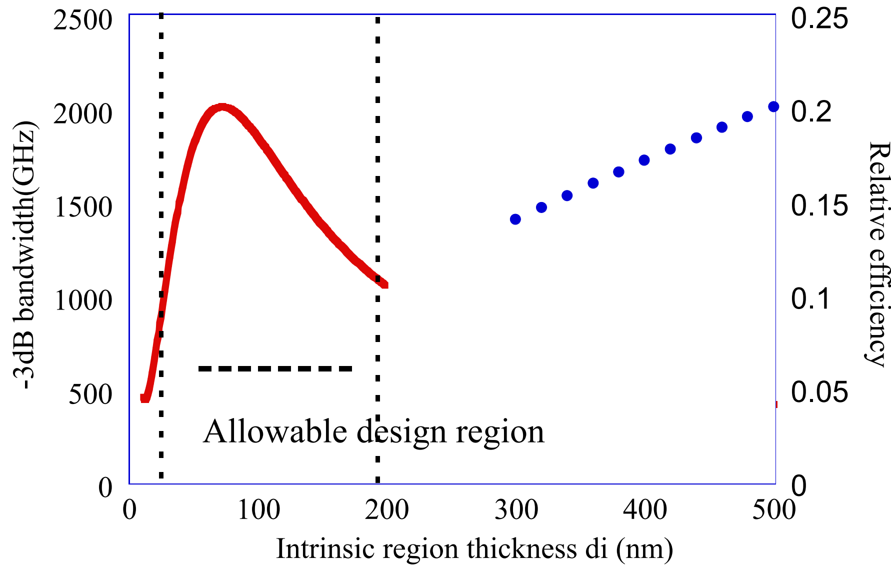

Figure3.5. The -3dB bandwidth and efficiency with intrinsic region waveguide width=1 μm, length=10 μm

In the thin intrinsic region, the value Γ is not high enough so that the optical power can not be completely absorbed. Inversely, in the thick intrinsic region, because of the long carrier transit time, the value t_l / t_t is small. Let's assume the allowable design zone for the intrinsic region thickness with which the quantum efficiency is higher than the half of peak value, as shown in Figure 3.5. For a conservative design to ensure the optical power is completely absorbed and the high bandwidth, we set the thickest intrinsic region (~170 to 190 nm) in the allowable design regime. To investigate the dependence on device length, Figure 3.6 draws the bandwidth-efficiency product as a function of intrinsic region

thickness at different lengths. For the waveguide with $d_i = 170\ nm$, above 99% of the optical power can be absorbed in the length of 10 μm. When the device is much longer than the optical-microwave interaction region (>10 μm), the microwave power will loss during transmission. By compensating the efficiency and the bandwidth, the length of device is set at 10 μm.

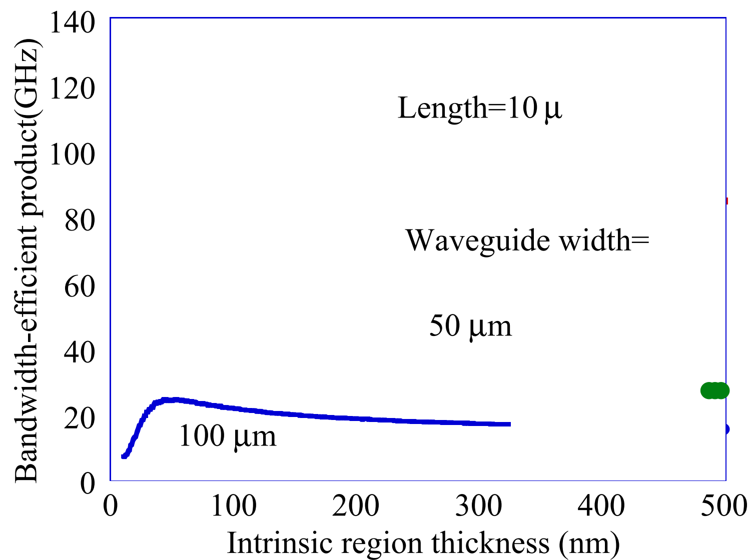

Figure 3.6. The bandwidth-efficiency product at different intrinsic regions.

(c) Discussion about carrier lifetime and transit time:

In material response, two limitation regimes (the carrier lifetime and transit time limit) have different considerations on design. In the carrier transit regime, because the carrier transit time is inversely proportional to the intrinsic region thickness. The material response is inherently dependent on the transmission line design (microwave velocity and impedance), i.e. there is, in this case, one more parameter constraining with the TWPD speed (Equation 2.10). Actually, the transit time effect with the bandwidth of circuit is a trade-off relation. The thinner the intrinsic region, the faster the carrier sweeping across the junction, but the slower the response due to the higher loaded capacitance. While increasing the intrinsic

region thickness to bring the lower load capacitance, the carrier transit time is longer.

On the other hand, while the material performance is limited by carrier lifetime, the material response will not be correlated with the device dimensions. Figure 3.7 depicts the total bandwidth of TWPD as function of intrinsic region thickness at different material response. The waveguide is $1\mu m$ wide and $20\mu m$ long. The dotted curve (carrier transit effects) shows an optimum condition peaking at $d_i \sim 50\ nm$ due to the compromise of transit time and circuit effects. By putting the carrier lifetime on the response, the bandwidth is followed by the TWPD circuit effects and saturated at the carrier trapping limitation. The solid curve of Figure 3.7 shows a monotonically increasing bandwidth.

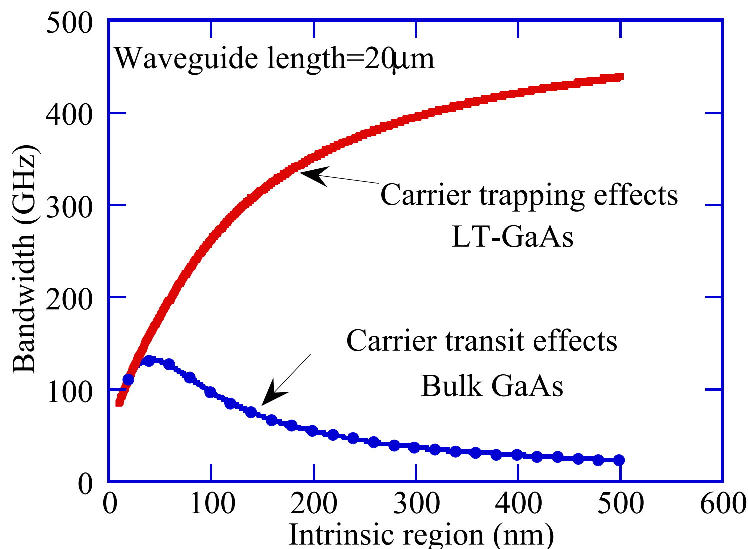

Figure3.7. Two different approaches for the material response.

By this calculation, in the general bulk semiconductor material, the bandwidth is often limited by the carrier transit and the circuit design. This is why most photodetectors can not push the bandwidth higher than two hundred GHz by either improving the RC limitation [9,10] or designing the traveling structure [11].

It is instructive to set the LT-GaAs material as intrinsic regions by utilizing the high carrier-trapping rate. The selection of material response is only dependent on the other fabrication, like material annealing and growth temperature. It is an advantage over the general carrier transit time limit device.

3.2 Material design

Choosing LT-GaAs p-i-n heterojunction as the material structure of p-i-n, the idea is originated from the fabrication of LT-GaAs MSM-photodetectors. In the 1996, I involved in the project of fabricating high-speed photodetectors [38]. Before that, I grew several types of structures (InGaAlAs material), for example, the InGaAs strain quantum-well laser structures and the GaAs quantum-well photo luminescence samples. From these experiences, I learned some techniques to improve the epilayers properties, like doping offset problems (Be) and superlattice layers to block the defect-diffusion. It is very helpful to design the LT-GaAs p-i-n structure.

At the beginning of this project, three attempts of LT-GaAs material growth on the S.I. GaAs wafers were done. Among these growths, the RHEED pattern became spotty after deposing several hundreds of nm. It was found that the roughness of the AlAs blocking layer before lowering the substrate temperature causes the abnormal LT-GaAs. Smoothing of the surface can be done by growing about 10 nm of GaAs [39]. The four generation of LT-GaAs was thus successfully made.

On the fourth generation of LT-GaAs material, the pump-probe measurement and MSM photodetector were made to calibrate the material. By *ex-situ* annealing at different temperatures, a subpicosecond decay rate was obtained from the samples annealed at temperature < 625^0C. Three generations of MSM structures were also fabricated on this wafer to test the dark current and photocurrent. However, it was found that a good Schottky contact was not easily made on the top of LT-GaAs layers. The fabrication of contacts (ohmic or

Schottky) between metal (Ti/Au) and LT-GaAs is not reproducible from generation to generation at the same annealing temperature and even from samples to samples on the same processing. The hole-pile-up problems at the interface [40,41] may be deleterious to the device speeds. Therefore, after about 8 months, we decided to fabricate the alternative structure, i.e. the LT-GaAs p-i-n structure. The LT-GaAs is sandwiched by n- and p-AlGaAs cladding layers. Using heavily doped AlGaAs material, the contact-problems can be improved. The previous work on the high-speed photodetectors in our group [9,11] indicated that the graded layers could eliminate the charge trapping effects on the i-layer and the cladding layers.

The details of material structure design and processing are described in this section and next section.

(a) epilayer structures:

As discussed in Section 3.1, the optimum conditions for designing the optical confinement factor are the $1\mu m$ wide waveguide (Figures 3.1, 3.2 and 3.3) and 100 nm to 200 nm thick intrinsic region (Figure 3.5). In determining the cladding layers of waveguide, the bulk Ga/AlAs material characteristics must be considered.

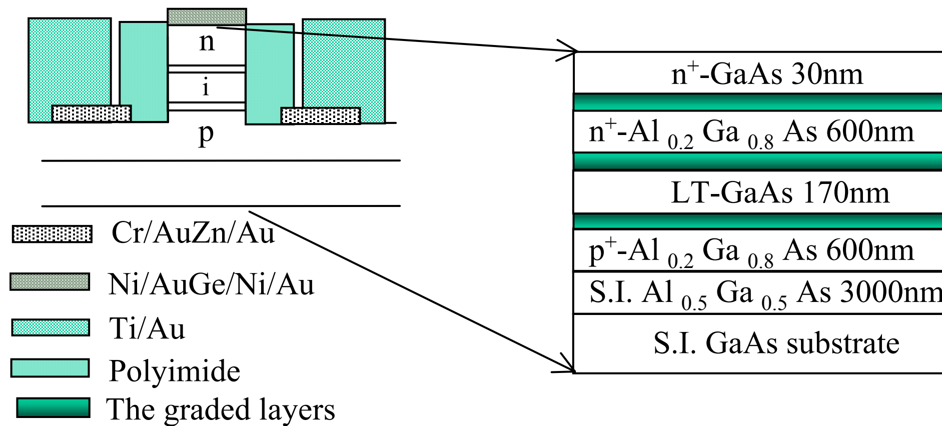

Figure3.8. The schematic drawing of TWPD and material growth

All the material is grown in a Varian GenII solid source molecular beam epitaxy (MBE) system on a (100) oriented semi-insulating GaAs substrate (S.I. GaAs). The semi-insulated wafer can have a very low parasitic capacitance to avoid any unwanted electrical connection. Figure 3.8 plots the AlGaAs material p-i-n heterostructure (the i-layer is grown by LT-GaAs). Before the onset of growth, the wafer is set to 630°C for 5 to 10 minutes to desorb the surface oxide under the As_2 overpressure of 9×10^{-6} torr. The wafer is then cooled down to 570°C to begin the growth. A 300 nm thick buffer GaAs layer is then grown to smooth the surface. Before growing the p-i-n waveguide structures, a 300 nm AlAs and $3\mu m$ $Al_{0.5}Ga_{0.5}As$ layers are deposited. The AlAs is for the etch stop during the removal of the substrate. Although the substrate removal may not be necessary, however, it can increase the flexibility for the processing and the measurement.

A $3\mu m$ $Al_{0.5}Ga_{0.5}As$ growth is completed by the digital alloy method [12~14], which uses the alternating layers of 1 nm AlAs and 1 nm GaAs, i.e. a periodic superlattice of AlAs/GaAs. By this method, we use bandgap engineering and well approximate the AlGaAs alloy (the analogy alloy)[13,15,16]. Also as in the reference [17,18], the periods of superlattice AlAs/GaAs can tailor the optical waveguide properties of the device. There are several reasons for the digital alloy $Al_{0.5}Ga_{0.5}As$. *The first* is to separate the optical mode of p-i-n waveguide from the bottom GaAs substrate, because the S.I. GaAs substrate and the intrinsic region have the same energy bandgap and optical refractive index. *The second* is to eliminate some charges generated in the bulk GaAs. These may induce photocurrent, which will contribute the long tail in the pulse response [19], although the electrical field is almost confined in the intrinsic region. *The third reason* is that the superlattice (AlAs/GaAs), according to the references [20,21], can smooth the surface strikingly after growing several periods of superlattice and can trap the defects originated from the substrate. It is then ensured that the good quality of material can be grown after these layers.

The p-i-n GaAs/AlGaAs double heterostructure structure, as shown in Figure 3.8, includes the doping AlGaAs cladding layers, the LT-GaAs intrinsic layers and the graded layer between the cladding layers and intrinsic layer. The n- and p- regions of p-i-n structure are doped with Si and Be respectively. The optical waveguide is formed by such heterostructure, which includes the lower index and transparent AlGaAs cladding layers. And also, because of the higher bandgap in AlGaAs material, the slow carriers diffusion problems from absorption in the n and p regions of the homojunction can be avoided [22].

The high doping in the cladding layers causes the optical loss, which is mainly resulted from the free carrier and inter-valence-band absorption [42]. In reference [43], the optical loss at λ=1550 nm for p-type GaAs (p=$5\times10^{18}cm^{-3}$) is about 125 cm^{-1} and the one for n-type GaAs (n=$3\times10^{18}cm^{-3}$) is about 12 cm^{-1}. According to [42], the optical loss due to free-carrier absorption increases approximately as λ^3, i.e. the free-carrier absorption is lower at λ=800 nm. However, for the conservative sake, let's take the data at λ=1550nm to estimate the free carrier effects. The optical absorption above bandgap of GaAs is about 1 μm^{-1}. The band-to-band absorption is one order of magnitude larger than the free carrier absorption. Considering the optical confinement in the waveguide, only small portion of optical power loss in the cladding layers. Therefore, at the short wavelength regime, the optical loss due to free-carrier absorption below the doping level of $3\times10^{18}cm^{-3}$ can be neglected.

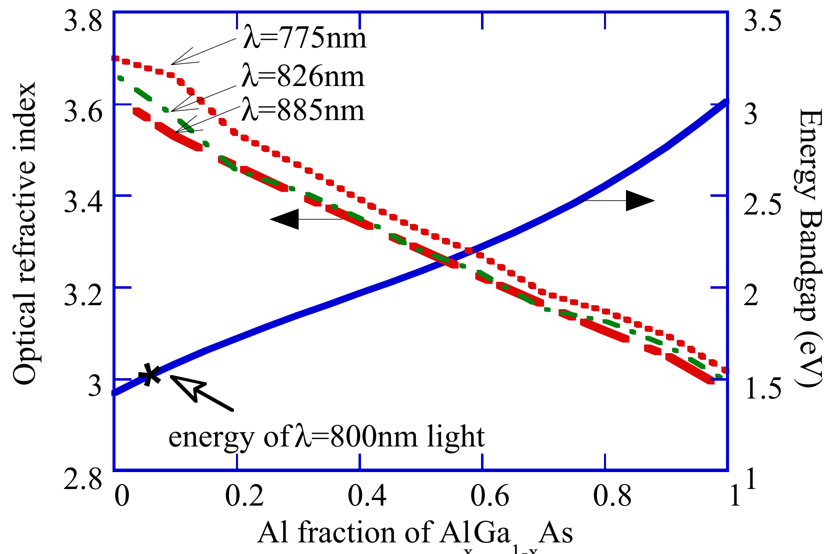

Figure 3.9. The AlGaAs refractive index and energy bandgap for different compositions.

In choosing the Al content of doped AlGaAs cladding layers, one needs to consider two factors. *One* is that the Al should be high enough to be transparent for the light at λ=800 nm and have lower index to support the optical waveguide mode. *The other* is the doped AlGaAs should have high enough mobility and good contacts for the metalization, in that the Al content should be low. Figure 3.9 plots the optical refractive index and energy bandgap of $Al_xGa_{1-x}As$ [23]. The star point (*) is the energy of optical light with wavelength 800 nm, where the equivalent Al content is around 7%, which is the bottom line for the heterojunction to separate the optical absorption from the active region. In the electro-optic sampling measurement, the mode-lock optical pulse is around 100 fs (the corresponding optical bandwidth is around 10 nm). In order to keep the cladding layers transparent to the optical pulse and the bandgap energy of the intrinsic region still lower than the optical energy, it is better to set the optical bandwidth is one order larger than 10nm, say at 100nm. At this condition, the Al content is higher than 20%. The electron mobilities of $Al_xGa_{1-x}As$ have not significantly changed in the compositions of $0<x<0.2$, but, the hole mobilities drop abruptly as x increases [23,24]. So, we keep the Al content of $Al_xGa_{1-x}As$ as low as possible to make low

material resistivity and contact resistance. From the above discussion, to design the low contact resistance of metalization and the low cladding resistance, the choice of AlGaAs is set to 20%.

The LT-GaAs material is grown as the intrinsic region. As mentioned in Section 3.1, in the transit-time limited photodetectors, the device bandwidth inevitably suffers from the trade off between carrier transit time effects and the distributed RC effects (Figure 3.7). On the other hand, if by a choosing suitable material that can operate in the carrier trapping time region, the design then has one more degree of freedom. Using LT-GaAs as the absorption material is to obtain the ultra short carrier lifetime [25-27]. The high concentration of defects in the LT-GaAs result from the excess As, Ga vacancies and As interstitial defects. The carriers are easily trapped in these levels and thus have short carrier trapping time.

The carrier lifetimes of LT-GaAs can be engineered by either growth temperature or annealing temperature [25,27]. We chose 215-230°C as the growth temperature (the variation is due to thermocouple sensor). Following the growth, the layers are *in-situ* annealing at 600 ^{o}C under an As_2 overpressure in the MBE chamber for about 10 minutes. There are two reasons for setting 600 ^{o}C as the annealing temperature. *One* is that there are n-type AlGaAs layers to be grown after LT-GaAs. To grow a good quality of n-AlGaAs, the temperature should be high (generally higher than 550°C), but in order to keep the defects of LT-GaAs in intrinsic region, the growth temperature after LT-GaAs should be kept lower to "freeze" the defects. *The other* reason is that from the pump-probe measurement for different annealing temperatures of LT-GaAs, the layers of 600 ^{o}C annealing show a single and fast decay rate (around 200~300 fs) in the LT-GaAs material grown at the same growth temperature as p-i-n structure [37]. The different carrier decay rates (different carrier trapping time and lifetime) will make the speed of the device slow.

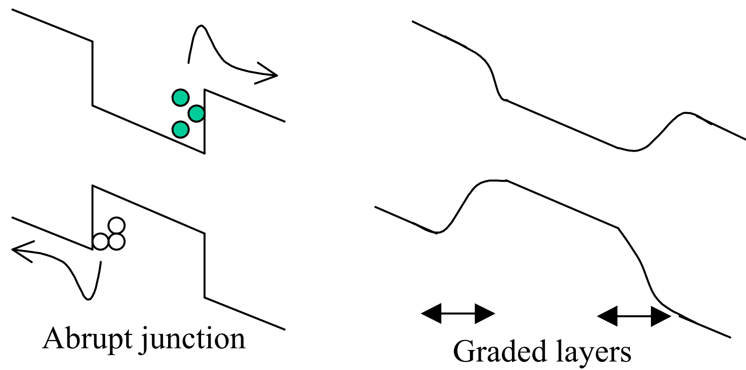

Figure3.10, the graded layers are used to smooth the abrupt heterojunction

In the junction of LT-GaAs and the n-, p- $Al_{0.2}Ga_{0.8}As$, there are some effects that should be considered. *The first* is that the graded heterojunction is necessary for avoiding the carrier trapping in the abrupt junction, as shown in Figure 3.10. To simplify the graded layers, we used the digital alloy techniques, by which the graded heterojunction can well be resembled [29]. Ten periods of superlattice $(AlAs)_y(GaAs)_{1-y}$ y=0~0.2 (each period has 2nm thick) are grown. *The second* is that the outdiffusion of defects from the LT-GaAs to the cladding AlGaAs material need to be avoided [30]. During the growth of top n-cladding and the *in-situ* annealing, the high temperature (about 600^oC) will cause the defects outdiffused to the cladding and may ruin the doping region. Two AlAs layers sandwiching the LT-GaAs material can set barriers for the defect [31]. Two 1.5 nm thick AlAs are deposited before and after growth of LT-GaAs.

Table 3.1 shows the total material growth. In order to check the optical mode in the waveguide geometry (Figure 3.8), the BPM software [8] is used to calculate the optical mode profile. The optical wavelength is set at 850 nm. The waveguide is $1\mu m$ wide with a 170 nm thick intrinsic region (Figure 3.5). The process is assumed to etch through the intrinsic region to 200 nm deep into the p-type-cladding layer. Figure 3.11 depicts the optical power contour of the

fundamental mode. The unit for the x- and y- axis is micrometer. The mode reveals a $1\mu m$ diameter size and is well confined in the waveguide.

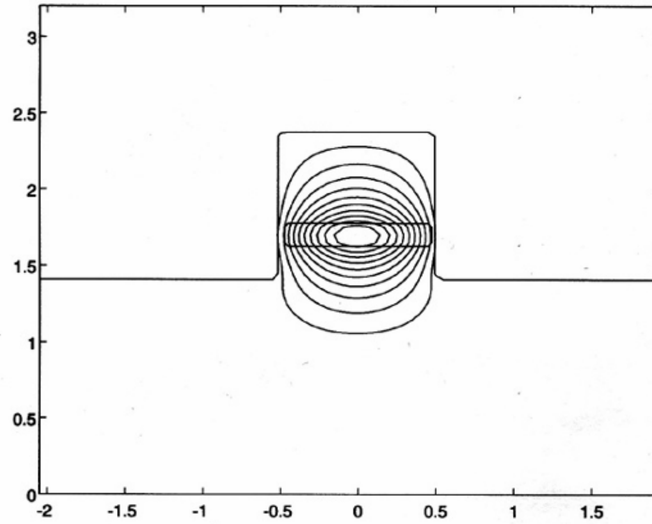

Figure 3.11, the optical mode profile form the BPM method.

Table 3.1 lists the material growth structure. The top GaAs layer (#19) is for the ohmic-contact of center electrode metalization. Also, with this cap layer, the oxidation of n-AlGaAs can be prevented. Undoped layers of AlGaAs layers are grown in both sides near the intrinsic region (#13~16, #7~10). They are the doping offset layers, by which the dopant diffusion to intrinsic region can be avoided. The diffusion constant of Be is around ($1\times10^{-17} cm^2/\sec$ at T=570°C) and Si's is around one order less than the Be's in the GaAs material [31]. The growth rate of AlGaAs is set at $1\mu m/hr$. After annealing the LT-GaAs, there are about $0.6\mu m$ thick n-type AlGaAs material to be deposited at substrate temperature 570°C. So the corresponding diffusion length ($\sqrt{D\cdot t}$) of Be is in the order of 100 nm, and the Si's is around 30 nm. The #11 layer is the space region for smoothing the surface during cooling the substrate temperature to 215°C.

3.3 Device fabrication:

Figure 3.12 schematically plots the details of processing. Generally, the device is separated by two parts, namely (1) the p-i-n region, (2) the output CPW load circuit. The processing is done by the self-alignment technique on the semi-insulate wafer [11,32]. *The first part* is defined on small regions (typically in the area of $100\mu m \times 20\mu m$), which are made by n- and p- contact metalizations and the reactive ion etching between the processes of n- and p- contact. *The second part* is the signal-loaded circuits (CPW lines) at the outside of p-i-n region. After finishing *the first part*, ion-implantation is used to render the area of output load circuit semi-insulating. By bridging through polyimide, the CPW line is connected to the p-i-n photodetector region to receive the microwave signal and also used for the EO-sampling measurement. The polyimide is used for the passivation of the etching surface.

Table 3.1 The material growth structure. T_g: the growth temperature, T_a: the annealing temperature.

#	Material	Doping level	Thickness	Description
19	N^+-GaAs	$8\times10^{18} cm^{-3}$	20 nm	For the ohmic contact, T_g=570°C
18	N^+-$Al_{0.2}Ga_{0.8}As$	$3\times10^{18} cm^{-3}$	400nm	Top cladding layers, T_g=570°C
17	n-$Al_{0.2}Ga_{0.8}As$	$1\times10^{18} cm^{-3}$	180nm	Top cladding layers T_g=570°C
16	$Al_{0.2}Ga_{0.8}As$	Undoped	20nm	Top cladding layer, n-doping offset, T_g=570°C
15	Graded layers	Undoped	20nm	From 0% Al to 20% Al, T_g=570°C
14	GaAs	Undoped	5nm	The *in-situ* annealing cap layer, T_g=350°C
13	AlAs	Undoped	1.5nm	Top diffusion barrier of excess As, T_g=370°C
12	LT-GaAs	Undoped	160nm	Tg=215 °C (by thermal couple), T_a=600°C
11	GaAs	Undoped	10nm	Surface smoothing layers, T_g=570°C
10	AlAs	Undoped	1.5nm	Bottom diffusion barrier of excess As, T_g=570°C
9	GaAs	Undoped	5nm	Space layers
8	Graded layers	Undoped	20nm	From 20% Al to 0% Al, T_g=570°C
7	$Al_{0.2}Ga_{0.8}As$	undoped	50nm	Bottom cladding layer, p-doping offset, T_g=570°C
6	p-$Al_{0.2}Ga_{0.8}As$	$1\times10^{18} cm^{-3}$	150nm	Bottom cladding layers T_g=570°C
5	P^+-$Al_{0.2}Ga_{0.8}As$	$7\times10^{18} cm^{-3}$	400nm	Bottom cladding layers T_g=570°C

4	$Al_{0.5}Ga_{0.5}As$	undoped	3000nm	Optical isolation layers
3	AlAs	undoped	300nm	The etching stop layer
2	GaAs	undoped	300nm	Buffer layers
1	S.I. GaAs			Substrate

Wafer cleaning:

The wafer is soaked in ACE, ISO and methanol for around 2 minutes in the ultrasonic. After the nitrogen blows dry, the sample is then baked at 120^0C around 10 minutes for dehydration.

The top metalization:

The wafer is cut into around 1 $cm\times1$ cm square and cleaned by "wafer cleaning". The top n-metalization is made by the double-layer photoresistors and the lift-off technique. By using this procedure, the metal is easily lift-off with sharp edge. The double layer process is:

(1) clean and 120^0C baked in oven for at least 10 minutes.

(2) HMDS spin at 5.5K rpm 40seconds.

(3) photoresistor 825 (first layer) @5.5K rpm 40seconds.

(4) 95^0C baked at hot plat for 1 minute.

(5) flood exposure on the aligner for 7 seconds at UV light power density of $7.5\,mW/cm^2$.

(4) photoresistor AZP4110 (second layer) @5.5K rpm 40 seconds.

(5) photolithography : after removing edge PR, UV light exposure 10 seconds.

(6) development: stirring in the developing solution (AZ400K:D.I. water=1:4) for around 40 seconds. After that, rinse in D.I. water for 20 seconds, nitrogen blow dry and inspection by optical microscope.

(7) continue the step (6) until the development is good.

(8) O_2 descum for 15 seconds at 100W to remove some PR residues in development region..

(9) E-beam evaporation Ni(5 nm)/AuGe(10 nm)/Ni(10 nm)/Au(60 nm)/Ni(100 nm) for the n-type ohmic contact.

(10) The metalization will be lift-off in the ACE by the help of ultrasonic bath.

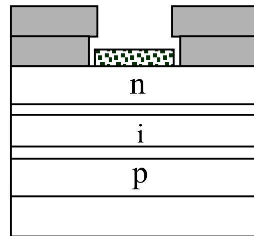

(a) double layer of photoresistor

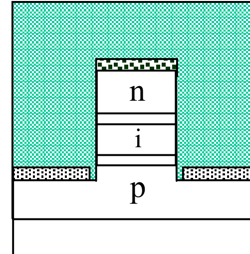

(c) spin polyimide

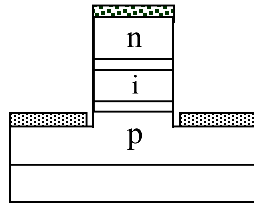

(b)RIE etching and p-metalization

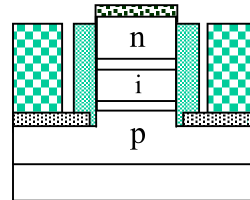

(d)polyimide etching and CPW metal

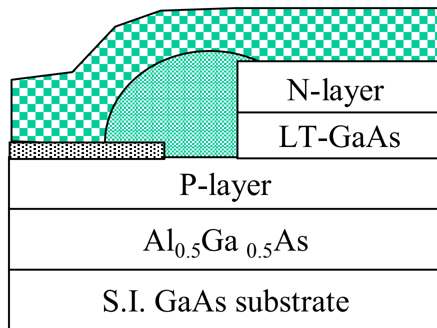

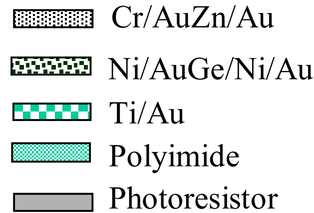

(e)side view of photodector

Figure3-12, the schematic diagram of processing

Reactive ion etching (RIE):

After top metalization, the sample is then placed in the RIE chamber and pumped down below $2 \times 10^{-6} torr$. The self-alignment n-type metalization Ni/AuGe/Ni/Au/Ni is good for ohmic contact after annealing [34]. The top 100 nm Ni is used as an etch mask for RIE etching. Otherwise, the Au layers will be etched and left with rough surface during the plasma Cl_2.

The waveguide widths (generally 1 to 3 μm) are in the same dimension of the ridge depth (about 1 μm) in the high-speed design. The wet etching will get the wedge profiles (inward profile or outward profile) at the different cleavage directions of GaAs. Both directions of wet etching will result in higher intrinsic capacitance or etching through the waveguide by the side-wall etching. So the wet etching is not useful to get the sharp and vertical walls. In order to gain a precise etching and a sharp vertical profile, an *in-situ* measurement and RIE etching are used to form the ridge waveguide. Figure 3.13(a) plots the schematic diagram of RIE etching. A He-Ne laser is used as a light source and monitors a test sample cut from the same wafer as the real sample. There is no processing on the test sample such that the monitoring optical intensity from reflection is from the epilayer itself. The RIE should be through the intrinsic region and stop at around 100 to 200 nm into the p-region. Figure 3.13(b) plots the reflection of optical power from the laser with time. From the different cycles of intensity, the etching surface can be monitored.

The bottom metalization:

After RIE, the sample is rinsed in the D.I. water for at least 10 minutes. This process is for cleaning some Cl_2 residue remaining in the surface after etching. It is important since the remaining Cl_2 will continue to etch to make a rough surface. After that, a cleaning process and photolithography follows the steps in the top metalization. The alloy Cr/AuZn/Cr/Au (6 nm/75 nm/25 nm/600 nm) deposited by thermal evaporation is for the p-type ohmic contact. Both n- and p-contacts are then annealed by the rapid thermal annealing (RTA) at 400^0C for 30 seconds. The voltage-current performance of the p-i-n region should be tested before continuing the next processing. Only if the I-V curve turns out to be normal I-V characteristics of photodiode, then go to the next process.

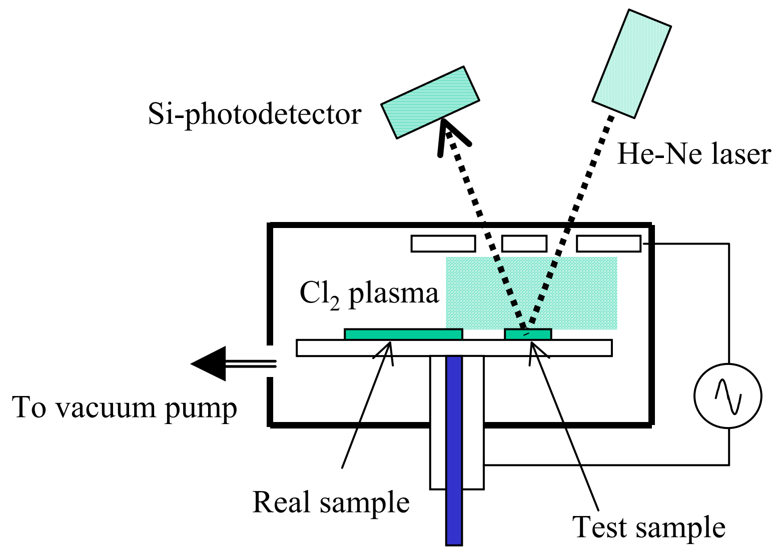

Figure 3.13(a) RIE system and laser monitor

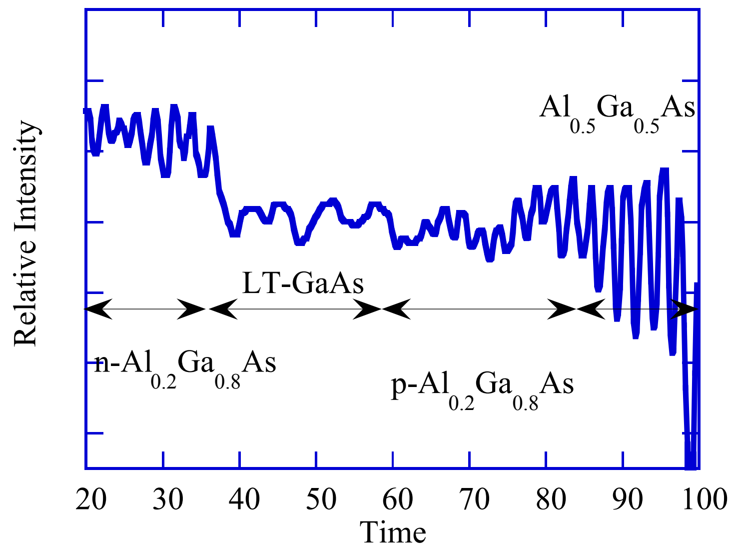

Figure 3.13(b). The laser monitor signal during RIE etching

The ion implantation:

The area of ion implantation is the whole sample except for the region of the p-i-n detector. To do the selected area ion-implantation, a thick PMGI layer is

used for masking the ion. The PMGI processing consists of three layers of SF-15 and is described as follows:

(1) the sample is cleaned by the **wafer cleaning** step, then spin the SF-15 @3.5K rpm 30 seconds.

(2) baked in the oven at 300^0C for around 1 minutes. Each SF-15 layer is around $3\,\mu m$.

(3) inspect the surface by optical microscope to check if there are any bubbles.

(4) repeat (1) to (3)

(5) photolithography : use AZ4330 (5K rpm around 40 seconds) to define the masking region.

(6) use deep-UV light (1000W) to expose for 5 minutes. Then, develop by SAL-101 around 1 minutes and rinse in the D.I. water.

(7) continue step (6) until the PMGI in the region of ion-implantation is totally disappeared.

The ion-implantation is implemented by the proton ion. Three layers of SF-15 and one layer of AZ4330 are used to protect the detector region (p-i-n) from the ion-implantation. The total thickness of SF-15 and AZ4330 is about $11\,\mu m$. The sample is bombarded with proton ion at IICO Corp. The conditions for using ion-implantation are [11,37]:

The offset angle is set at 7 degrees to prevent the channeling effects.

(1) $6\times10^{14}\,cm^{-2}$ at 12 KeV.

(2) $2.3\times10^{14}\,cm^{-2}$ at 30 KeV.

(3) $3\times10^{14}\,cm^{-2}$ at 60 KeV

(4) $3.7\times10^{14}\,cm^{-2}$ at 100 KeV

(3) $4\times10^{14}\,cm^{-2}$ at 150 KeV

(3) $4.5\times10^{14}\,cm^{-2}$ at 200 KeV

The sample is then cleaned by soaking 1165 @90^0C for about 3 hours. Then, we anneal the sample at 350^0C for 30 seconds by the RTA to enhance the semi-insulating.

Passivation and planarizatoin:

As shown in the cross section of Figure 3.12. The polyimide is used for passivating the etching surface and also for planarization, by which the bridges can connect the output CPW line circuits and the p-i-n region.

The processing of the polyimide is as follows:

(1) spin adhesion promoter “QZ3289:QZ3290=1:9”, 5K rpm 50 seconds

(2) spin probimide 284, 5K rpm, 50 seconds

(3) baked in oven and follow the procedure 90^0C for 30 minutes and then 150^0C 15 minutes.

(4) photolithography: use AZ 4330 (5K rpm 30 seconds) and follow the process of **top metalization** to develop.

(5) use RIE (O_2 plasma) to etch pattered polyimide.

(6) clean by ACE, ISO and D.I.

(7) cured in the oven (240^0C for 15 minutes, 325^0C for 60 minutes)

The cured process is for smoothing the polyimide edge after the O_2 RIE etching such that the last metalizaton (output circuit and interconnection lines) can be easier to fabricate. The process for the p-i-n region is finished after this step. Figure 3.14 plots the p-i-n detector region. The dashed curve is for the cleaving to create a mirror facet of waveguide.

Metalization of output CPW and interconnection lines:

As shown in Figure 3.14, the depth profile of the bridge region (point **A** to **B**) is an around 1.2 μm (from the top to the bottom points). The thickness of Ti/Au metal should be thick enough to bridge the metal from the p-i-n regon to ion-implantation region, otherwise the metalization is easily broken in the edge of

polyimide area. And also, the thick metal can have a low resistance and easily be contacted by the microwave probe while doing the measurement. The Ti(20 nm)/Au(1500 nm) is chosen to be the last metalization which is done by the lift-off of the triple layers photoresistors. The process is as follows:

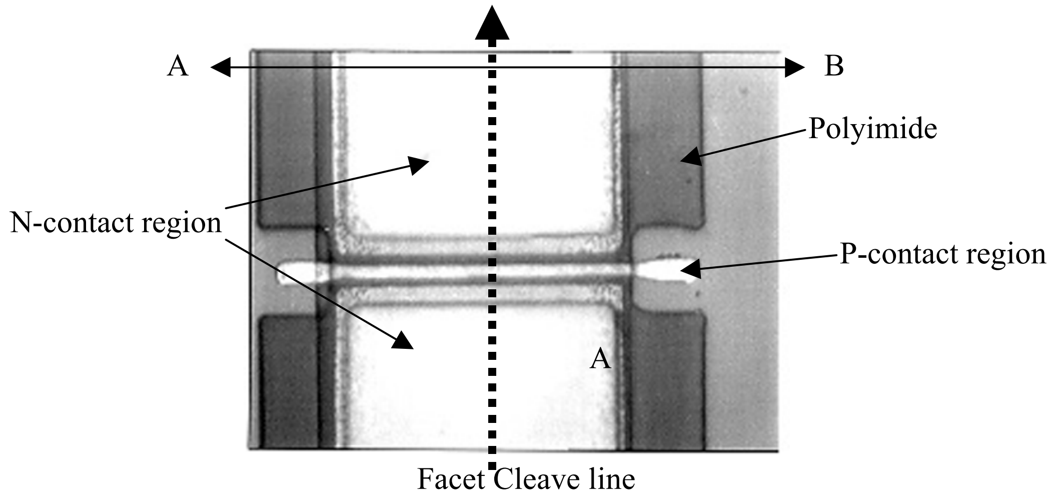

Figure 3.14, the p-i-n region, the dashed line is facet cleaving.

(1) clean and 120^0C baked in oven for at least 10 minutes

(2) HMDS spin at 5.5K rpm 40seconds.

(3) photoresistor 825 (first layer) @5.5K rpm 40seconds.

(4) 95^0C baked at hot plat for 1 minute, flood exposure 7 seconds.

(5) repeat steps (3) and (4).

(6)photoresistor AZ4210 @5.5K rpm 40seconds.

(7) 95^0C baked at hot plate for 1 minute.

(8) photolithography : exposure time 15 seconds.

(9) development: stirring in the developing solution (AZ400K:D.I. water=1:4) for around 40 seconds. After that, rinse in D.I. water for 20 seconds, nitrogen blow dry and inspection by optical microscope.

(10) rinse in D.I. water for 2 minutes. And baked in oven @120^0C for 20 minutes.

(11) Ti(10 nm)/Au(1500 nm) metalization by E-beam evaporation.

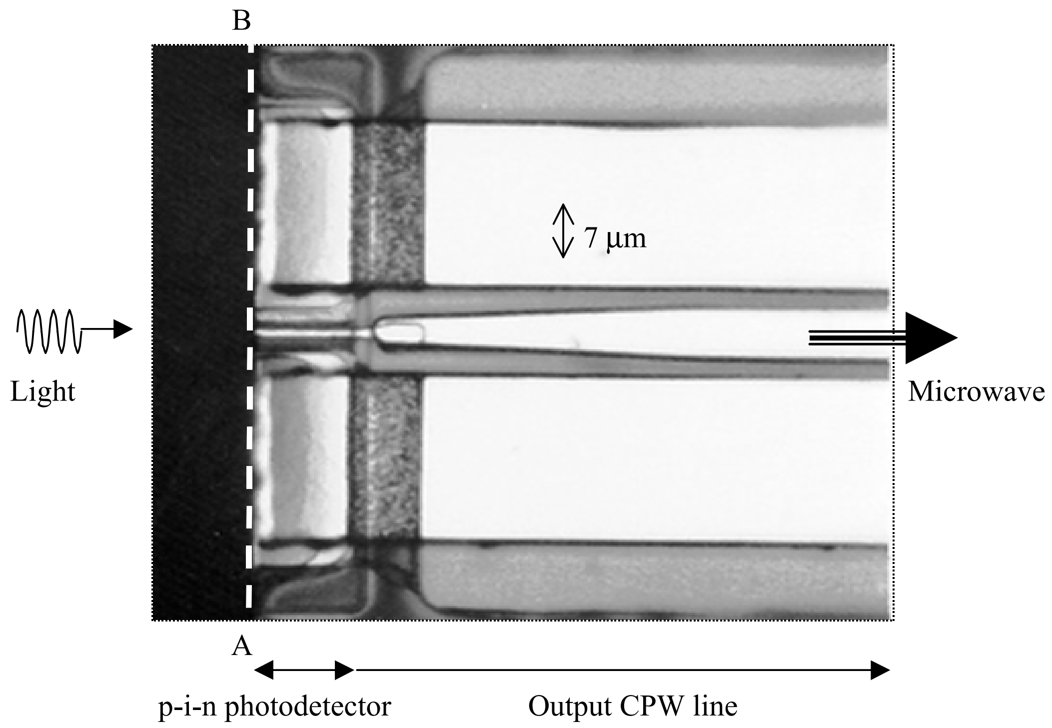

Figure 3.15. The top view of TWPD

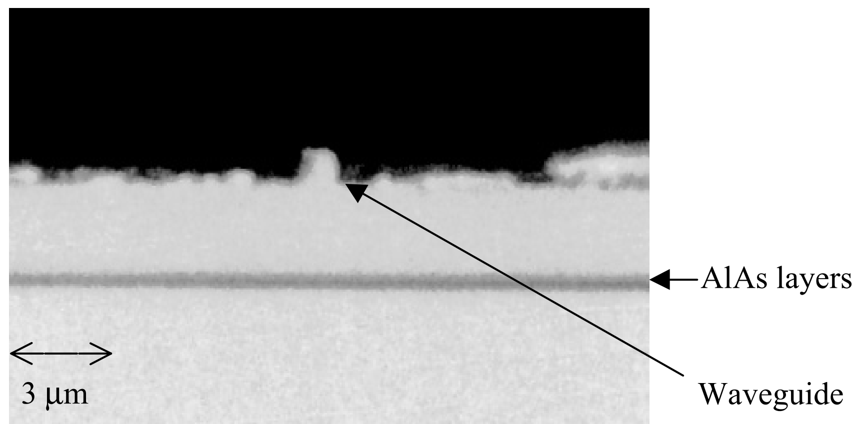

Figure 3.16. The cross section of optical waveguide (point A to B in Figure3.15)

Figure 3.15 shows the top view of the device, which is cleaved from the center of Figure 3.14 (the facet cleave line). Figure 3.16 shows the cross section of waveguide (point A to B of Figure 3.15).

3.4 Summary:

In this chapter, the TWPD structure is designed. From the point views of bandwidth and efficiency, the optimum condition for the intrinsic region is set to 100 nm to 200 nm. The waveguide is set as $1\mu m$ wide. There is one more free degree to enhance the device speed in the design by choosing LT-GaAs as the active region. The material structure and fabrication are also described in this chapter

Reference:

[1]Dan Tauber's, ' Design and performance of semiconductor microstrip lasers', UCSB Ph.D. Dissertation March 1998

[2]Sheng Z. Zhang, Yi-Jen Chiu, Patrick Abraham, and John E. Bowers, "25 GHz polarization-insensitive electroabsorption modulators with traveling-wave electrodes," *IEEE Photon. Technol. Lett*. Vol 11, number 2, p191.

[3]Jackson, R.W. 'Coplanar waveguide vs. microstrip for millimeter wave integrated circuits'. 1986 IEEE-MTT-S International Microwave Symposium Digest 1986. p.699-702.

[4]S. M. Sze, ' Physics of semiconducto devices' second edition.

[5]Harmon, E.S.; Melloch, M.R.; Woodall, J.M.; Nolte, D.D.; Otsuka, N.; Chang, C.L. 'Carrier lifetime versus anneal in low temperature growth GaAs '. Applied Physics Letters, vol.63, (no.16), 18 Oct. 1993. p.2248-50.

[6]Segschneider, G.; Dekorsy, T.; Kurz, H.; Key, R.; Ploog, K. 'Energy resolved ultrafast relaxation dynamics close to the band edge of low-temperature grown GaAs '. Applied Physics Letters, vol.71, (no.19), AIP, 10 Nov. 1997. p.2779-81.

[7]Larry A. Coldren, Scott W. Corzine, ' Diode lasers and photonic integrated circuits'

[8]BPM software

[9]Wey, Y.G.; Crawford, D.L.; Giboney, K.; Bowers, J.E.; Rodwell, M.J.; Silvestre, P.; Hafich, M.J.; Robinson, G.Y. 'Ultrafast graded double-heterostructure GaInAs/InP photodiode'. Applied Physics Letters, vol.58, (no.19), 13 May 1991. p.2156-8.

[10]I-Hsing Tan; Chi-Kuang Sun; Giboney, K.S.; Bowers, J.E.; Hu, E.L.; Miller, B.I.; Capik, R.J. '120-GHz long-wavelength low-capacitance photodetector with an air-bridged coplanar metal waveguide'. IEEE Photonics Technology Letters, vol.7, (no.12), IEEE, Dec. 1995. p.1477-9.

[11]Giboney, K.S.; Nagarajan, R.L.; Reynolds, T.E.; Allen, S.T.; Mirin, R.P.; Rodwell, M.J.W.; Bowers, J.E. 'Travelling-wave photodetectors with 172-GHz bandwidth and 76-GHz bandwidth-efficiency product '. IEEE Photonics Technology Letters, vol.7, (no.4), April 1995. p.412-14.

[12]E.H.C. Parker, 'The technology and physics of molecular beam epitaxy'.

[13]Sundaram, M.; Wixforth, A.; Geels, R.S.; Gossard, A.C.; English, J.H. 'A direct method to produce and measurecompositional grading in Al/sub x/Ga/sub 1-x/As alloys'. Journal of Vacuum Science & Technology B (Microelectronics Processing andPhenomena), vol.9, (no.3), May-June 1991. p.1524-9.

[14]Gossard, A.C.; Miller, R.C.; Wiegmann, W. MBE growth and energy levels of quantum wells with special shapes. Surface Science, vol.174, (no.1-3), (Proceedings of the Yamada Conference XII on Modulated Semiconductor Structures (Second International Conference), Kyoto, Japan, 9-13 Sept. 1985.) Aug. 1986. p.131-5. 6

[15]Harbison, J.P.;Peterson, L.D.;Levkoff, J. ' Precisely controlled compositional gradients in MBE grown AlGaAs/GaAs structures. Journal of Crystal Growth', vol.81, (no.1-4), (Fourth International Conference on Molecular Beam Epitaxy, York, UK, 7-10 Sept. 1986.) Feb. 1987. p.34-7.

[16]Giugni, S.; Tansley, T.L. 'Molecular beam epitaxy growth and physical characterization of precise, narrow, triangular heterostructures using an analog grading algorithm'. Journal of Vacuum Science & Technology B (Microelectronics Processing and Phenomena), vol.9, (no.6), Nov.-Dec. 1991. p.2805-13.

[17]Trivedi, D.A.; Anderson, N.G. Modeling the near-gap refractive index properties of semiconductor multiple quantum wells and superlattices. IEEE Journal of Selected Topics in Quantum Electronics, vol.2, (no.2), IEEE, June 1996. p.197-209. 62 references.Language: English.

[18]Kahen, K.B.; Leburton, J.P. 'Structure variation of the index of refraction of GaAs-AlAs superlattices and multiple quantum wells'. Applied Physics Letters, vol.47, (no.5), 1 Sept. 1985. p.508-10.

[19]Soole, J.B.D.; Schumacher, H. 'Transit-time limited frequency response of InGaAs MSM photodetectors. IEEE Transactions on Electron Devices, vol.37, (no.11), Nov. 1990. p.2285-91.

[20]Petroff, P.M.; Miller, R.C.; Gossard, A.G.; Wiegmann,W. "Impurity trapping, interface structure, and luminescence of GaAs quantum wells grown by molecular beam epitaxy. Applied Physics Letters, vol.44, (no.2), 15 Jan. 1984. p.217-19.

[21]Petroff, P.M.; Weisbuch, C.; Dingle, R.; Gossard, A.C.; Wiegmann, W. "Luminescence properties of GaAs-$Ga_{1-x}Al_xAs$ double heterostructures and multiquantum-well superlattices grown by molecular epitaxy". Applied Physics Letters, vol.38, (no.12), 15 June 1981. p.965-7.
[22]V.Diadiuk and S.H. Groves, "Double-heterstructure InGaAs/InP PIN photodetectors," Solid-State Electron., vol.29, no.2, pp229-233,1986
[23]S. Adachi, "Properties of Aluminium Gallium Arsenide".INSPEC 3th edition 1993
[24]Chand, N.; Henderson, T.; Klem, J.; Masselink, W.T.; Fischer, R.; Chang, Y.-C.; Morkoc, H. 'Comprehensive analysis of Si-doped Al/sub x/Ga/sub 1-x/As (x=0 to 1). Physical Review B (Condensed Matter), vol.30, (no.8), 15 Oct. 1984. p.4481-92.
[25]Grenier, P.; Whitaker, J.F. 'Subband gap carrier dynamics in low-temperature-grown GaAs'. Applied Physics Letters, vol.70, (no.15), AIP, 14 April 1997. p.1998-2000.
[26]Lochtefeld, A.J.; Melloch, M.R.; Chang, J.C.P.; Harmon, E.S. 'The role of point defects and arsenic precipitates in carrier trapping and recombination in low-temperature grown GaAs'. Applied Physics Letters, vol.69, (no.10), AIP, 2 Sept. 1996. p.1465-7
[27]Harmon, E.S.; Melloch, M.R.; Woodall, J.M.; Nolte, D.D.; Otsuka, N.; Chang, C.L. 'Carrier lifetime versus anneal in low temperature growth GaAs '. Applied Physics Letters, vol.63, (no.16), 18 Oct. 1993. p.2248-50.
[28]Brown, E.R.; McIntosh, K.A.; Nichols, K.B.; Manfra, M.H.; Dennis, C.L. 'Optical-heterodyne generation in low-temperature-grown GaAs up to 1.2 THz '. Proceedings of the SPIE - The International Society for Optical Engineering, vol.2145, 1994. p.200-8.
[29]Baskey, J.H.; Rimberg, A.J.; Yang, S.; Westervelt, R.M.; Hopkins, P.F.; Gossard, A.C. Remotely-doped superlattices in wide parabolic GaAs/Al/sub x/Ga/sub 1-x/As quantum wells. Applied Physics Letters, vol.61, (no.13), 28 Sept. 1992. p.1573-5.
[30] Yin, L.-W.; Hwang, Y.; Lee, J.H.; Kolbas, R.M Trew, R.J.; Mishra, U.K. Improved breakdown voltage in GaAs MESFETs utilizing surface layers of GaAs grown at a low temperature by MBE. IEEE Electron Device Letters, vol.11, (no.12), Dec. 1990. p.561-3.
[31]E. Fred Schubert , "Doping in III-V semiconductors ", 1993
[32]Apl paper, Specht, P.; Jeong, S.; Sohn, H.; Luysberg, M.; Prasad, A.; Gebauer, J.; Krause-Rehberg, R.; Weber, E.R. "Defect control in As-rich GaAs". Materials Science Forum, vol.258-263, pt.2, (19th International Conference of Defects in Semiconductors. ICDS 19, Aveiro, Portugal, July 1997.) Trans Tech Publications, 1997. p.951-6. 15 references.

[33]Langer, D.W.; Ezis, A.; Rai, A.K. Structure and lateral diffusion of ohmic contacts in AlGaAs/GaAs high electron mobility transistors and GaAs devices. Journal of Vacuum Science &

[34]Hu, E.L.; Coldren, L.A. ‘Recent developments in reactive plasma etching of III-V compound semiconductors’. Proceedings of the SPIE - The International Society for Optical Engineering, vol.797, Jan. 1987 July-Aug. 1987. p.1030-2.

[35]Ralph E. Williams, “Gallium Arsenide Processing Techniques”

[36]Ren, F.; Pearton, S.J.; Hobson, W.S.; Fullowan, T.R.; Lothian, J.; Yanof, A.W. “Implant isolation of GaAs-AlGaAs heterojunction bipolar transistor structures”. Applied Physics Letters, vol.56, (no.9), 26 Feb. 1990. p.860-2.

[37]Private communication with ‘Christoph Kadow’.

[38]This project is named as ‘PRET’ sponsored by the Center for Nonstoichiometric III-V Semiconductors under program No. F49620-95-1-0394.

[39]suggested by Dr. James Ibbetson.

[40]Salem, A.F.; Brennan, K.F. ‘Influence of hot carrier transport on the transient response of an InGaAs/InAlAs metal-semiconductor Schottky diode structure’. IEEE Transactions on Electron Devices, vol.43, (no.4), IEEE, April 1996. p.664-5.

[41]Burroughes, J.H.; Hargis, M. ‘1.3 µm InGaAs MSM photodetector with abrupt InGaAs/AlInAs interface’. IEEE Photonics Technology Letters, vol.3, (no.6), June 1991. p.532-4.

[42]Pankove, J.I., ‘Optical processes in semiconductors’. Dover publication Inc. New York (1971).

[43]Babic, Dubravko Ivan, ‘Double-fused long-wavelength vertical-cavity lasers’, UCSB Ph.D. Dissertation August 1995.

Chapter 4

Experimental Results and Discussion

This chapter describes the measurement results. It is divided into two sections. In the *first* section, the properties of the bulk material and the microwave waveguides are measured and analyzed. In the D.C. measurements, the Transmission Line Model (TLM) is used to characterize the metalization contact and the bulk material resistance. As for the A.C. characteristics, the network analyzer is used to test the microwave propagation in the transmission line. The transmission line impedance, loss and dispersion effects are extracted from the measured scattering parameters (s-parameter). In the *second* section, the TWPD performance is measured. The device bandwidth is first characterized by a digital electrical sampling scope to do the fist testing. Then, the electro-optic sampling technique is applied to measure the device speed. The EO-sampling principle and setup are described in this section. Comparing two different lengths of devices, the microwave propagation constants can be extracted to the frequency much higher than the limitation the network analyzer can provide. The device speed limitation will be discussed in this section, which includes the circuit limitation and the material effects in the LT-GaAs. A power and bias dependent EO-sample is also presented. It is found that the high speed is due to carrier trapping in LT-GaAs material.

4.1 The p-i-n waveguide characteristics:

4.1.1 D.C. characteristics:

As mention in Chapter 2, the contact resistance and bulk material resistivity will effect the relaxation frequency of the material and the transmission line performance. To obtain high speed and high power performance in photodetectors, a good ohmic contact and low material resistivity is needed [1~3].

The current-voltage measurement of the TLM patterns is used to characterize the bulk material and the contact resistance of n- and p- metalization. The TLM patterns are designed with the dimensions of $100\mu m \times 100\mu m$, and the electrode gaps between them are from 2 μm to 35 μm. The top Au layer is deposited at least 500nm thick to ensure a good contact on the probes. HP-4145 is used to measure the I-V characteristics. All the I-V data is not recorded until reaching the reproducibility. After at least three times of measurements for each pattern, the I-V data is taken and averaged statistically. The two probe contacts on the Au surface are also measured to correct the TLM resistance. Two probes are placed as close as possible on the same test pad to measure the contact resistance, in which the resistance of Au layer between two probes is assumed zero. The average resistance of two-probe contact is equal to 2.55 Ω. The resistance of the TLM patter is obtained by subtracting the probe resistance. The relation between the average TLM resistance and the electrode gaps is assumed as a linear function. And, the slope and intercept points of linear relation are obtained by fitting linear curves. The contact resistance of metalization is given by [4]:

$$R = \frac{2R_{sc}L_t}{W} + \frac{R_s}{W}L = 2 \cdot R_c + \frac{R_s}{W}L \quad (1)$$

$$L_t = \sqrt{\frac{r_c}{R_{sc}}} \quad (2)$$

where W, L (unit=μm) are the TLM pattern width and separation. R_{sc}, R_s (Unit $=\Omega$) are the sheet resistance under the contact and the separation regions. L_t: transfer length. r_c:(unit=$\Omega \cdot \mu m^2$) the contact resistance. It is noted that equation (1) is true only at $W >> L_t$. The value of L_t is in the order of 1 to 0.1 μm which is quite smaller than the device width W=100μm, so equation (1) is a good

approximation. To simplify the calculation, the assumption $R_{sc} = R_s$ is used in the TLM pattern measurement.

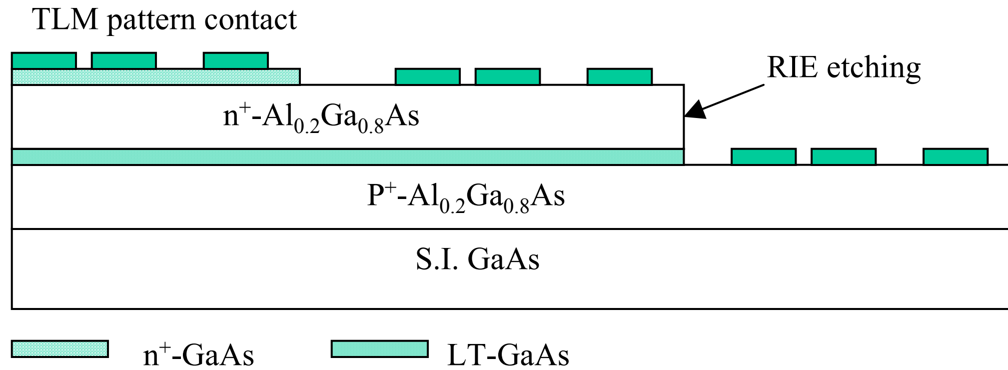

Figure4.1, The metalization pattern for measureTLM resistivity

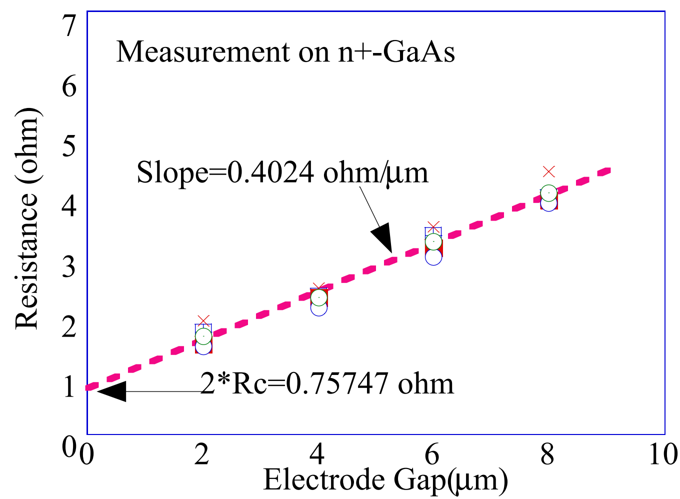

Figure 4.2 The TLM measurement on n+ GaAs

In order to get contact resistance on the different layers of the p-i-n heterostructre (the design of the material structure is in Chapter 3); the sample is cut into four pieces. Each is etched by RIE to different layers of interest. Figure 4.1 plots the schematic diagram for this process. The top surfaces of the three samples are prepared to be $n^+ - GaAs$ layer, $n^+ - AlGaAs$, and $p^+ - AlGaAs$ such

that the metalization contacts can be known. The TLM patterns are then followed by the general lithography techniques to lift-off metalization. Here, the alloys of Ni/AuGe/Ni/Au are annealed at $410^0 C$ and Cr/AuZn/Cr/Au are annealed at $390^0 C$. Figure 4.2 shows the measurement on the $n^+ - GaAs$, which corresponds to the n-contact of TWPD. The contact resistance is about 35.6 $\Omega \cdot \mu m^2$. After the top $n^+ - GaAs$ layer is etched, the TLM pattern is used to measure the resistance of $n^+ - Al_{0.2}Ga_{0.8}As$ layers. Figure 4.3 plots these TLM data on $n^+ - Al_{0.2}Ga_{0.8}As$ layers. The metal contact resistance is increased to around 245 $\Omega \cdot \mu m^2$. The RIE etching is assisted by the *in-situated* measurement to ensure that the etching surface is 200 nm underneath the junction of $n^+ - GaAs$ and $n^+ - Al_{0.2}Ga_{0.8}As$ layers. The contact resistance of AlGaAs is about one order larger the GaAs layer, even the $n^+ - GaAs$ is only 30nm thick. To improve the contact resistance of p-i-n heterostructure and to decrease the amount of oxygen incorporated to the Al, the top contact $n^+ - GaAs$ is necessary. The rest of $n^+ - Al_{0.2}Ga_{0.8}As$ layer is about 400nm thick, such that the average resistivity is 96 $\Omega \cdot \mu m$ (which is calculated by R_s / d, d: $n^+ - Al_{0.2}Ga_{0.8}As$ thickness). Using the same technique, the TLM of $p^+ - Al_{0.2}Ga_{0.8}As$ can also be measured, as shown in Figure 4.4. The metal contact resistance is around 269 $\Omega \cdot \mu m^2$ and the average layer resistivity is 140 $\Omega \cdot \mu m$. The contact resistance and material resistivity are listed in Table 4.1, which are consistent with reference [5,6].

Table 4.1

	$n^+ - GaAs$	$n^+ - Al_{0.2}Ga_{0.8}As$	$p^+ - Al_{0.2}Ga_{0.8}As$
Contact resistance ($\Omega \cdot \mu m^2$)	35.6	245	269
Resistivity ($\Omega \cdot \mu m$)		96	140

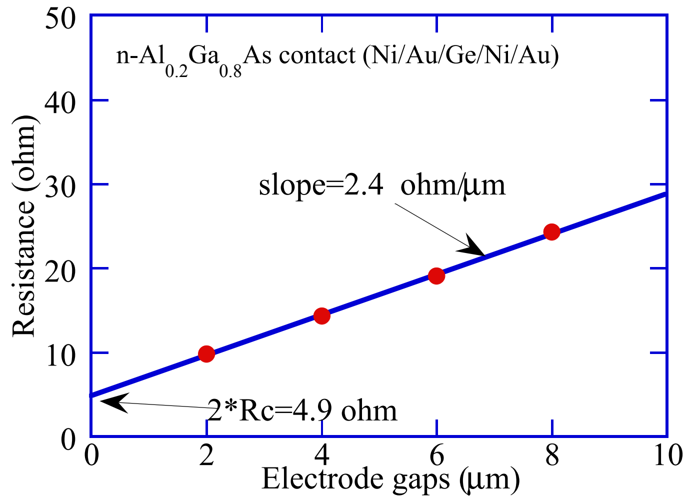

Figure 4.3, TLM measurement on n-$Al_{0.2}Ga_{0.8}As$

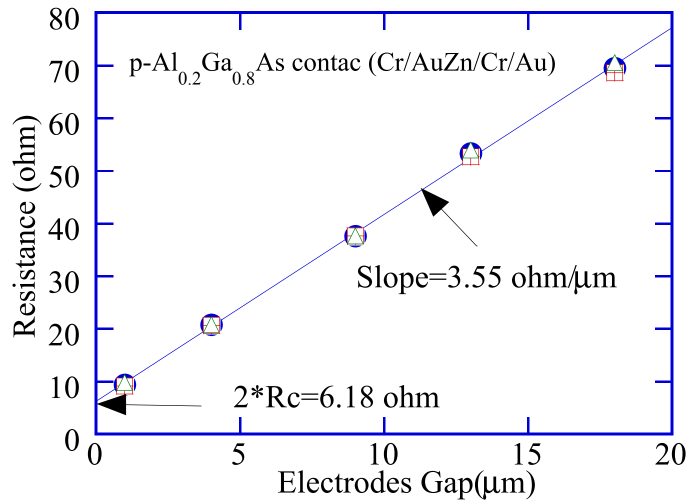

Figure 4.4 TLM measurement on p-$Al_{0.2}Ga_{0.8}As$

4.1.2 A.C. characteristics:

The A.C. characteristics are mainly based on scattering matrix measurements (s-parameters), by which the microwave propagation constant can be extracted [7-9]. In the TWPD structure (or WGPD), the microwave propagation and characteristic impedance are the basic factors effecting the circuit limitation of

the device [10,11]. Generally, the lengths of the TWPD are in the order of 1 μm to 10 μm. In this range, it is hard to measure the s-parameters of waveguides precisely since the calibration of the output contact pads used to connect the microwave probes to the waveguides [12]. To avoid the calibration errors in the measurement, a long p-i-n waveguide without output contact pads is designed and fabricated by the general processes of in-plan laser [13].

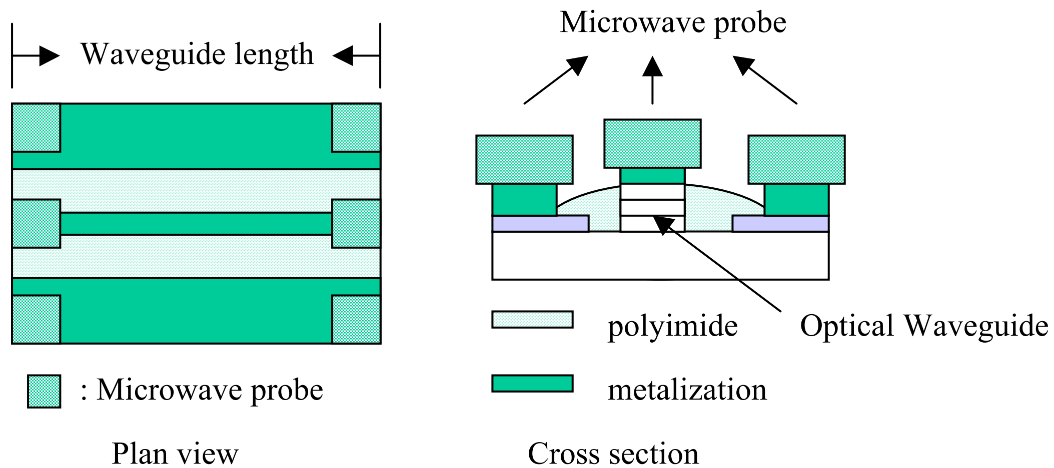

Figure 4.5. The schematic diagram for the scattering parameter measurement

Figure 4.5 plots the schematic diagram of waveguide and measurement. The process is almost the same as for the real device [14] except that there are no output CPW lines. The microwave probes are directly contacted with the metalization, so the TWPD microwave waveguide can be simulated precisely. The sample substrate is lapped to about 100 μm thick. Cleaving on these thinning samples forms the ends of the waveguides. The polyimide is etched by RIE just through the center contact for the microwave probes. The etching surfaces are passivated by polyimide below the n-contact metal. The width of polyimide is patterned so that the center pad of microwave probes will not touch the bottom contacts (p-metalization). Two Picoprobe microwave probes are closely connected both ends of waveguide so that the measurement length is equal to the full

waveguide. The microwave probes are connected with two V-connectors and microwave transmission lines. A HP network analyzer is used to measure the s-parameter. The calibration is done by open, load and through testing circuits on a calibration substrate to shift the measurement points to the microwave waveguide. All the data are averaged 128 times in the frequency range of 45MHz to 50 GHz. Although this is not enough to investigate the frequency domain higher that 50 GHz, it shows the trend of microwave propagation characteristics for different sizes. It also allows us to extrapolate the speed of TWPD and optimize the device structure.

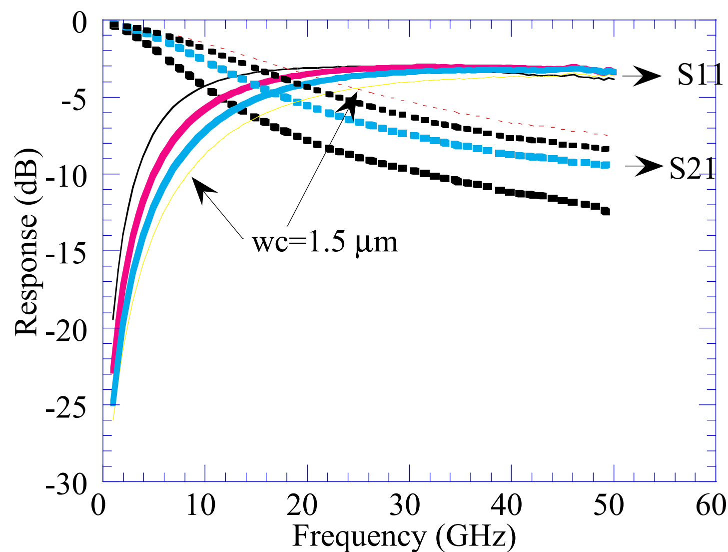

Figure 4.6. The S11 and S21 values at waveguide width, wc=1.5,.2, 4 and 6 µm, S11 (solid cureves from top to bottom), S21 (dash cureves from bottom to top)

The waveguide is 400 μm long. Both n- and p- metalizations include an about 1.5 μm thick Au to ensure a good contact for the microwave probe. About 100 nm thick intrinsic region (LT-GaAs region), n- and p- $Al_{0.2}Ga_{0.8}As$ cladding layers are grown on a S.I. GaAs wafer. Figure 4.6 depicts the S11 and S21 parameters on these p-i-n waveguides at different waveguide widths (wc), which

are 1.5, 2, 4 and 6 μm. Generally, the S11 represents the reflection of the signal from one end of the 50Ω transmission line and the measured waveguide. The reflection coming from the other end of waveguide can approximately be treated as a small reflection for a long waveguide. The solid curves of Figure 4.6 indicate a low S11 values for narrower waveguides. Because the narrower width waveguide has lower intrinsic capacitance, microwave impedance is increased as the width is decreased. The S21 values (the dashed curves of Figure 4.6) show the microwave transmission through the waveguide. The trend of S21 for different widths is that narrower waveguides have lower transmission losses, which increase for higher frequency. Therefore, to get the lowest loss and reflection on the microwave performance, the best design is to make narrow waveguides. The same trends were predicated in the Chapters 2 and 3.

In order to get more details on the propagation characteristics of waveguides, the microwave characteristics are extracted from the s-parameters [9]. By using the s-values of Figure 4.6, the microwave field attenuation factors, microwave index and the waveguide characteristic impedance are plotted on Figures 4.7 and 4.8. As shown in these figures, the flat region of index and impedance over the middle frequency region can be seen on the frequency range above 10GHz. As mentioned in Chapter 2, the velocity and impedance can be well approximated by the inductance (L) and the intrinsic capacitance (C_i) in the microwave waeguide. These two plots indicate that the narrower waveguides have the lower microwave loss, lower index, and the higher impedance. The optimum conditions of TWPD structure should be impedance matched, velocity matched and have low microwave loss. From Figures 4.7 and 4.8, the best choice of TWPD circuit is to make a narrow waveguide. This is why it is necessary to use the narrow waveguide to reach a high bandwidth in reference [15].

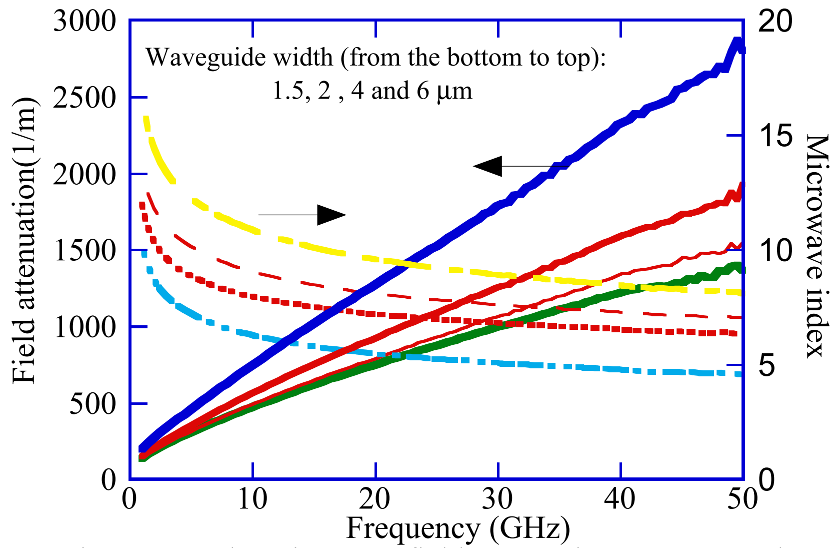

Figure 4.7. The micowave field attenuation constant and microwave index for differnet width of waveguide

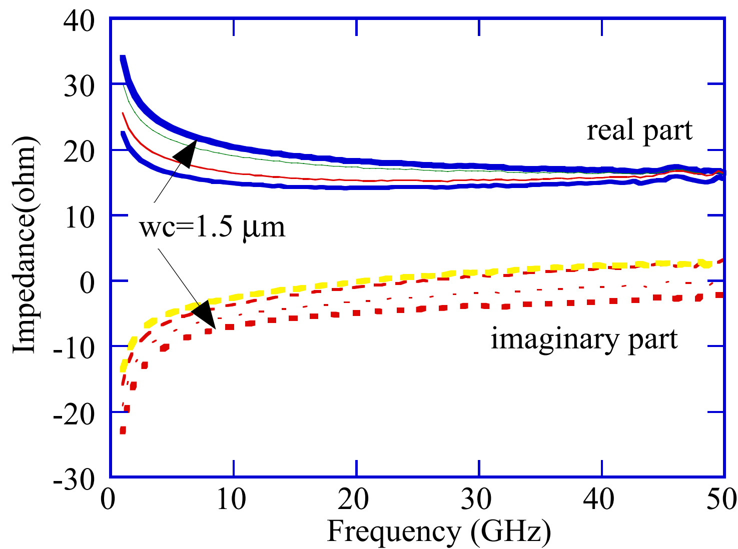

Figure 4.8. The impedance of waveguide at different lengtths. The solid curves are the real part of impedance (from top to bottom), and dashed curves are imaginary part (from bottom to top) with width 1.5, 2, 4, 6 µm

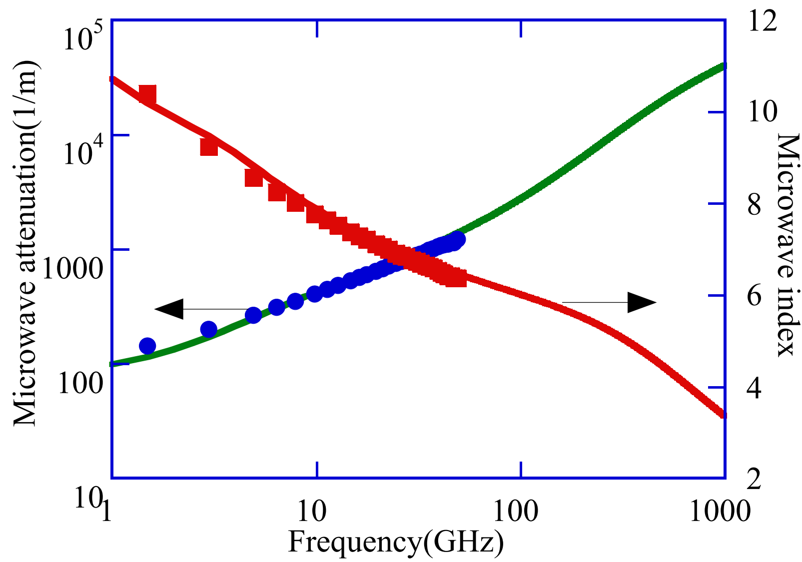

Figure 4.9. The microwave field attenuation and index with frequency The dash curves are the experimental results and the solid curves are the theoretical results

4.1.3 Discussion:

As discussed in Chapter2, the calculated microwave index and characteristic impedance will diverge as frequency approaches to D.C. ($\propto 1/\sqrt{\omega}$). Similar behaviors also observed in the experiment (in Figures 4.7 and 4.8) mean that the transmission of microwave signal approaches infinitely slowly as at low frequency. It is not consistent with the measured photocurrent response in the low frequency [31]. The microwave wavelength is proportion to $1/\sqrt{\omega}$ as $\omega \to 0$. As some points of low frequency, the scale of microwave wavelength is much longer than the device length. For example, as seen in Figure 4.7, the wavelength at 1 GHz is about in the order of $10^4\,\mu m$, which is about two orders larger than the waveguide length. At this point, the voltage and current along the device is almost position independent. The behaviors of the lump-element are dominated in the signal transmission, rather than the wave phenomena. In the practical points of views, the phase change due to microwave transmission of low frequency is small enough to

easily make measurement inaccurate. Therefore, the velocity mismatch or impedance matching are not important in the low frequency [32,33].

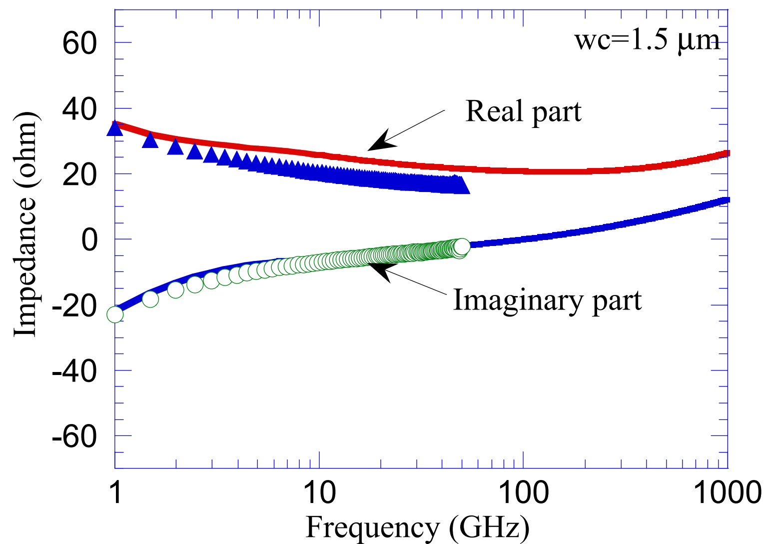

Figure 4.10. Impedance as a function of frequency. The dash curves are experimental results and the solid curves are the theoretical results.

To predict the photodetectors performance at frequency higher than 50 GHz, the equivalent circuit model (Chapter 2) is used to calculate the propagation characteristics at frequency up to 1 THz. The LT-GaAs intrinsic region and waveguide width is set to 100 nm and 1.5 μm. The bulk resistivity and the contact resistance are used in the measurements on the D.C. characteristics. Figures 4.9 and 4.10 plot the field attenuation, microwave index and impedance. The dashed curves are the experimental results for a waveguide width of 1.5 μm. The theoretical results are in good agreement with the measurement. The optical effective index is around 3.5 to 4.5, and the corresponding absorption length is below 10 μm. At 500GHz, the microwave loss for a 10 μm long device is about 2dB loss, the microwave index is about 4 and the impedance is about 25 Ω. To fit the TWPD conditions, the waveguide width need be designed as one micrometer

wide. The impedance of the output CPW line should be lower than 50Ω to lower the reflection at the output of the photodetectors.

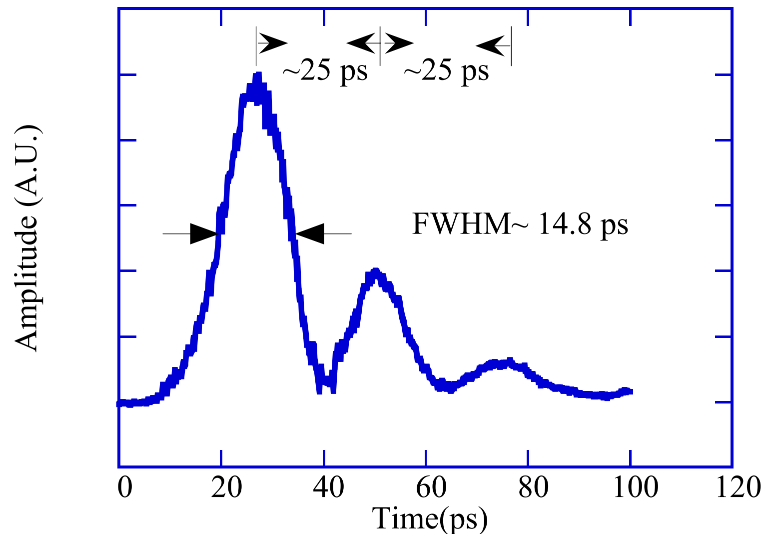

Figure 4.11. The electrical sampling measurement. The multiple reflection from the microwave probe and optical input. The round trip time is around 25 ps.

4.2 The high speed measurement of photodetectors:

4.2.1 Electrical sampling measurement:

Before doing the electro-opto measurements, an electrical sampling is used to do the first test of impulse response. Compared to E-O sampling, the electrical sampling is a simpler check to see if the instrument limits the response of photodetector. A mode-locked Ti-sapphire laser centered at 800nm generates the optical impulses. In the electrical sampling setup, the optical excited signal is taken by a Cascade-microwave-probe with a bias tee (with bandwidth above 40GHz). Through a microwave cable, the probe is then connected to a HP sampling oscilloscope. Typically, the bandwidths of the sampling oscilloscope, microwave cable, cascade microwave probe and the bias Tee are around 40 GHz. If taking the

bandwidth as a Gaussian-like profile, then the impulse response due to the instrument is about 16ps FWHM.

The material growth and device fabrication is following the process described in the Chapter 3. The TWPD region is 10 μm long with 170 nm thick intrinsic region. The n- and p- doped cladding layers are 600 nm thick $Al_{0.2}Ga_{0.8}As$. Figure 4.11 plots the device impulse response shown at the sampling oscilloscope. A 15ps FWHM impulse (the first peak) exhibits, briefly, an instrument-limited response. The impedance of the output CPW lines is designed to be about 40 Ω. As shown, the strong echoes after the main signal are the reflections from the 50 Ω microwave probe. This 800 μm long CPW line means that the corresponding round-trip traveling time is about 25 ps.

4.2.2 Electro-optic pump-probe measurement:

The electrical sampling technique is restricted by the electrical bandwidth of instrument once the photodetector response is up to several picosecond or subpicosecond (> 100 GHz). The optical pump-probe technique is an another alternative way to implement the measurement. By the optical pump probe technique, the measurement limitation is dependent on the optical pulse width. Up to date, the mode-locked lasers with the subpicosecond or even much shorter are the common optical pulse sources for utilizing. Therefore, if a method exists that it can convert the electrical signal to the optical probing pulses, a below subpicosecond regime measurement can be implemented.

With the birefringent crystals, the polarization of optical light will be changed by the applied electrical field [16]. The optical pulse can thus probe the electrical signal. This is the so-called electro-optic pump probe measurement (EO sampling). There are several kinds of crystals that have been applied to electro-optic sampling. For example, the GaAs, InP semiconductor material can be used as internal EO sampling [17]. There is, in this case, no need for other EO crystals.

However, the substrate should be transparent for the optical probe beam, or the bulk substrate needs to be removed [15]. This increases the complexity of process and the design. The other kind of EO crystals, like $LiTaO_3$ and $LiNbO_3$, are also widely used since the high EO-coefficient can achieve high sensitivity [17]. By using these crystals, there are no other process is needed. Table 4.2 lists the EO coefficient of different materials. Comparing with the coefficient in the Table 4.2, the values of r_{33} and r_{51} of $LiTaO_3$ and $LiNbO_3$ are one order larger than GaAs's or InP's. In order to improve the EO sensitivity, a $LiTaO_3$ crystal is chosen as the EO sampling crystal in this measurement.

Table 4.2,

Material	Electro-optical coefficients (10^{-12}m/V)
GaAs	r_{41}=1.2
InP	r_{41}=1.32
$LiNbO_3$	r_{13}=8.6, r_{22}=3.4, r_{33}=30.8, r_{51}=28
$LiTaO_3$	r_{13}=7.9, r_{22}=1, r_{33}=35.8, r_{51}=20

The r_{ij} factors are the EO coefficient by the Pockel effects at different orientation of crystal and symmetry [16].

To explain the principle of EO sampling, it is convenient to use the index ellipsoid [16]:

$$(\frac{1}{n^2})_{xx}x^2 + (\frac{1}{n^2})_{yy}y^2 + (\frac{1}{n^2})_{zz}z^2 + 2(\frac{1}{n^2})_{yz}yz + 2(\frac{1}{n^2})_{zx}zx + 2(\frac{1}{n^2})_{xy}xy = 1 \quad (3)$$

Where x, y, z represent the [100],[010] and [001] directions. The $(\frac{1}{n^2})_{ij}$ are the values of impermeability tensor. The index ellipsoid tells the constant energy surface described by the displacement values D $(= \varepsilon \cdot E)$ and also the refractive index at different polarization. In the EO material, the tensor $(\frac{1}{n^2})_{ij}$ changes linearly by the electric fields. This is the Pockel effect. That is, the variation by

the applied electrical field can be expressed by $\Delta(\frac{1}{n^2})_{ij} = r_{ij} E_k \quad (i, j, k = 1,2,3)$. There are three dimensions for expressing the electric fields and 6 dimensions (9 values can be reduced to 6 due to symmetry) for the index ellipsoid. Therefore, the tensor can be expressed by 6×3 matrix. In $LiTaO_3$ the 6×3 tensor is:

$$(\Delta \frac{1}{n^2})_{ij} = \begin{bmatrix} 0 & -r_{22} & r_{13} \\ 0 & r_{22} & r_{13} \\ 0 & 0 & r_{33} \\ 0 & r_{51} & 0 \\ r_{51} & 0 & 0 \\ -r_{22} & 0 & 0 \end{bmatrix} \cdot \begin{pmatrix} E_x \\ E_y \\ E_z \end{pmatrix} \quad (4)$$

and the index ellipsoid equation:

$$\begin{aligned} &(\frac{1}{n_o^2} - r_{22}E_y + r_{13}E_z)x^2 + (\frac{1}{n_o^2} + r_{22}E_y + r_{13}E_z)y^2 + (\frac{1}{n_e^2} + r_{33}E_z)z^2 \\ &+ 2r_{51}E_y yz + 2r_{51}E_x zx - 2r_{22}E_x xy = 1 \end{aligned} \quad (5)$$

where the values are listed in Table 4.2., n_o is the refractive index at eigenpolarizations x, y axes (principle axises) with the D.C. applied electrical fields and n_e is at z axis.

Figure 4.12 plots the schematic diagrams how the $LiTaO_3$ crystal is placed on the top of output CPW lines for detecting the electrical signal. The photogenerated microwave propagates in the x direction. The optical probe beams propagate towards the $-y$ direction and reflect back for detecting the polarization changes. The plane where the optical probe beam changes the polarization is on the $x-z$ plane, so the value of y can be set as $y=0$. As shown in the Figure 4.12(b) (the cross section of probe light), the probe light pulses pass through the EO crystal and experiences the index changes by the fringe fields near the edge of metal and then reflect back for the detection.

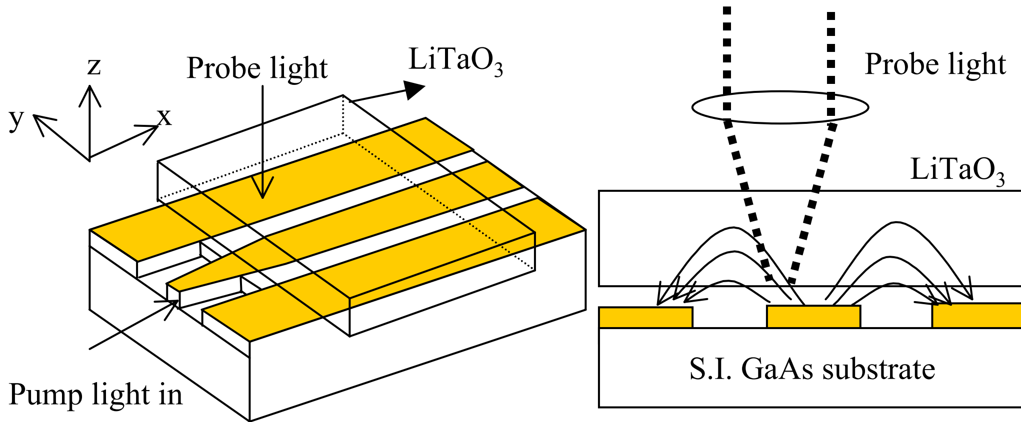

Figure 4.12(a) The $LiTaO_3$ is placed on the top of CPW line with y-cut, x-direction propagation.
(b) Use the fringe field on the edge of metal to detect the EO-sampling signal.

Therefore, the index ellipsoid can be simplified as:

$$(\frac{1}{n_o{}^2} - r_{22}E_y + r_{13}E_z)x^2 + (\frac{1}{n_e{}^2} + r_{33}E_z)z^2 + 2r_{51}E_x zx = 1 \qquad (6)$$

Where the principle axes will change to new the ones x', z' due to the factor of $2r_{51}E_z zx$. For simplifying the calculation of new axes, let's check the order of magnitude of index change. In the CPW line, assume the electrode gaps are $5\mu m$ with $10V$ applied voltage. Also, assume that the maximum of EO-effect achieves, said $r = 35\times 10^{-12}\, m/V$. The value of index ellipsoid change is about $\Delta\frac{1}{n^2} = r\cdot E = 7\times 10^{-5}$, which is much smaller than 1. Hence, the new axes can be approximately expressed by a small angle θ [18], which is in the order of 10^{-3} (radius):

$$\theta = \frac{r_{51}E_x n_o^2 n_e^2}{n_e^2 - n_o^2} \approx 10^{-3} \qquad (7)$$

Figure 4.13 plots the schematic diagram of how the principle axes rotate due to the EO-effects.

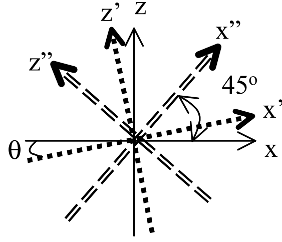

Figure 4.13. Principle axes change due to EO-effect.
X,Z : No electric fields.
X',Z' : with applied field.
X'',Z'' : the polarization beam splitter

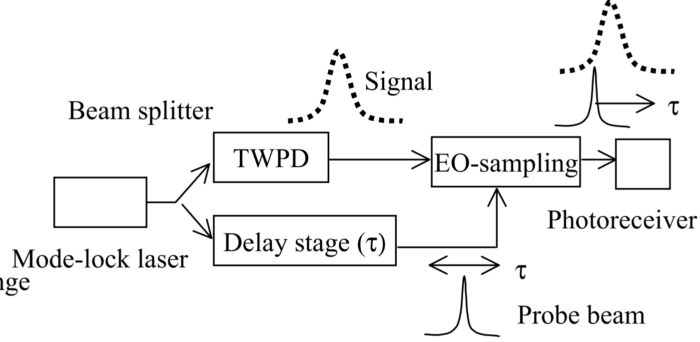

Figure4.14. The schematic diagram of EO-sampling

With the EO effects, the optical refractive indexes of the principle axes will change. After the optical pulse passes through the crystal, the two eigenpolarizations will experience the phase change (retardation effects). They are noted by $\delta n_x, \delta n_z$, and the retardation effect Γ:

$$\delta n_x \approx -\frac{1}{2} n_o^3 (-r_{22} E_y + r_{13} E_z)$$

$$\delta n_z \approx -\frac{1}{2} n_e^3 (r_{33} E_z)$$

$$\delta \Gamma = \frac{2\pi}{\lambda} \int (\delta n_x - \delta n_z) \cdot dy \quad \text{on the EO crystal} \tag{8}$$

Generally, two ways to modulate the optical light by the EO effects are (a) rotating the eigen-polarization (by equation (7)) and (b) retarding the phase change between axes of x and z (by equation (8)). (a) From the Equation 7, the negligible amount in the rotation of the eigen-polarization means that modulating the light is not efficient by this way. (b) In the CPW lines, the E_x fields of microwave and the static applied field are almost zero. E_x exists only when the crystal is misalign or

the non-TEM microwaves propagation. However, the EO effect (r_{33} equation (8)) on the phase change is the maximum value in crystal EO effects. By reference [18], the high efficient optical phase modulation effects (retardation) on the r_{33} can be picked up by selecting the optical polarization shifting 45° from the principle axes (the x"-y" on the Figure 4.13). The amplitude modulation transferred by the optical phase can thus be converted to photocurrent, i.e.

$$I_{photon} = I_o \cdot \delta\Gamma \qquad (9)$$

The microwave signal is linearly related to the retardation and the detection current as well.

Figure 4.14 plots the schematic diagram of pump-probe electro-optic sampling flow chart and setup [19]. The electro-optic sampling technique is based on the optical pulses from the mode–locked laser. As show in Figure 4.14, the optical pulses are divided into two pulses, where one is for pumping the photodetector and the other is for detecting the photogenerated electrical pulse. The pumping pulses couple into the photodetector and generate the electrical impulse response. The electrical pulses pass through the EO-crystal and can consequently be converted to the different phase change of the optical probe beams on time, which is linearly proportion to the electrical pulse amplitude. Once the probe beam is shifted by the time of τ, it will experience the phase change at time τ and be converted to current on the output photoreceiver (Equation (9)). Since all the energy conversion between optical and electric is linear relation, the photoreceiver can duplicate photodetector response if the optical pulse is much shorter than the electrical pulse, the photodector response can hence be measured.

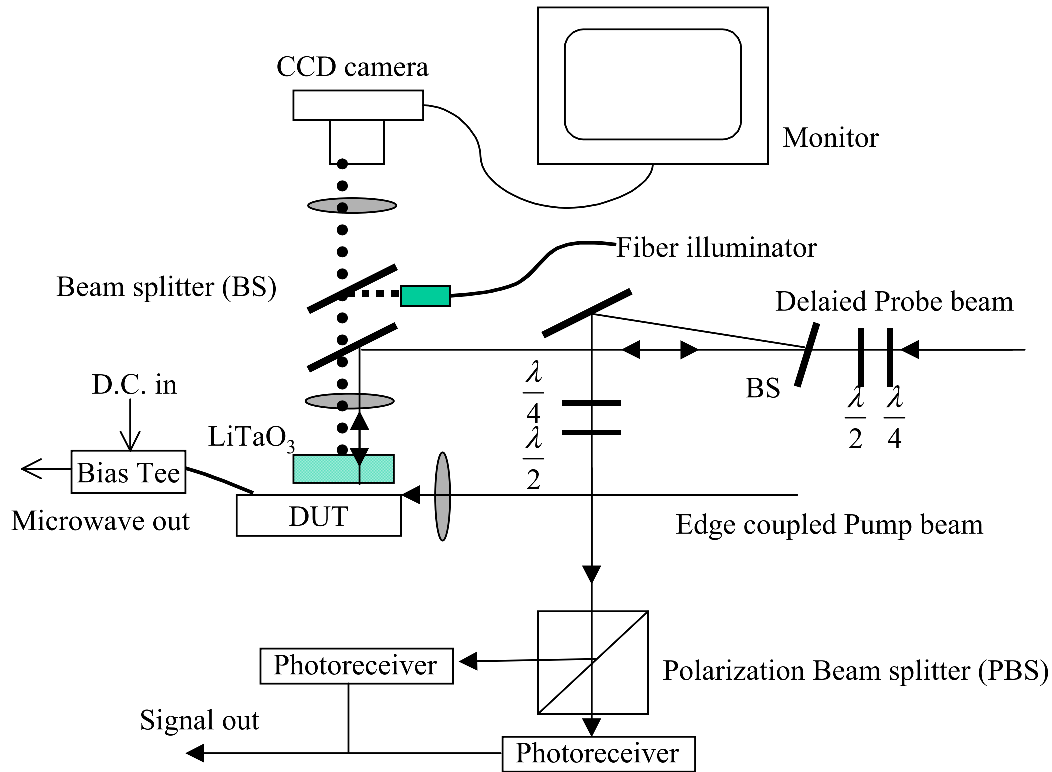

Figure 4.15. The EO-sampling setup (coutesy of Dr. Siegfried B. Fleischer).
The PBS is orientated at 45°from the principle axes of $LiTaO_3$.
Fiber illuminator is for CCD and monitor .

Figure 4.15 shows the schematic electro-optical setup [19]. The pump and probe beams come from the Ti-sapphire mode-locked laser. After the mechanic delay, the probe beam is chopped by an acoustic-optical (AO) modulator at 10MHz which is for eliminating the 1/f noise at low frequencies. The half and quarter waveplates are used for choosing the optical polarization so that the circular polarization is generated and can probe the modulation phase changes by the microwave signal. The output polarization beam splitter (PBS) is selected such that the principal axes are 45^0 angles to the $LiTaO_3$ ones for obtaining the amount of phase retardation [18]. The output detection is the difference of two balanced photoreceivers. The CCD camera and monitor are for pump and probe pulses

alignment. A 50 GHz sampling scope is used to optimize the pump beam alignment.

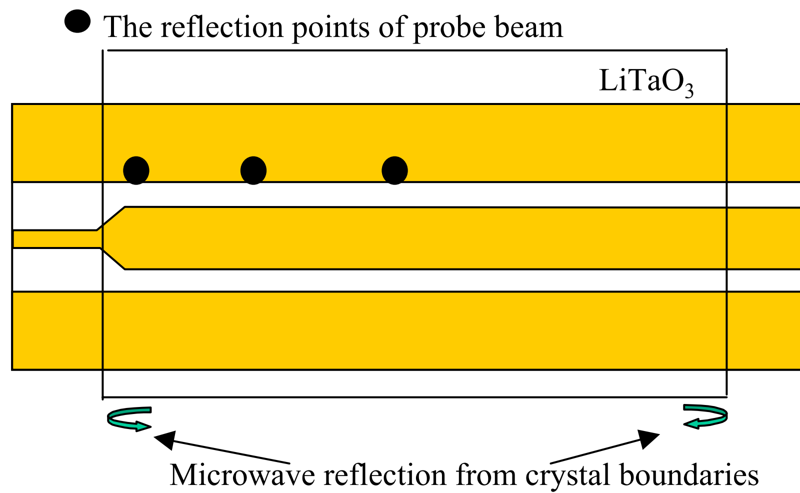

Figure 4.16. The top view of the focus points of probe beam

4.2.3 Electro-optic sampling results:

The TWPD structure under test is measured by EO-sampling. The device is 1 μm wide, 10 μm long and has a 170 nm thick intrinsic region. The optical excitation pulses for the EO-sampling measurement are from a mode-locked Ti-sapphire laser operating at 800 nm with an about 100 fs optical pulse width and a 100 MHz repetition rate. An optical pulse energy of 0.3 pJ (not accounting for the coupling and reflection loss) is used for the optical excitation. The laser is edge coupled into the optical waveguide. After absorption of the optical pulse, the electrical pulse is generated in the TWPD and the microwave impulses are collected and propagate along the output CPW lines. On the CPW lines, the EO sampling pump-probe signal is detected by the $LiTaO_3$ crystal with 100 μm thick, y-cut orientation and x-direction microwave propagation (the principle is described in the Section 4.2.2). The EO-crystal is placed upon the CPW line as shown in the

Figure 4.16. The CPW line is made as $800\mu m$ long such that the echoes from the output contacts of microwave probes can not effect the detection signal (the echoes are shown in the electrical sampling measurement, Figure 4.10). As shown in the Figures 4.12 and 4.16, the optical probe beams are focused near the edge of CPW electrodes, on which the highest electric field density can yield the high EO-sampling signal. The different lengths of $LiTaO_3$ testing on the x-direction are from $500\mu m$ to $800\mu m$. The crystal is long enough that the optical probe beams can focus on the different points of CPW lines region. Therefore, the microwave propagation along the CPW lines can be traced by changing the probe beam positions.

To avoid the nonlinear effects on the device, such as carrier blocking, charge screen effects [20-23], the optical power is kept low such that the impulse response will not change as optical power varies, i.e., the device is operated at linear regime. Also, to eliminate the carrier avalanche effects [24], the TWPD is operated at 3 to 4 V, which are far from the breakdown voltage (about 11V).

Two generations of TWPD are fabricated with the same processing. The second one is to improve the misalignment between the p- and n-contacts that happened during the first generation [14]. Figure 4.17(a) plots the EO sampling signal results and Figure 4.17(b) shows the corresponding frequency response, which is the Fourier transform from (a). The FWHM is around 1.1 ps and the –3dB bandwidth microwave power drop is around 370 GHz. The speed significantly overcomes the device performance limited by carrier transit time [25].

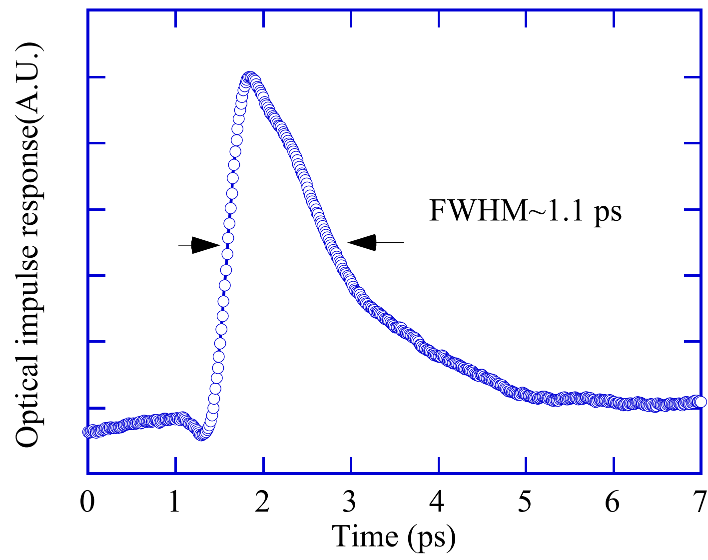

Figure 4.17a. The time response of the first generation TWPD

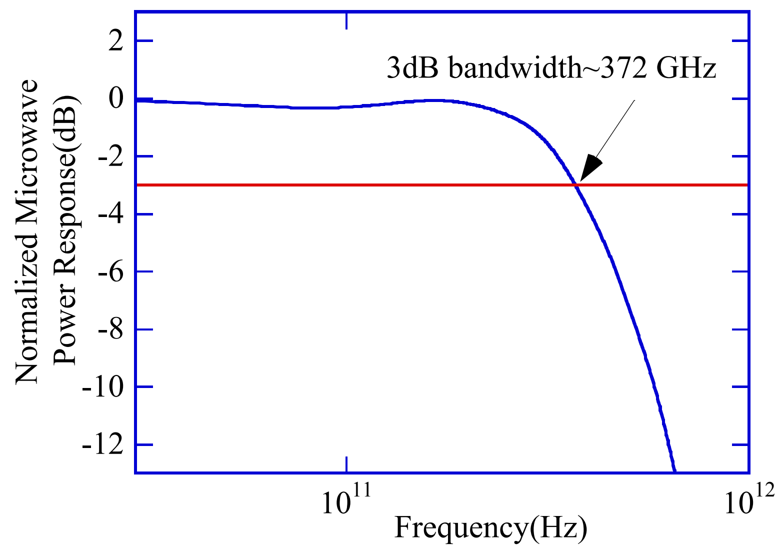

Figure 4.17(b). The power response with frequency. It is obtained from the Fourier transform of figure 4.17(a)

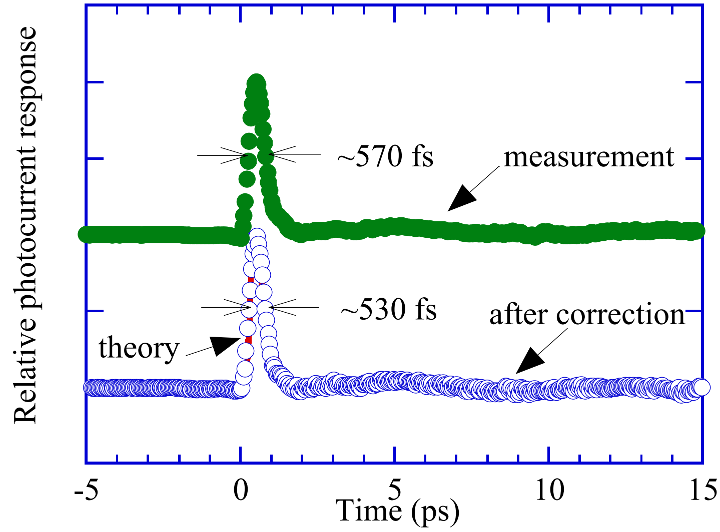

Figure 4.18a. The EO-measurement pulse (top). And the pulse (bottom) after correction the 150fs pulsewidth of optical pulses. The solid curve is the calculation results.

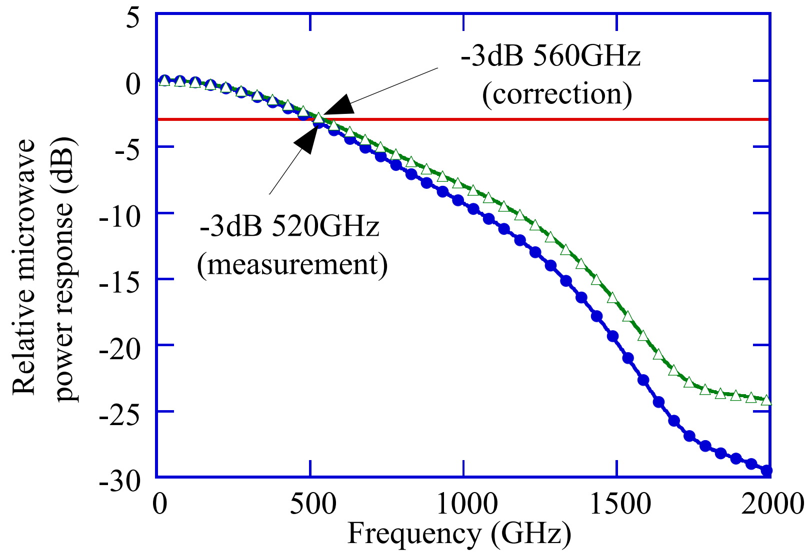

Figure 4.18b. The frequency response of second generation device. The optical pulse is around 150fs FWHM (autocorrelation)

In Figure 4.17(a), the signal has about 2 to 4 ps of decay time before and after the peak value, which is not consistent with the corresponding carrier lifetime (~300fs). The processing, the intrinsic material itself and the electro-optic measurement may influence the device performance. During the processing, a considerable misalignment between the n- and p- contact metalization is found in every device in the first generation. To examine the accuracy of EO-sampling measurement, the second generation is fabricated for the comparison with the first one. In the second generation, the same wafer and process techniques are used. The photolithography for the n- and p- regions is improved. As shown in the Figure 4.18(a), the electro-optical impulse response exhibits a 570fs FWHM (top curve). After correction by optical pulse width (150fs autocorrelation pulsewidth), the pulse has a 530 fs FWHM. Their corresponding Fourier transform bandwidths shows 520GHz (measurement) and 560GHz –3dB bandwidth (correction). In contrast to the results from the first generation, the signal is clearer and also the device performance is improved by around 50%. Thus, the slower response in Figure 4.17(a) is mainly caused by the parasitic capacitance, which results from the misalignment between n- and p- contacts.

In the regime of the subpicosecond response, the high dispersive effects of transmission lines may be the considerable effects on the time signature of device response and the accuracy of the EO sampling technique. The electrode gap in the CPW line is about $5\mu m$. In the typical transmission line, the dispersion effects due to the substrate and EO sampling crystal can be defined on a critical frequency [26].

$$f_c = c_0 / 4s\sqrt{\varepsilon_{rel} - 1} \qquad (10)$$

where ε_{rel} is the relative dielectric constant, s is the gap between electrode and c_0 is the light velocity in vacuum. Above this critical frequency, modal dispersive effects due to higher order modes become significant. So, the time signature will

change as transmitting along the CPW line. However, below that, the modal dielectric constant can be treated as frequency independent. The material surrounding the CPW metalization is GaAs (ε_{rel} = 13.2 in the microwave region), and $LiTaO_3$ (ε_{rel} = 43 in the microwave region), in that their corresponding modal critical frequency are around 5 and 2.5 THz respectively. The measured signals we obtained are, however, slower than these. Moreover, to further minimize this kind of microwave dispersion effects (pulse broadening and chirping), the measured response is obtain as close as the photodetector output.

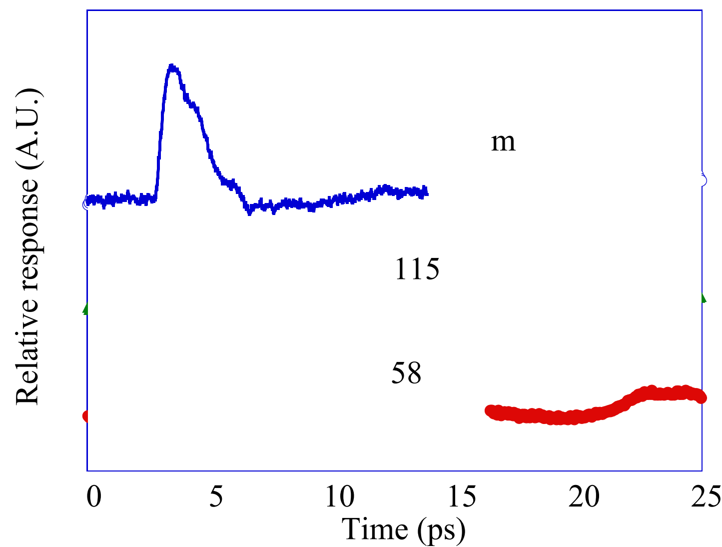

Figure 4.19. The pulse evolution at different position from the photodetector on CPW lines.

The other factor that might influence the EO-sampling measurement is the microwave reflection on the zone boundaries of $LiTaO_3$, as shown in the Figure 4.16. Due to the high dielectric constant (ε_{rel}=43) of $LiTaO_3$, the modal microwave index and impedance will change. The reflections from the crystal boundaries will interfere with the signal. From the EO-sampling data, however, there is no evidence showing these effects. For example, Figure 4.19 plots the

measured EO-sampling data at different positions on the CPW lines. The positions are measured from the photodetector facet to the probe beam spots. The $LiTaO_3$ is around 550μm long. As shown, the EO-sampling signature at 58μm has another small peak at around 22.5 ps from the main pulse. This echo is consistent with the echo time delay (~25 ps) on the electrical sampling measurement (in Figure 4.11). This means that electrical pulses experience the same propagation speeds in either the CPW line with $LiTaO_3$ on the top or with air (the electrical sampling measurement). Additional test is shown in Figure 4.20, which shows the measured EO sampling positions along the CPW line and the pulse delay time. From the slope of Figure 4.20, the propagation index of electrical pulse can be estimated. On CPW line, the microwave velocity can be approximated

$\sqrt{\frac{1+\varepsilon_{GaAs}}{2}} \sim 2.5$ for the case with air on the top

$\sqrt{\frac{\varepsilon_{LiTaO_3}+\varepsilon_{GaAs}}{2}} \sim 5.3$ for the case with $LiTaO_3$ on the top (11)

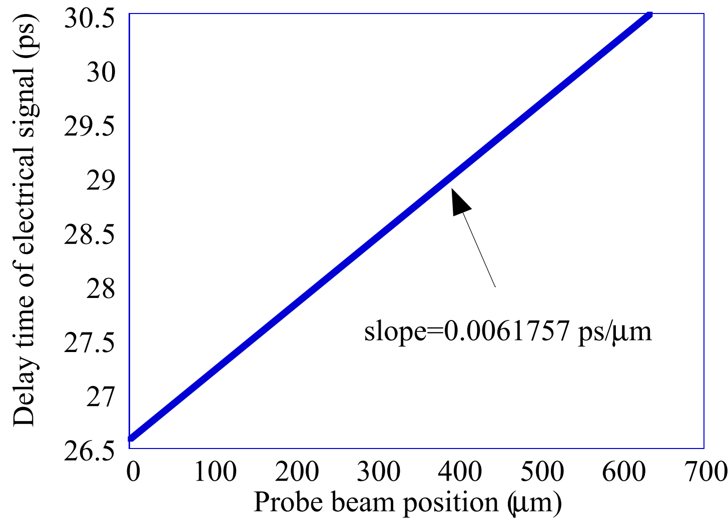

Figure 4.20. The pulse evolution on the CPW lines

The index extracted from Figure 4.20 is about 2.2, which is close to the value of the CPW line without the EO crystal. Even though the $LiTaO_3$ has a much higher dielectric constant than GaAs, the EO crystal is only resting on the GaAs and an air gap of several microns between the crystal and the GaAs is to be expected. Such a gap will decouple the waveguide mode from the crystal because of the small electrode separation of only $5\mu m$ used for the samples. The crystal effects on microwave propagation are minimal.

4.2.3 Discussion of EO-sampling results**:**

In the previous section, the effects of $LiTaO_3$ application on the EO-sampling measurement are presented. The results were used to calculate the device speed up to above several hundred GHz. The speed of the LT-GaAs p-i-n TWPD was tested and the device shows promise as a high-speed photodetector. However, there are remaining questions about the device performance. What is the limitation of LT-GaAs p-i-n TWPDs? Is it coming from the material itself or the circuit? Several factors affect the impulse response of traveling wave photodetectors, namely microwave loss and dispersion in the microwave transmission line, impedance mismatch, reflection in the optical input and the basic material response. In this section, the data measured by the EO-sampling is analyzed to investigate the TWPD circuit. Also, the distributed effects (chapter 2) are used to simulate the measurement in order to thoroughly understand the TWPD properties.

First, the p-i-n transmission line effects should be analyzed. In Chapter 2 , the model distributed photodetectors is adopted to calculate the device speed performance. Equation 2.10 shows the total device performance including the velocity mismatch between optical wave and microwave signal, the reflection, the microwave loss and the material properties. To isolate the microwave propagation effect, the distributed effects and optical absorption should be eliminated. This can be done by comparing two different lengths of TWPDs. Here, $10\mu m$ and $25\mu m$ long devices are fabricated on the processing and measured. The same D.C.

external quantum efficiencies are measured for these two devices, indicating that the absorption length is below $10\mu m$. Therefore, comparing the two frequency responses, the propagation constant can be solved using the expression:

$$\frac{V_1(f)}{V_2(f)} = \exp(-\bar{\gamma}\cdot(l_1 - l_2)) = \exp(-(\alpha(f) + j\beta(f))\cdot(l_1 - l_2)) \qquad (12)$$

where V_1, V_2 are the frequency response of device 1 and 2, l_1 and l_2 are the lengths.

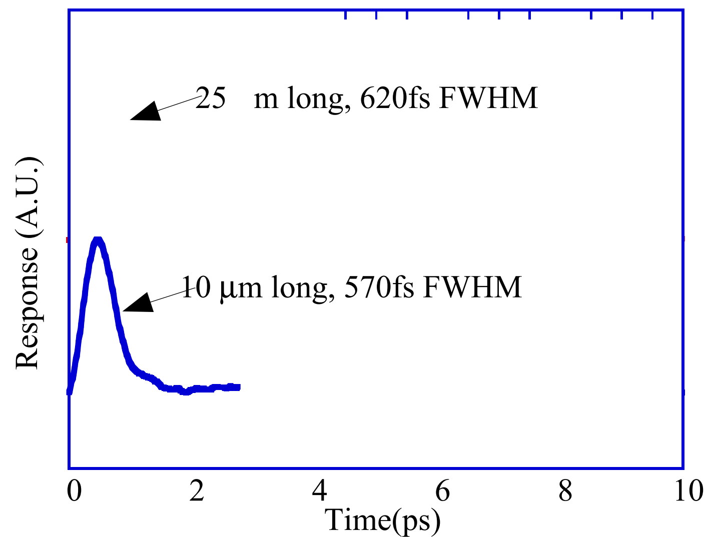

Figure 4.21. Comparision of different lengths of devices

Figure 4.21 plots the EO-sampling results of both devices with the pulsewidths of 620fs (top curve, $25\mu m$ long) and 570fs (bottom curve, $10\mu m$ long) respectively. Both performances show a very similar and fast rise time, but the rear parts of pulses show quite different falling times. A longer decay tail is found on the $25\mu m$ long device. The main reasons for the difference are the microwave field attenuation and the dispersion, since the only difference between two devices is the waveguide length. By applying Equation 4.12, the microwave loss and dispersion curves as a function of frequency can be calculated. They are shown in Figure 4.22.

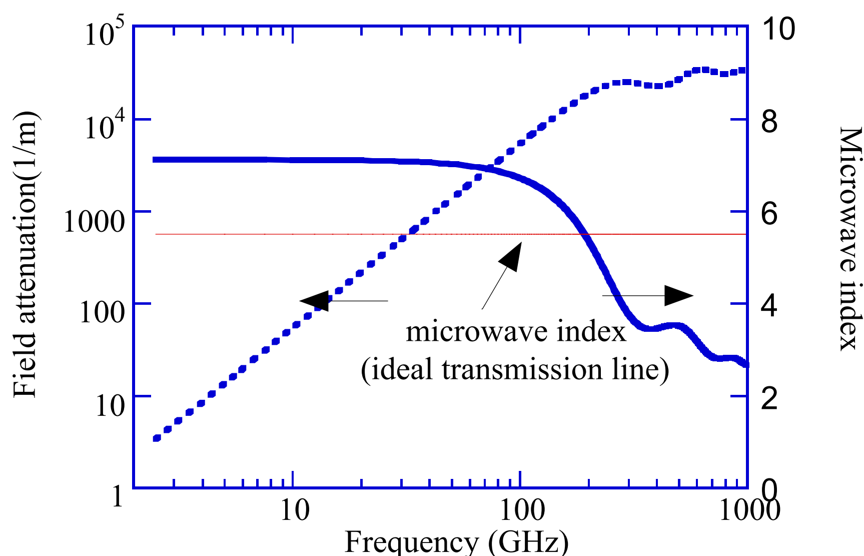

Figure4.22. The microwave loss and index vs frequency. The values are calculated from the measured EO-sampling data of two different lengths of photodetectors

The optical group index is around 3.5. The velocity mismatch (walk-off) factor ($l/v_e - l/v_o = l/c_o \cdot (n_e - n_o)$) is below 0.4 ps for the longer device at the frequencies above 5GHz. Considering that the tail is approximately 3 ps long, we see that the velocity mismatch is not the main reason for the slower speed of the $25\mu m$ device.

As shown in Figure 4.22, the attenuation of the microwave signal is around $0.02\mu m^{-1}$ for the regime from 100 GHz to 1 THz. The corresponding microwave loss should be about –1.7dB and –4.3dB for $10\mu m$, $25\mu m$ lengths respectively. Allowing a –3dB bandwidth penalty, the only way to exceed terahertz bandwidth is to make the device length shorter than $20\mu m$. The bandwidths from these two measured impulses are found to be around 520GHz and 340GHz. The microwave attenuation is thus one of the main limiting factor.

The impedance mismatch may be the problem. The waveguide is about 30 ohm at frequencies above several GHz. The output CPW line is designed as 35Ω

to 45Ω. The output reflection will be from 10% to 20%. As shown in Figure 4.22, the microwave index ranges from 3 to 7. Because the optical input end is equivalent to an open circuit, and taking into account the reflection from the output CPW line, we find that the corresponding round trip time is ranged from 0.1 to 0.4 ps with an amplitude smaller than 20% of the main pulse. This means that the output received pulses from the two internal reflections in the waveguides are shorter than 1ps within 4 % of the main pulse strength. Taking into account the loss effects, the amplitude is even less. In this case, the multiple reflections due to impedance mismatch can be neglected.

To realize the material response, the calculated bandwidth dependence as a function of the velocity mismatch ration (v_m / v_o, microwave velocity to optical velocity) is plotted in the Figure 4.23. The waveguide is assumed to be 1 μm wide, 10 μm and have a 170nm thick intrinsic region, which are the best conditions on the design (Chapter 3) and the measured EO-sampling results. The top curve of Figure 4.23 shows that an ideal TWPD (no loss, no dispersion, no reflection at the photodetector boundary and carrier lifetime is assumed to be zero) gives optimal performance when the velocity matched ($v_m / v_o = 1$). However, while considering the carrier lifetime effects, the response is almost flat over a large range of velocity mismatch ($v_m / v_o = 0.5 \sim 1$). And the –3dB bandwidth is only dependent on the carrier lifetime over the range of 100fs to 400fs, which is the range of the carrier lifetimes obtained from the same growth conditions of LT-GaAs. The loss, dispersion and reflection (dashed curves) also have only minor effects on this 10 μm long device. The experimental result (the "*" point) is quite consistent with the theory and the discussion in this section.

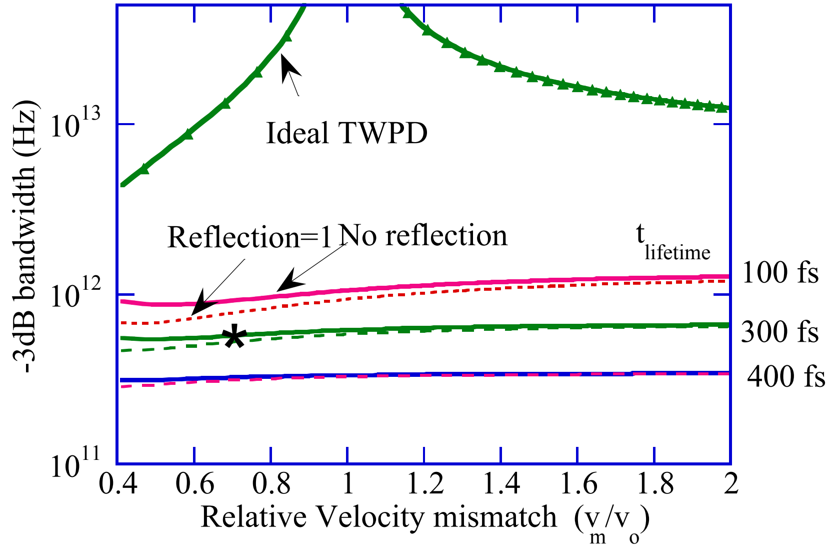

Figure 4.23. The -3dB bandwidth with the relative microwwave velocity for different carrier lifetime. The device length is about 1μm. The "*" point is the experiment point.

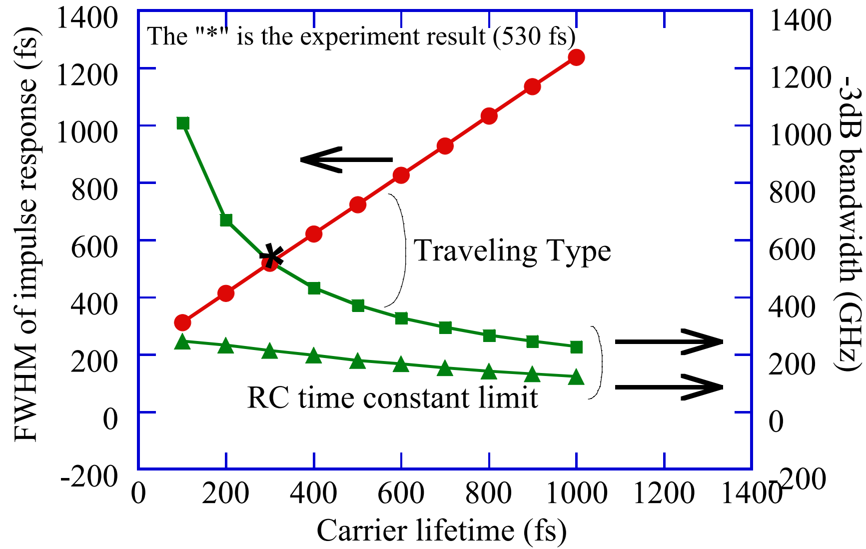

Figure4.24. The calculated impulse response v.s. the effective carrier lifetime for the 1μm long device. The top two curves are TWPD, and the bottom is the RC-imposed bandwidth.

To examine the RC-time constant effects, Figure 4.24 summarizes the calculated impulse response as a function of the effective carrier lifetime. The RC-imposed bandwidth is shown on the bottom of Figure 4.24 (triangle), for a vertically illuminated structure with the same active area and the intrinsic region thickness. The measured result is marked with a "*" point in Figure 4.24. Compared to a RC-limited lump element photodetector, the significant improvement in the bandwidth of the TWPD indicates that this RC-limitation is overcome in TWPD. Instead, the limitation is from the carrier lifetime.

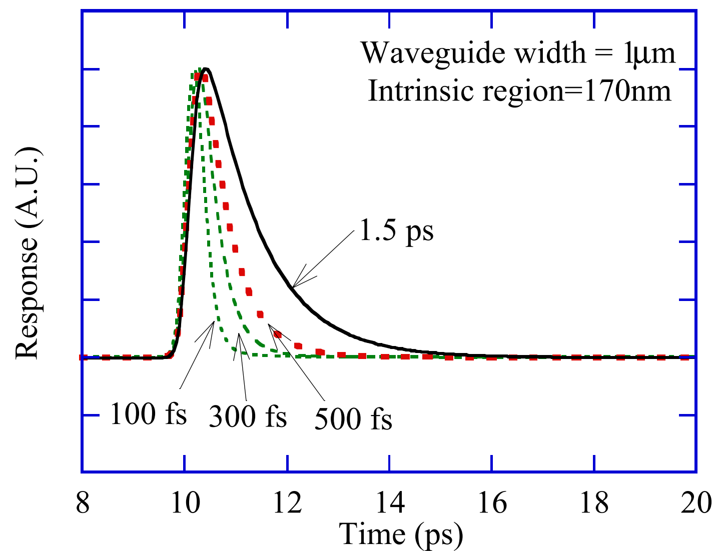

Figure 4.25. The calculated impulse response at different effective carrier lifetime

Figure 4.25 plots the calculated impulse responses at different effective carrier lifetimes. It can been seen is that the shorter carrier lifetime obtain narrower pulsewidth. The carrier lifetime is around 250fs to 300fs in the LT-GaAs material, using these values the calculated pulse width is around 550 fs, which is in good agreement with the measured results. The carrier transit time across the intrinsic region (170nm) is around 1.5 ps (the saturation velocity is assumed $10^7 cm/s$)[27]. Defining this carrier sweep time, the calculated TWPD response is shown as a solid

line in Figure 4.25. A 1.5 ps FWHM (about 200 GHz bandwidth) is obtained, which is quite consistent with the experimental results from Giboney's GaAs-TWPD [15]. In contrast to the carrier lifetime limit TWPD, the TWPD shows only a small improvement over the RC-limitation (Figure 2.24). However, by utilizing LT-GaAs with a traveling wave structure, this photodetector is shown to have an advantage over the RC-limited device.

4.3 The bias dependence response:

Figure 4.26 shows the bias dependent response. The breakdown voltage of the photodiode is around 10 V. The reverse bias applied is 1v to 7v to prevent the carrier multiplication in the high field region. As shown in the Figure 4.26, the pulsewidths and the tails do not change significantly from low bias to high bias voltage. It is found that the FWHM of between 520 and 540 fs is almost constant within the accuracy of measurement. This behavior is not like that of carrier transit-time photodetectors [25,28].

In general carrier transit limited photodiodes, broadened pulses and slow tails will be observed at lower bias, which is attributed to the carrier blocking in the heterojunction [28,30]. With increasing bias, the tail becomes smaller due to the increase in the hole velocities. At higher bias (below breakdown), the pulses will also broaden due to the increase in depletion region width. However, in this experiment, there is almost no difference found in the bias dependent measurements. The difference from the carrier transit limited photodetectors is that the LT-GaAs is used for carrier trapping limitation. The photogenerated charges recombine in the defect center of the LT-GaAs. The charges will be trapped before they are swept out of the intrinsic region at the drift velocities. So, the heterojunction trapping effects at lower bias and the longer transit time due to the longer intrinsic region at high bias will be small. This is one evidence that the speed mechanism of the LT-GaAs TWPD is dominated by the high carrier recombination rate.

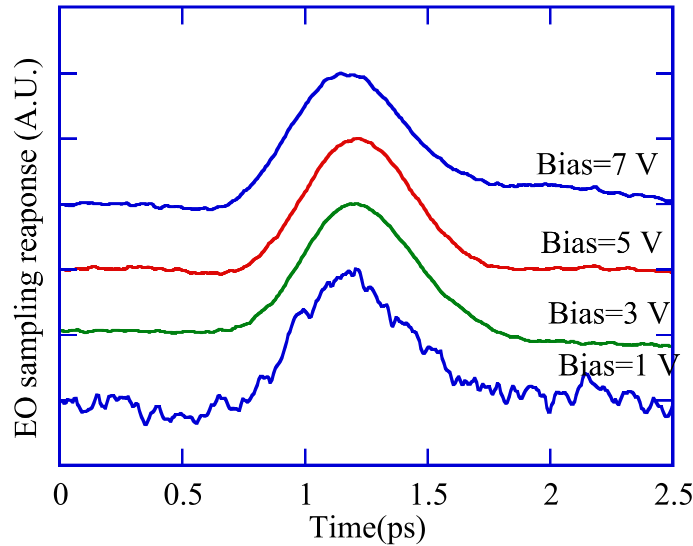

Figure 4.26. The bias dependent EO-sampling response

4.4 The power dependence response:

Figure 2.27 shows the power dependence of the measured detector response. In the linear or low excitation regimes, the corresponding photogenerated charge is around $10\,fc$ (1.0W optical peak power), the photocurrent shows a subpicosecond response due to the fast photocarrier trapping in the LT-GaAs. As the optical power is then increased gradually, the signal shows an initial fast response similar to the low excitation regime. A slower pulse with a few picoseconds duration then follows the fast pulse. This behavior is quite similar to the performance of TWPD with GaAs active region [15]. Under the high power excitation, the space charge effects will build up and collapse the electric field applied by the external bias [20-23,30].

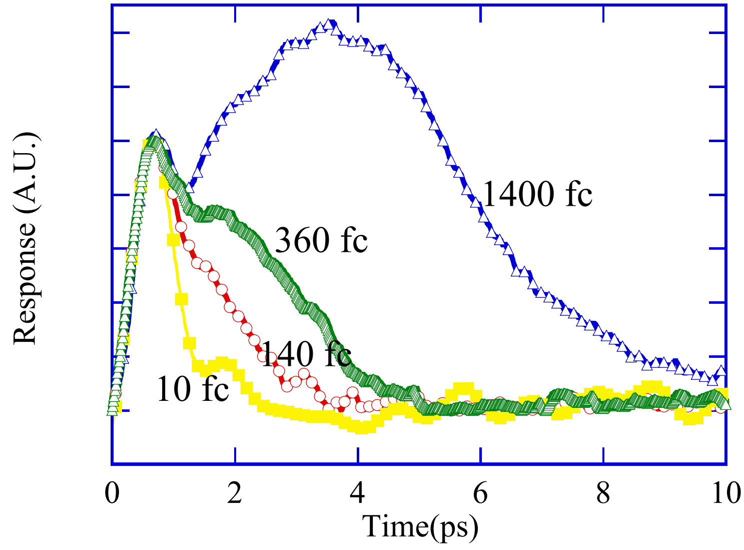

Figure 2.27. The measured EO-sampling at different excitation intensity

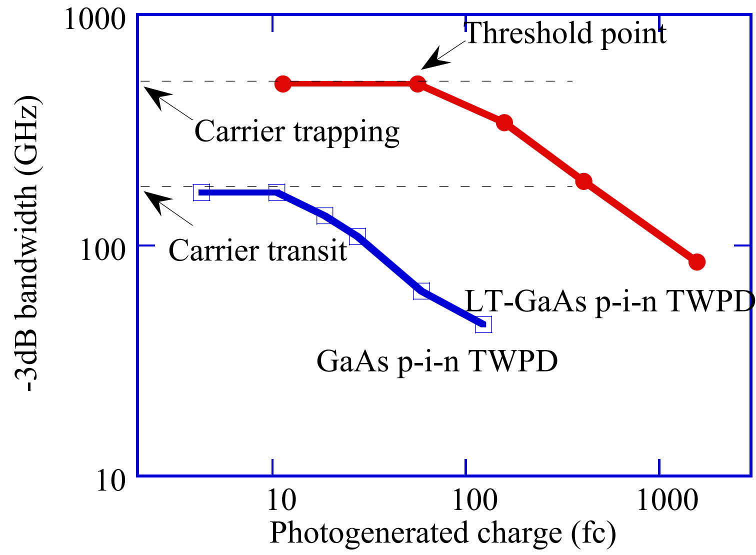

Figure 4.28. The bandwidth with different photogenerated charge

Figure 4.28 plots the corresponding –3dB bandwidth with the optical excitation charge of the impulse response shown in Figure 4.27. The bottom curve is the data from Giboney's [15], which is measured from the GaAs-TWPD. The low excitation exhibits two different speeds attributed to two mechanisms, carrier trapping time and transit time limitation. Another discrepancy is the threshold points (LT-GaAs and GaAs have the values around $10\,fc$ and $60\,fc$ respectively) for the nonlinear saturation effects. Generally, the LT-GaAs photodetectors inherently have low quantum efficiency due to high carrier recombination rate (Equation 3.1). However, in Figure 4.28, the LT-GaAs TWPD exhibits a saturation power about six-time higher than that of the GaAs-TWPD. The operation of the LT-GaAs TWPD can be implemented with a higher pumping power to compensate for the low quantum efficient and still have a higher bandwidth than the GaAs-TWPD.

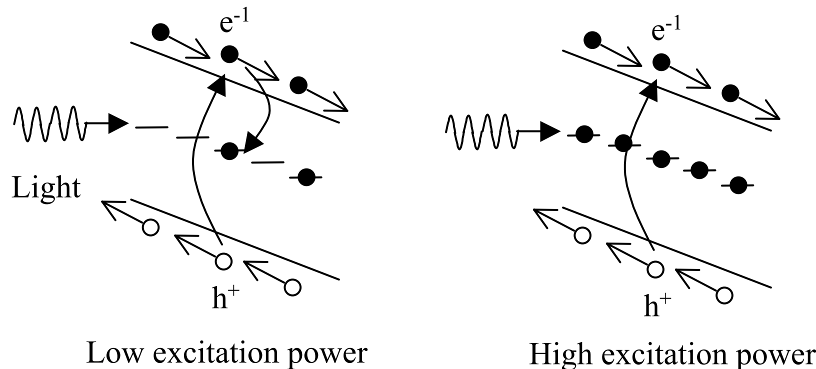

Figure 2.29, the schematic diagram for trapping saturation effects

At low power, the GaAs detectors showed a bandwidth of 170GHz [15]. The bandwidth for LT-GaAs drops below 170GHz for a photoexcited charge of $\sim 500\,fc$. Both GaAs and LT-GaAs devices have the same thickness in the intrinsic region. This indicates that for an excitation level above $\sim 500\,fc$ the traps are filled and the detector becomes carrier transit limited. As the power excitation increases, the high recombination effects turns to be charge screening dominated and then

transit-time limited. The schematic diagram, Figure 2.29, explains this. The defects are saturated as the optical power density increases due to the limited defect density in the LT-GaAs material. A few experiments by the pump-probe measurement on LT-GaAs also observed the similar behaviors [31-33]. From the threshold point in the curve of figure 2.28, the corresponding trap density is around $8\times10^{17} cm^{-3}$, which is consistent with the value given in [30].

With the power dependent EO-sampling measurement, the high-speed performance of LT-GaAs TWPD is understood to be limited by carrier trapping effects at low excitation density. At high density pumping, the carrier transit effect dominates due to the trap density filling.

4.5 Summary:

In this section, the high-speed responses of traveling wave photodetectors are presented. The D.C. and A.C. performance of LT-GaAs p-i-n waveguide is first characterized to evaluate the traveling wave circuits. Then, the impulse responses of the TWPD were measured by the electro-optic sampling technique. To gain more insights into the TWPD structure, a distributed photodetector model was used to simulate the detector response and obtain a good agreement with the experimental results. From the bias dependence and power dependence, and the calculated distributed effect analysis, it is found that this kind of photodectors is limited by the carrier trapping time in the LT-GaAs.

Reference:

[1]Schneider, H.; Larkins,E.C.; Ralston, J.D.; Fleissner, J.; Bender, G.; koidl, P.,' Diffusive electrical conduction in high-speed p-i-n photodetectors', Applied Physics Lett., vol60 (no.21), p2648-50, 1992

[2]Murakami, M.; Oku, T.; Koide, Y.; Wakimoto, H.; Furumai, M.; Kobayashi, S. 'Ohmic contact materials for compound semiconductors.' Proceedings of the Twenty-First State-of-the-Art Program on Compound Semiconductors (SOTAPOCS XXI), Electrochem. Soc, 1995. p.163-74. vii+304.

[3]Goossen, K.W.; Cunningham, J.E.; Zhang, G.; Walker, J.A. 'Very large arrays of flip-chip bonded 1.55 μm photodetectors'. Journal of Lightwave Technology, vol.16, (no.6), IEEE, June 1998. TA1800 .J68, p.1056-61.
[4] Ralph E. Williams, 'Gallium Arsenide processing techniques'.
[5] Chand, N.; Henderson, T.; Klem, J.; Masselink, W.T.; Fischer, R.; Chang, Y.-C.; Morkoc, H. 'Comprehensive analysis of Si-doped Al/sub x/Ga/sub 1-x/As (x=0 to 1): theory and experiments'. Physical Review B (Condensed Matter), vol.30, (no.8), 15 Oct. 1984. p.4481-92.
[6] Shen, T.C.; Gao, G.B.; Morkoc, H., 'Recent developments in ohmic contacts for III-V compound semiconductors'. Journal of Vacuum Science & Technology B (Microelectronics Processing and Phenomena), vol.10, (no.5), Sept.-Oct. 1992. p.2113-32 T1 .J754
[7] Kucera, J.J.; Gutmann, R.J. 'Effect of finite metallization and inhomogeneous dopings on slow-wave-mode propagation'. IEEE Transactions on Microwave Theory and Techniques, vol.45, (no.10, pt.1), IEEE, Oct. 1997. p.1807-10. T1, I27 M53
[8]George D. Vendelin, Anthony M. Pavio, and Ulrich L. Rohde, ' Microwave Circuit Design using linear and nonlinear techniques'. Wiley Publication, 1990
[9]Peter A. Rizzi, 'Microwave engineering passive circuit'. Prentice hall 1988
[10]Giboney, K.S.; Rodwell, J.W.; Bowers, J.E. 'Traveling-wave photodetector theory'. IEEE Transactions on Microwave Theory and Techniques, vol.45, (no.8, pt.2), IEEE, Aug. 1997. p.1310-19.
[11]Bottcher, E.H.; Bimberg, D. 'Millimeter wave distributed metal-semiconductor-metal photodetectors'. Applied Physics Letters, vol.66, (no.26), 26 June 1995. p.3648-50.
[12] Pribetich, P.; Seguinot, C.; Kennis, P. 'Systematic determination of the propagation characteristics of coplanar lines on semiconductor substrate'. IEEE Transactions on Microwave Theory and Techniques, vol.39, (no.7), July 1991. p.1083-9.
[13] Daniel Tauber, ' Design and performance of semiconductor microstrip lasers', UCSB Ph.D. Dissertation March 1998
[14] Yi-Jen Chiu; Fleischer, S.B.; Lasaosa, D.; Bowers, J.E. 'Ultrafast (370 GHz bandwidth) p-i-n traveling wave photodetector using low-temperature-grown GaAs'. Applied Physics Letters, vol.71, (no.17), AIP, 27 Oct. 1997. p.2508-10.
[15] Giboney, K.S.; Rodwell, M.J.W.; Bowers, J.E. 'Traveling-wave photodetector design and measurements'. IEEE Journal of Selected Topics in Quantum Electronics, vol.2, (no.3), IEEE, Sept. 1996. p.622-9.
[16] Amnon Yariv and Pochi Yeh, 'Optical waves in crystals'.
[17] Heutmaker, M.S.; Cook, T.B.; Bosacchi, B.; Wiesenfeld, J.M.; Tucker, R.S. 'Electrooptic sampling of a packaged high-speed GaAs integrated circuit'. IEEE Journal of Quantum Electronics, vol.24, (no.2), Feb. 1988. p.226-33.

[18] Itatani, T.; Nakagawa, T.; Kano, F.; Ohta, K.; Sugiyama, Y. 'Electrooptic vector sampling-measurement of vector components of electric field by the polarization control of probe light'. IEICE Transactions on Electronics, vol.E78-C, (no.1), Jan. 1995. p.73-80

[19] Thanks to Dr. Siegfried B. Fleischer for setuping the EO-sampling system.

[20] Williams, K.J.; Esman, R.D. 'Photodiode DC and microwave nonlinearity at high currents due to carrier recombination nonlinearities'. IEEE Photonics Technology Letters, vol.10, (no.7), IEEE, July 1998. p.1015-17.

[21] Williams, K.J.; Esman, R.D.; Dagenais, M. Nonlinearities in p-i-n microwave photodetectors. Journal of Lightwave Technology, vol.14, (no.1), IEEE, Jan. 1996. p.84-96.

[22] Saar, A.; Mermelstein, C.; Schneider, H.; Schoenbein, C.; Walther, M. 'Space charge buildup in quantum-well infrared photodetectors leading to low-power nonlinear photoresponse'. IEEE Photonics Technology Letters, vol.10, (no.10), IEEE, Oct. 1998.

[23] Uskov, A.V.; Karin, J.R.; Nagarajan, R.; Bowers, J.E. 'Dynamics of carrier heating and sweepout in waveguide saturable absorbers'. IEEE Journal of Selected Topics in Quantum Electronics, vol.1, (no.2), June 1995. p.552-61.

[24] Anselm, K.A.; Nie, H.; Hu, C.; Lenox, C.; Yuan, P.; Kinsey, G.; Campbell, J.C.; Streetman, B.G. 'Performance of thin separate absorption, charge, and multiplication avalanche photodiodes'. IEEE Journal of Quantum Electronics, vol.34, (no.3), IEEE, March 1998. p.482-90.

[25] Giboney, K.S.; Nagarajan, R.L.; Reynolds, T.E.; Allen, S.T.; Mirin, R.P.; Rodwell, M.J.W.; Bowers, J.E. 'Travelling-wave photodetectors with 172-GHz bandwidth and 76-GHz bandwidth-efficiency product '. IEEE Photonics Technology Letters, vol.7, (no.4), April 1995. p.412-14.

[26] Valdmanis, J.A.; Mourou, G. 'Subpicosecond electrooptic sampling: principles and applications'. IEEE Journal of Quantum Electronics, vol.QE-22, (no.1), Jan. 1986. p.69-78.

[27]Sze, 'Physics of semiconductor device'. Second edition

[28]Yih-Guei Wey; Giboney, K.S.; Bowers, J.E.; Rodwell, M.J.W.; Silvestre, P.; Thiagarajan, P.; Robinson, G.Y. '108-GHz GaInAs/InP p-i-n photodiodes with integrated bias tees and matched resistors'. IEEE Photonics Technology Letters, vol.5, (no.11), Nov. 1993. p.1310-12.

[29] I-Hsing Tan; Chi-Kuang Sun; Giboney, K.S.; Bowers, J.E.; Hu, E.L.; Miller, B.I.; Capik, R.J. 120-GHz long-wavelength low-capacitance photodetector with an air-bridged coplanar metal waveguide. IEEE Photonics Technology Letters, vol.7, (no.12), IEEE, Dec. 1995. p.1477-9.

[30]Chi-Kuang Sun; I-Hsing Tan; Bowers, J.E. 'Ultrafast transport dynamics of p-i-n photodetectors under high-power illumination'. IEEE Photonics Technology Letters, vol.10, (no.1), IEEE, Jan. 1998. p.135-7.

[31] Personal communication with Professor Nadir Dagli.

[32] Ralph Spickermann, 'High speed Gallium Arsenide/ Aluminum Gallium Arsenide traveling wave electro-optic modulators'. University of California, Santa Barbara CA. Ph.D. dissertation April 1996.

[33] Alferness, R.C. 'Waveguide electrooptic modulators'. IEEE Transactions on Microwave Theory and Techniques, vol.MTT-30, (no.8), Aug. 1982. p.1121-37.

Chapter 5

Long Wavelength Detection

For optical fiber communications, the wavelengths widely used are in the range of 1.3-1.6 μm. Most commercial optical receivers in this long wavelength range are based on the GaInAsP material. Progress in commercial development of InP-based integrated receivers or electronic circuits is slow. On the other hand, the AlAs/GaAs material is a well-developed material and such photodetectors have been integrated with high performance integrated circuits. However, its higher bandgap (1.42eV, $\lambda < 0.78\mu m$, short wavelength absorption) restricts the application to datacom communication only (short wavelength). The defect states and As metallic formation in the LT-GaAs are found to be around 0.6~0.7 eV below the conduction band edge [1~3]. For these kind of sub-bandgap states, the optical absorption has been observed at 1.3 and 1.55 μm [4,5]. Figure 5.1 draws the schematic plots of how the short wavelength (left) and long wavelength (right) is absorbed in LT-GaAs.

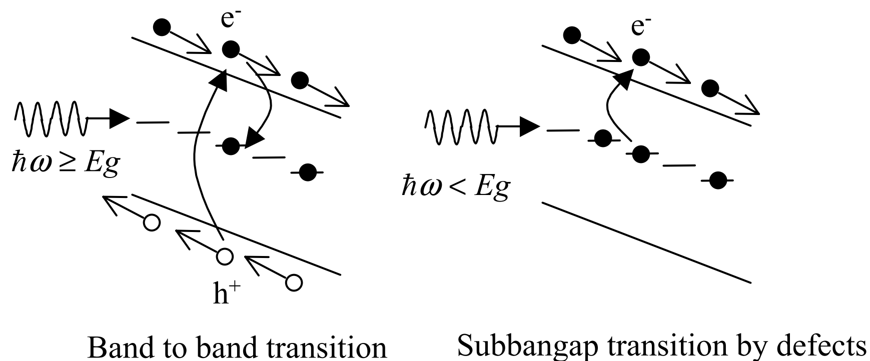

Figure 5.1. The schematic plots of long wavelength (right) and short wavelength (left) light absorption

LT-GaAs has been used to make high-speed photodetectors with bandwidths up to ~0.5 THz at 800 nm wavelength (described in the chapter 4). Also, a subpicosecond carrier trapping time at long wavelength was observed in reference [6]. LT-GaAs material thus has the potential to be used in high-speed photodetectors at long wavelengths. Reference [4,5] have shown that the long wavelength light can be absorbed in the LT-GaAs MSM structure, but a low quantum efficiency ($\approx 0.5 \quad mA/W$) is obtained due to the low absorption coefficient and high carrier recombination rate. In contrast to the top-illumination detectors, the waveguide structures can be designed more flexibly. Before this work, high-speed performance of LT-GaAs photodetectors at long wavelengths had not been investigated. In this chapter, improving the efficiency and maintaining the device speed are the main points described.

The quantum efficiency of photodetectors can be expressed by equation 3.1. which is :

$$\eta = \eta_g \cdot \frac{p_o}{h \cdot \nu} \cdot q \cdot (1 - e^{-\Gamma \cdot \alpha \cdot l}) \cdot \frac{t_l}{t_t} \qquad (5.1)$$

Quantum efficiency in the LT-GaAs is generally low due to the low carrier trapping time (t_l). The absorption coefficient of LT-GaAs at long wavelength is small [7], which is below $0.1 \mu m^{-1}$. Typically, the thickness of the LT-GaAs layer is about 0.1 to 1 μm. That is, less than 10% of optical power is absorbed to generate current in the vertical-illumination type detectors. This is the reason why the quantum efficiency in reference [4,5] is about three orders less than the band-to-band transition photodetectors.

Although the material absorption coefficient α is low in LT-GaAs, a waveguide structure can be used to improve the factor of $\Gamma \alpha \cdot l$ by increasing the device length. Also, the speed of waveguide photodetector can be optimized by the TWPD structure.

5.1. Characteristics for short length device :

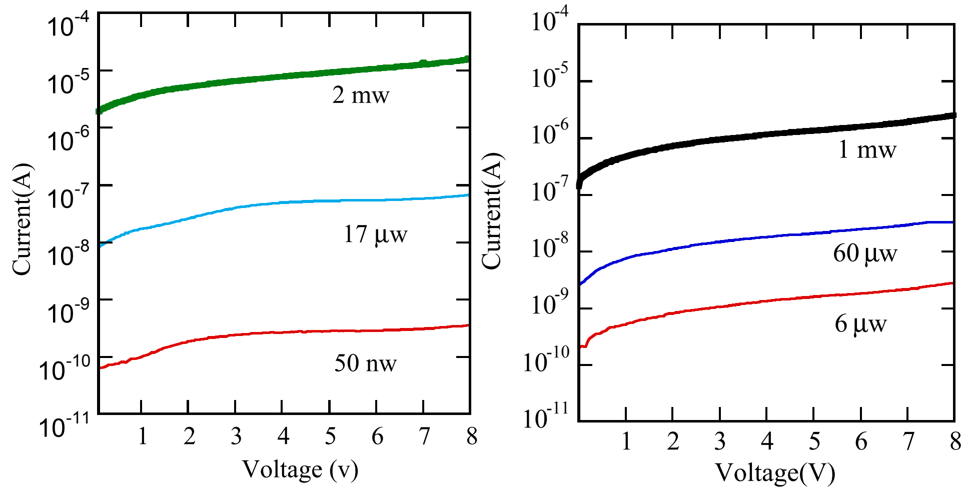

Figure 5.2. The photocurrent with bias at different wavelengths:820nm (left), 1540nm (right)

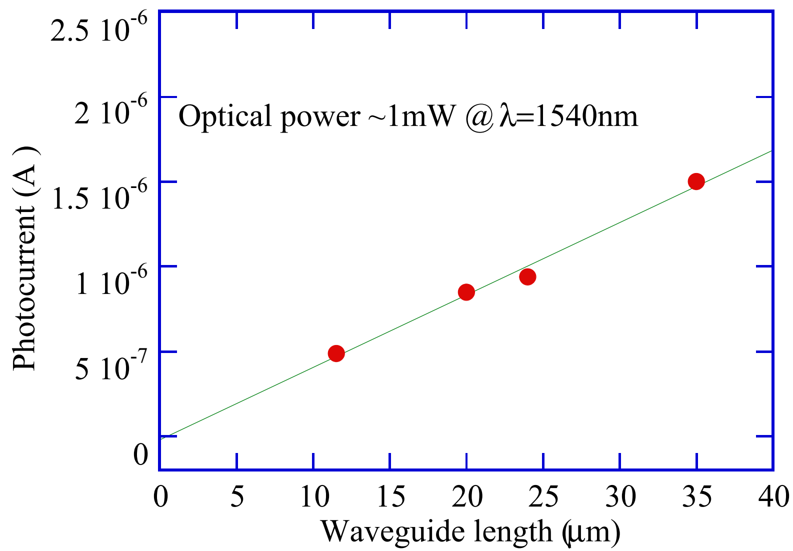

Figure 5.3. The photocurrent with different length.

All the material growth and device fabrication are described in chapter 3. A photodetector with dimensions of $2\mu m$ width, $35\mu m$ length and 170 nm thick

intrinsic region is fabricated. Figure 5.2 plots the photocurrent as a function of the reverse bias at long (1540 nm) and short (820 nm) wavelengths. Three different orders of optical power are used to excite the photodetector. The long wavelength measurement exhibits about one order less photocurrent than the shorter one. As mention in Chapter 4, the 800 nm optical power is almost absorbed below $10\mu m$. That means the absorption length at 1540 nm should be much longer than $35\mu m$. Photocurrents for different lengths of devices are used to extract the optical absorption length. Figure 5.3 plots the photocurrent as a function of waveguide lengths. A linear relation between photocurrent and device lengths indicates that the absorption length is much longer than the device's (equation 5.1). The optical coupling efficiency and the Fresnel reflection between the fiber and waveguide facet are about 10% and 0.3. The carrier lifetime is assumed to be 300 fs (it is based on the results of Chapter 4). Using Equation 5.1 and the data from Figure 5.3, the modal optical absorption is approximately 110 cm^{-1}. The corresponding absorption length is about 100 μm.

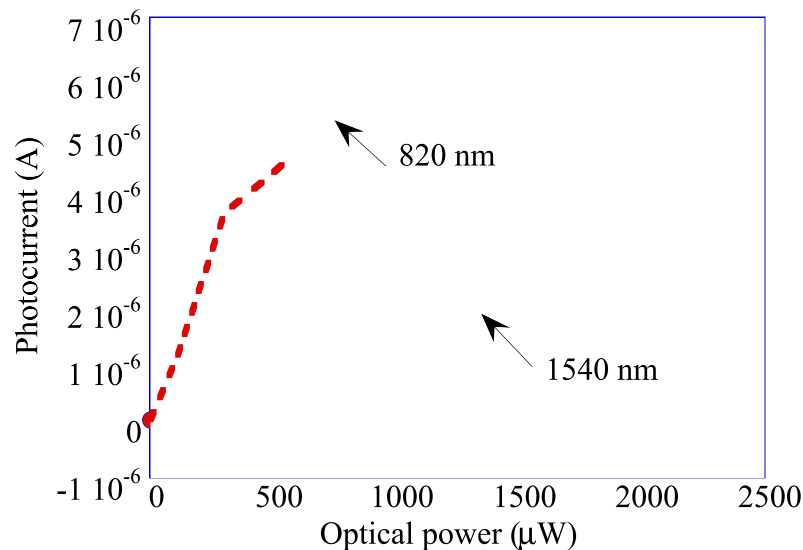

Figure 5.4. Power dependent excitation at 820 nm and 1540 nm

Figure 5.4 shows the D.C. photocurrent at different power levels. In contrast to 820 nm illumination, the photogenerated current at 1540 nm exhibits a non-saturation power above 2 mW (linear relation). The reason for this is that the D.C. saturation problems (e.g. carrier diffusion and high recombination rate) at high pumping power will be diminished due to the low absorption coefficient at long wavelength regime [7].

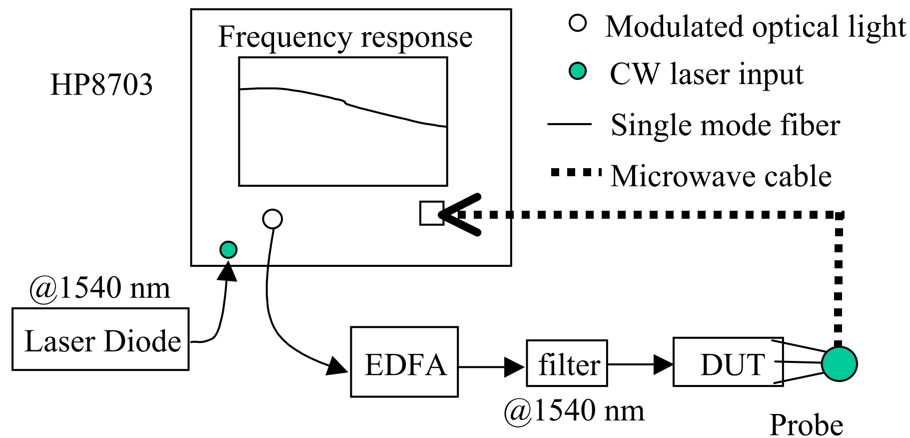

Figure 5.5. Frequency response measurement

In the A.C. performance, Figure 5.5 plots the schematic of the high-speed measurement [8]. An optical component analyzer (HP8703A, 0.13 MHz ~20 GHz) is used to measure the high frequency response. First, the component analyzer, the microwave cable and the single mode fiber are calibrated. The external tunable laser diode is at 1550 nm. After modulation by the component analyzer, the optical light is amplified by an erbium-doped-fiber-amplifier (EDFA) to obtain a higher power. Before edge-coupling into the waveguide, the light source passes through a filter centered at 1550 nm to get rid of some short wavelength light generated by the EDFA, for example 980nm. A Cascade microwave probe with > 40 GHz bandwidth collects the microwave signal.

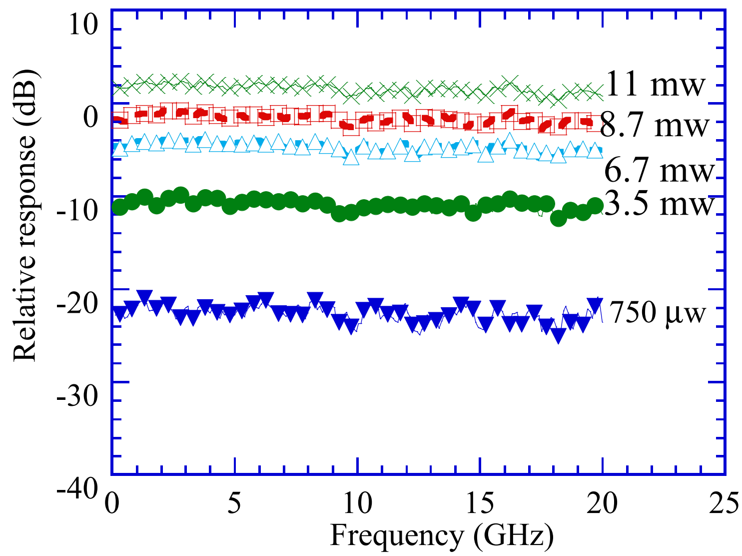

Figure 5.6. Photocurrent frequency response.

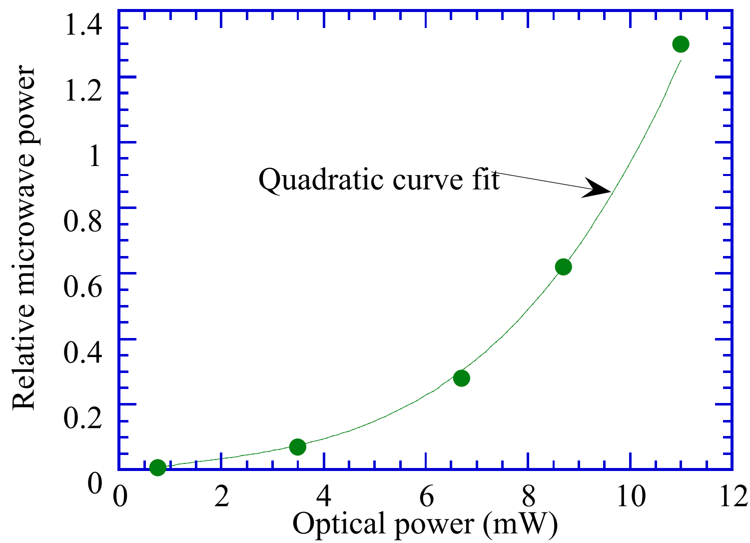

Figure 5.7. The received microwave power with input optical power at 20 GHz

Figure 5.6 shows the photocurrent frequency response of a $35\mu m$ long device. A flat response (only 2 dB variation) is observed from D.C. to 20 GHz. Obviously, the speed is limited by the instrument. An external quantum efficiency of 0.1% is measured. Different power levels of excitation ($0.75 \sim 11 \quad mW$) show

the identical responses. As seen in Figure 5.7, the excitation microwave power reveals a quadratic relation with optical power at 20 GHz, indicating that the photocurrent has a linear dependence on the optical power up to 20 GHz.

In the high-speed performance, the charge screening effects dominate the power saturation problem. The high concentration of charges pumped by high density of optical power will build up an electric field collapsing the applied electric field. Therefore, the response will degrade in high pumping power. Figures 5.6 and 5.7 show that LT-GaAs photodetectors (at long wavelength absorption) inherently have a high saturation power due to the low absorption coefficient.

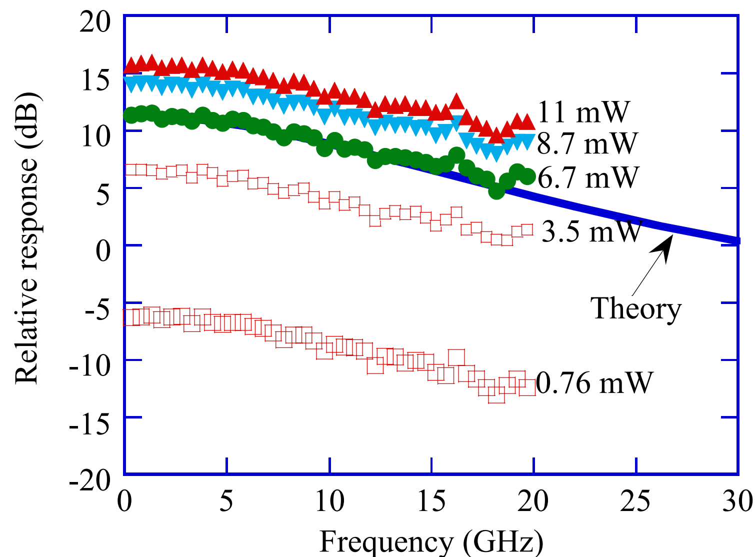

Figure 5.8. The frequency response of 350μm long device

5.2 Long device performance

In the previous section, a device with short length ($35\mu m$) had a bandwidth above 20 GHz, but a low quantum efficiency was obtained. The low efficiency is due to the short waveguide length. To increase the quantum efficiency, a longer waveguide is designed. This photodetector is $2\mu m$ wide and $350\mu m$ long (350 nm thick LT-GaAs). A 1% quantum efficiency is obtained. As seen in Figure 5.8, the

frequency response has around –4 dB rolloff from D.C. to 20 GHz. The solid curve is the theoretical calculation, which agrees quite well with the experimental results. One important fact is that the response for different powers still does not show any nonlinear (power saturation) effects up to 20 GHz.

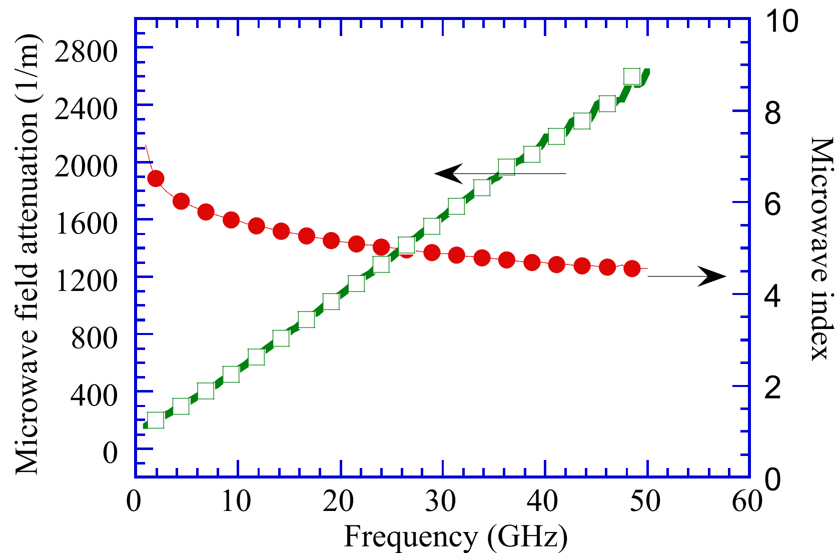

Figure5.9. The microwave field attenuation and index

The distributed photodetector model (in Chapter 2) is used to calculate the total photodetector frequency response. The microwave loss and dispersion of transmission line is included in the model. A 300 fs carrier trapping time is assumed. The calculated response shows little dependence on the carrier trapping effect for a change from 100 fs to 1 ps. This reveals that the trapping time is not the bandwidth-limiting factor.

Let's examine other factors affecting the speed. Figure 5.9 plots the measured microwave loss and dispersion curves. The measured microwave loss has an about 3.5 dB loss at 20GHz for a 350 μm long device. The velocity mismatch factor (v_m / v_o) is about 0.6 at 20 GHz. The optical absorption length is about 100 μm. The pulse broadening by the walk-off problem is around 5 ps

(chapter 2). This indicates that the loss and velocity-mismatch are responsible for high-speed performance in the $350\mu m$ long device.

5.3 Bias dependent efficiency

Photodetector efficiency depends on the ratio carrier trapping time to carrier transit time (Equation 5.1). By applying high enough voltage to saturate the carrier velocity, a general photodetector will get a flat D.C. photocurrent above that bias voltage. As shown in Figure 5.2, the photocurrent in LT-GaAs material shows a considerable dependence on the bias. Since the frequency response has the same speed performance over the applied voltages (carrier trapping limit dominated, Chapter 4, Figure 4.26), the carrier trapping rates should have little dependence on the bias voltage. The reason for causing a bias-dependent photocurrent is the carrier transit time effects, i.e. the carrier velocities in LT-GaAs.

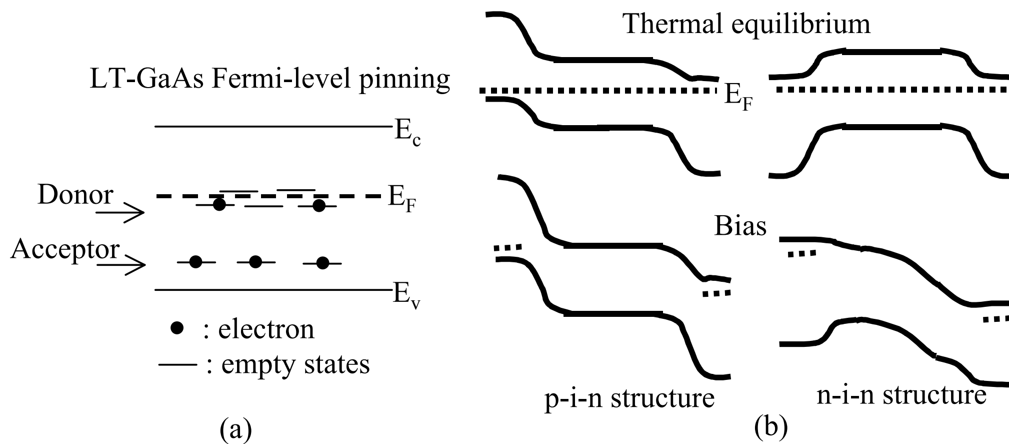

Figure 5.10, (a)LT-GaAs defect model, the deep donors and shallow acceptors force Femi-level pinned near midgap. (b) schematical energy band diagram of p-i-n and n-i-n structure

The slow carrier velocities are mainly due to the low electric fields built in LT-GaAs. A simple model is used to explain this. Figure 5.10(a) shows a schematic diagram of point defects model for the LT-GaAs material [1,2]. Due to excess-As during the growth of LT-GaAs, deep donors (anti-sited As defects) and

shallow acceptors (Ga-vacancy) exist in the material. The midgap donors are partially compensated by the small amount of shallow acceptors so that the Fermi-level is pinned near the midgap. The band diagram for when the LT-GaAs is grown in the p-i-n structure is shown in the figure 5.10 (b) (left). Owing to the Fermi-level pinning, the built-in voltage is almost at the junction of n and p doping side. The p-i-n structure acts like a back-to-back reverse p-n diode. With applied voltage, most of the voltage drop is on the p-i and i-n, so that only small electric field is on the bulk LT-GaAs material. The photocurrent is thus strongly dependent on the bias. To eliminate the problem of LT-GaAs junction, a n-i-n structure is proposed to solve this problem. The schematic band diagram of n-i-n is shown in Figure 5.10(b) (right). The junction n-i resembles a forward bias diode while applying a bias. The voltage on this junction needed is only about 0.7 V. The voltage can thus be efficiently applied on the LT-GaAs material.

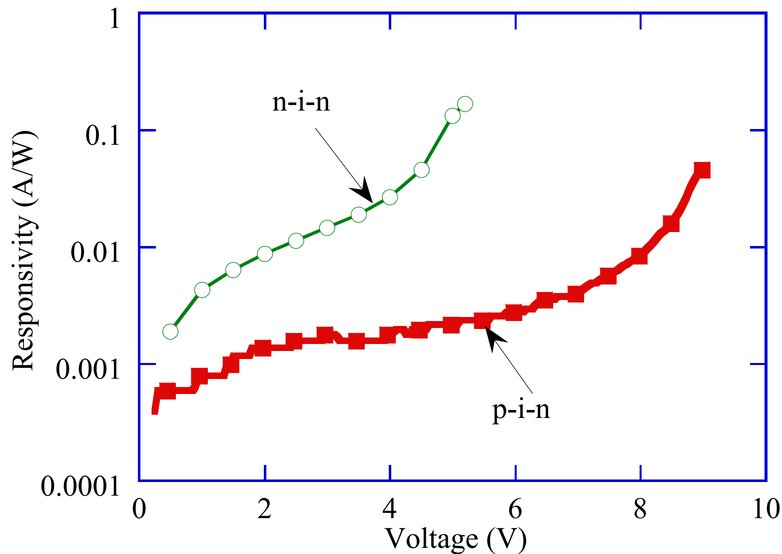

Figure5.11. N-i-n and p-i-n photocurrent responsivity with bias voltage

A p-i-n and n-i-n are compared to examine the difference. The structures have the same material growth and processing except the top contacts and top doped layers (one is n- type, the other is p-type). A 100 nm LT-GaAs layer is

grown. A 3μm wide and 250μm long waveguide structure is fabricated. The D.C. photocurrent is obtained by coupling optical power into the waveguide through a fiber and an optical lens. The responsivity of n-i-n and p-i-n are shown in the Figure 5.11. The significant difference is that the efficiency of p-i-n is about one order less than that of n-i-n. From the optical transmission measurement, the optical coupling loss is around 5 dB yielding the internal quantum efficiency of about 5% at bias 4 V. The A.C. performance is measured by the setup shown in Figure 5.5. Figure 5.12 shows the frequency response. A –3 dB bandwidth of 17 GHz is obtained.

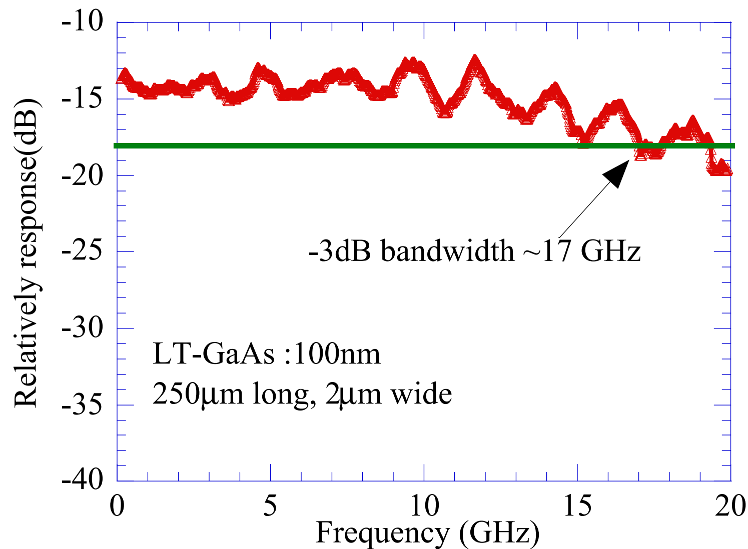

Figure 5.12. Frequency response of n-i-n structure.

5.4. Carrier transport effects at high electric field

The problem of the interface voltage drop between p-GaAs and LT-GaAs (Section 5.3) can be solved by the n-i-n. By using this structure, it is useful for the study of carrier transport in LT-GaAs. Figure 5.13 shows the photocurrent (solid curve) and dark current (dashed curve) of a 3 μm wide and 100 μm long LT-GaAs n-i-n photodetector. The active region (LT-GaAs) is 250 nm thick. The optical wavelength is 1550 nm. Both of the photocurrent current and the dark

current vary a factor of ~10 from 2V to 8 V. The dark current flow of the n-i-n structure has been studied in the reference [2]. In the model of reference [2], the carrier-emission rate increases due to the phonon-assisted tunnel ionization of traps [9] and the Poole-Frenkel effect [10] in the high electric field. The enhanced carrier-emission rate causes the steep increasing of the conduction current at the high electric field.

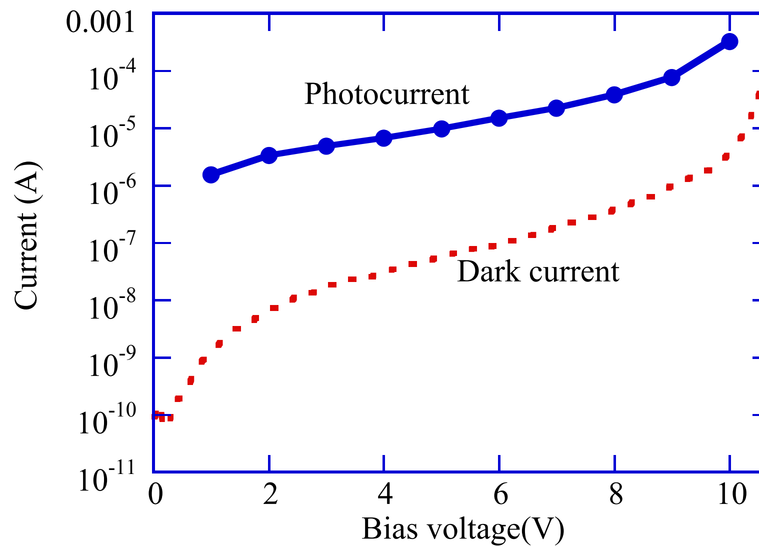

Figure 5.13. The photocurrent and dark current of n-i-n structure.
The i-layer is 250nm thick LT-GaAs.

This model can also explain the behaviors of photocurrent with bias. Equation 5.1 gives the quantum efficiencies of photodetectors. They are three factors that could influence the efficiency. They are (1) optical model absorption coefficient ($\Gamma\alpha$), (2) the carrier transit time and (3) the carrier trapping time. (1) By comparing different lengths of devices, it was found that the optical modal-absorption coefficient ($\Gamma\alpha$) is about 50 μm at the bias of interest (2~8 V), which indicates that the amount of optical light absorbed in the waveguide is the same. (2) The electrical field E_{sat} to saturate the carrier velocity requires about 2.5 V bias (10 kV/cm) [2,11]. The carrier transit time across the intrinsic region is

constant above E_{sat}. (3) Once the electrical field becomes higher, the carrier-effective trapping time becomes longer due to the field-dependent emission rates. Consequently, from the discussion of (1) to (3), the quantum efficiency will increase due to the decreasing of carrier trapping time.

As shown in Figure 5.13, the dark current shows an abrupt rising at about 10.5 V. The speed performance on the bias is measured to examine this effect. Figure 5.14 shows the frequency response at different biases. Below 8 V the n-i-n photodetector exhibits the same behaviors. The flat frequency response shows a high-speed performance similar to Figures 5.8 and 5.12. However, above 8 V, another pole comes out at the frequency ~1 GHz (3 dB drop). The reasons for the abrupt change of D.C. current and the slow response for above 8 V are still not clear. It maybe comes from the carrier multiplication at the high electric fields, so the carrier built-up time limits the frequency response. Probably the processing from the Poole-Frenkel and the phono-enhanced emission effects on the defects limits the speed. Or, the trap filling effect [12] increases the loaded capacitance.

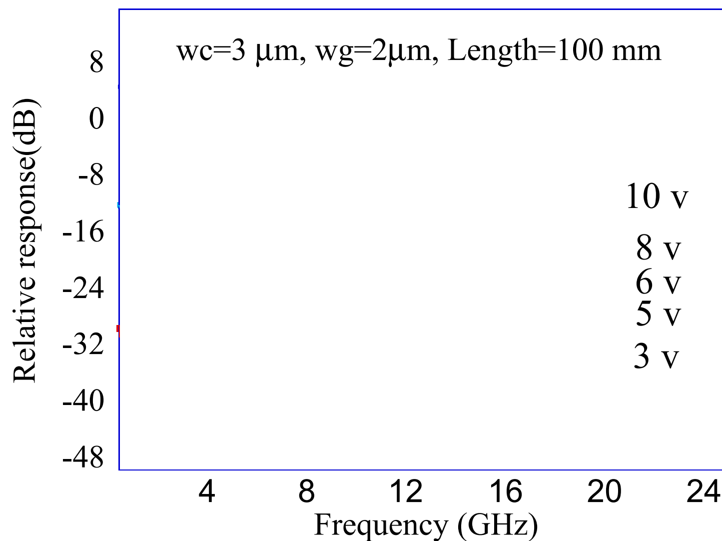

Figure5.14. The frequency response of nin structure at different bias.

5.5 Discussion and Summary:

In this section, the long wavelength detection in LT-GaAs for D.C. and A.C. perfomance is present. The considerably high external-quantum-efficiencies of 0.1% to 5% are obtained in several kinds of WGPD structures. The low efficiency is due to short carrier trapping time and a low absorption coefficient. By increasing the waveguide lengths, the efficiency can be improved by one order (from 0.1% to 1%). The power dependent measurement exhibits that the non-saturation properties of LT-GaAs are due to the low absorption coefficient. This means that a high current level can still be obtained by pumping higher optical power. Comparing to the p-i-n structure, the n-i-n LT-GaAs photodetectors can overcome the problems due to the LT-GaAs junctions.

Reference:

[1] Look, D.C. 'On compensation and conductivity models for molecular-beam-epitaxial GaAs grown at low temperature'. Journal of Applied Physics, vol.70, (no.6), 15 Sept. 1991. p.3148-51.

[2] Ibbetson, James, 'Electrical characterization of nonstoichiometric GaAs grown at low temperature by Molecular Beam Epitaxy'. University of California, Santa Barbara CA. Ph.D. dissertation March 1997.

[3]Warren, A.C.; Woodall, J.M.; Freeouf, J.L.; Grischkowsky, D.; McInturff, D.T.; Melloch, M.R.; Otsuka, N. 'Arsenic precipitates and the semi-insulating properties GaAs buffer layers grown by low-temperature molecular beam epitaxy'. Applied Physics Letters, vol.57, (no.13), 24 Sept. 1990. p.1331-3.

[4] Srinivasan, A.; Sadra, K.; Campbell, J.C.; Streetman, B.G. 'Influence of growth temperatures on the photoresponse of low temperature grown GaAs:As p-i-n diodes'. Journal of Electronic Materials, vol.22, (no.12), Dec. 1993. p.1457-9.

[5] Warren, A.C.; Burroughes, J.H.; Woodall, J.M.; McInturff, D.T.; Hodgson, R.T.; Melloch, M.R. '1.3- µm P-i-N photodetector using GaAs with As precipitates (GaAs:As)'. IEEE Electron Device Letters, vol.12, (no.10), Oct. 1991. p.527-9.

[6] Grenier, P.; Whitaker, J.F. 'Subband gap carrier dynamics in low-temperature-grown GaAs'. Applied Physics Letters, vol.70, (no.15), AIP, 14 April 1997. p.1998-2000.

[7] Dankowski, S.U.; Kiesel, P.; Knupfer, B.; Dohler, G.H.; Keil, U.D.; Dykaar, D.R.; Kopf, R.F. 'Annealing induced refractive index and absorption changes of

low-temperature grown GaAs ‘. Applied Physics Letters, vol.65, (no.25), 19 Dec. 1994. p.3269-71.
[8] Thanks to Sheng Z. Zhang for helping setup the measurement.
[9] Makram-Ebeid, S.; Lannoo, M. ‘Quantum model for phonon-assisted tunnel ionization of deep levels in a semiconductor’. Physical Review B (Condensed Matter), vol.25, (no.10), 15 May 1982. p.6406-24.
[10] J.L. Hartke, ‘The 3-dimensional Poole-Frenkel effects’. Journal of Applied Physics, 39, pp4871-5, 1968.
[11]S.M. Sze, ‘Physics of Semiconductor Devices’. 2nd edition.
[12]M.A. Lampert and P. Mark, ‘ Current injetion in solids’. New York, Academic press 1970.

This page is intentionally left blank.

Chapter 6

Conclusion

A novel low-temperature grown GaAs (LT-GaAs) p-i-n traveling-wave photodetector (TWPD) has been successfully designed, fabricated and measured. A distributed photodetector model is used to optimize and design the traveling wave structure. The measured electro-optic sampling results reveal that this kind of traveling wave photodetector is limited only by carrier-trapping time in LT-GaAs. A record bandwidth (560 GHz) is demonstrated.

Long wavelength absorption has been measured in the LT-GaAs material due to the midgap defects and As precipitates. A long waveguide photodetector is fabricated to enhance the quantum efficiency. A 1% efficiency is obtained. Long-wavelength absorption and high-speed (above 20 GHz) GaAs-based photodetector was also demonstrated.

6.1 Summary

The interest in fabricating a LT-GaAs traveling-wave photodetector originates from the transit-time limitation of the conventional photodetectors. The transit time across the intrinsic region is inherently related to the geometry of the photodetectors. The inevitable trade-off between the transit-time limitation and the RC-response in either vertical-illumination or waveguide structures makes it hard to surpass 200 GHz bandwidth for GaAs or InGaAs material. One alternative choice is using LT-GaAs material. The material response will be dominated by the high carrier recombination rate in LT-GaAs instead of carrier transit time. The transit time limit is eliminated. The material and circuit responses can be optimized independently.

Traveling-wave photodetectors (TWPD) are one kind of waveguide photodetectors (WGPD). In TWPDs, the waveguide impedance should match the

load circuit to minimize the microwave reflection at the boundaries. The RC roll-off frequency can thus be avoided. In contrast to top-illumination devices, the total photocurrent response is collected by the fully distributed photodetectors excited by optical wave traveling along the transmission line. The optimum performance is when the optical velocity matches the microwave velocity.

A distributed photodetector model is analyzed to realize the TWPD performance. An equation in the frequency domain is used to describe the distributed effect, in which the optical and microwave loss and dispersion, and the reflection in the optical input are involved. An equivalent circuit model is applied to calculate the microwave propagations in the hybrid-coplanar waveguides. The bandwidth limitations for velocity mismatch, microwave loss and reflection effects are discussed. It is found that the highest bandwidth is achieved not only when velocity and impedance are matched, but also when the microwave loss is least.

In the circuit and material design, the distributed photodetector model is used to optimize the waveguide geometry. Considering the material and the microwave propagation, one microwave wide waveguide is found to be the best choice. A 170 nm thick depletion region (LT-GaAs) is determined by optimizing the bandwidth-efficiency product.

A 530 fs FWHM of impulse response is obtained and the corresponding –3dB bandwidth is 560 GHz. By the power and bias dependent measurement, the high-speed performance is found to be carrier trapping limited in LT-GaAs.

Long wavelength (1300nm~1550nm) absorption was measured in the D.C. and A.C. characteristics. A quantum efficiency of 1% was obtained in a $350\mu m$ long device. An 18 GHz bandwidth was measured in this device. The calculation by the distributed photocurrent model reveals that the bandwidth is due to microwave loss in long device.

6.2 Future work

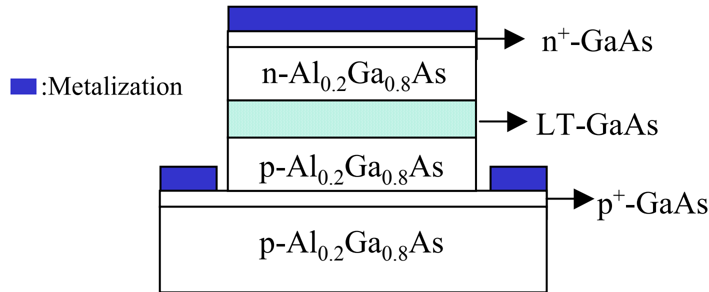

Figure 6.1. Insert a thin p^+-GaAs on the bottom p-cladding layer for improving ohmic contact.

6.2.1 Contact resistance

As discussed in the Chapter 4, microwave loss plays an important role in the performance of two different lengths of device. In the transmission line, an ohmic contact resistance problem will cause some bandwidth penalties. As seen in the contact resistances of the Table 4.1, the contact resistance for only 20% of Al in AlGaAs results in about 6 times the contact resistance of GaAs contact. To reduce the contact resistance, one possible structure involves inserting a thin $p^+ - GaAs$ layer to the bottom p-type AlGaAs layers, as shown in Figure 6.1. References [1-5] show other ways to improve the contact resistance. By using the tunneling conduction through the midgap defects of LT-GaAs [1] or growing the InGaAs strain layers [2,3], the nonalloy ohmic contacts can be achieved. The nonalloy-ohmic contacts have smooth metalization, so the metal spiking due to annealing can be avoided. And also, the microwave loss from the rough metal surface and the high contact resistance could be reduced. Heavy carbon doping can be used in AlGaAs material to get a very low p-contact resistance [4,5]. The low-diffusion carbon can allow the high temperature growth to get high quality material. The carbon doping may solve the problems arisen from the Be-doped p-material.

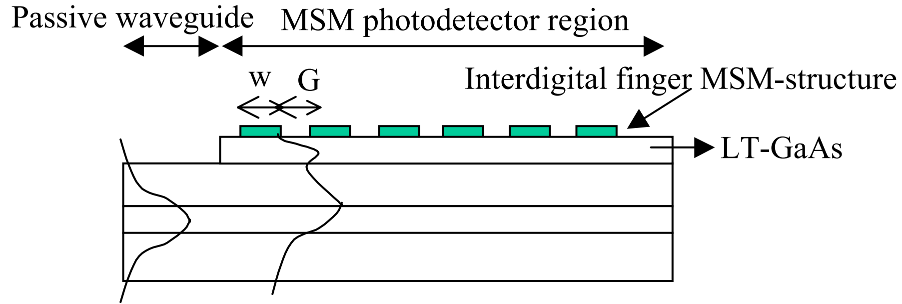

Figure6.2. Schematic diagram of distributed MSM photodetector

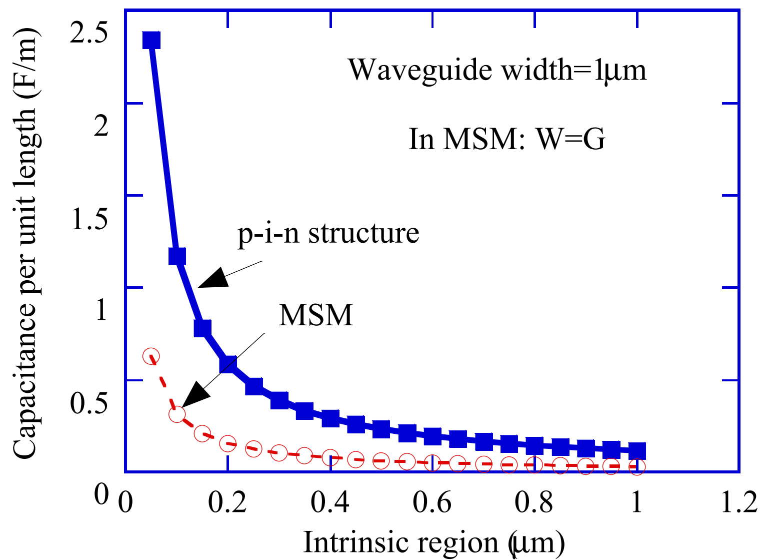

Figure 6.3. Loaded capacitance of p-i-n and MSM.
The intrinsic region of p-i-n is the same as MSM finger gap (G)

6.2.2 MSM structure

The drawbacks of p-i-n structure are the high microwave loss and velocity mismatch, because of the highly confined electric field inside the intrinsic region and the n- and p- doped material. Another way to decrease the microwave loss is to use a different waveguide structure. MSM photodetectors have been shown to have a potential for obtaining high bandwidth in theory or experiment [8-11]. In contrast to the p-i-n structure, MSM structures inherently have low capacitance. Figure 6.2 shows a schematic MSM waveguide photodetector, which has two sections, passive

waveguide and MSM-detector regions. The passive waveguide is designed for optimizing the optical coupling efficiency.

Figure 6.3 plots the calculated loaded capacitance per unit length of p-i-n structure (intrinsic capacitance) and MSM (interdigital finger capacitance) [8]. The waveguide width is set as $1\mu m$. It is assumed that the same carrier transit time in both structures (intrinsic region thickness in p-i-n = electrode gap in MSM digital fingers). And the same electrode gap and width (W=G) are set in the MSM structure. The MSM structure, as shown, shows a lower capacitance than the p-i-n structure. It indicates that the MSM might have better microwave propagation properties than p-i-n structure. In the point view of fabrication, the isolation process, metal contact annealing and the polyimide passivation can be avoided in the MSM structure. Therefore, the traveling wave MSM structure might have a high potential for high-speed application.

6.2.3 the reflection in the optical input end:

The ideal TWPD should not have reflection in the boundaries of waveguide. As discussed in Chapter 4, the reflection wave at the optical input end reveals some effects on the detector speeds. Figure 6.4 shows a possible solution to eliminate the impedance mismatching. The optical waveguide is divided two sections, a passive waveguide and p-i-n photodetector section (similar to Figure 6.2). The passive waveguide is used for obtaining high coupling efficiency and also supporting a space for bridging the load circuit B. The load circuit B can decrease the reflection wave. Reference [12] has shown the similar structure for traveling wave EA-modulator and obtained good results.

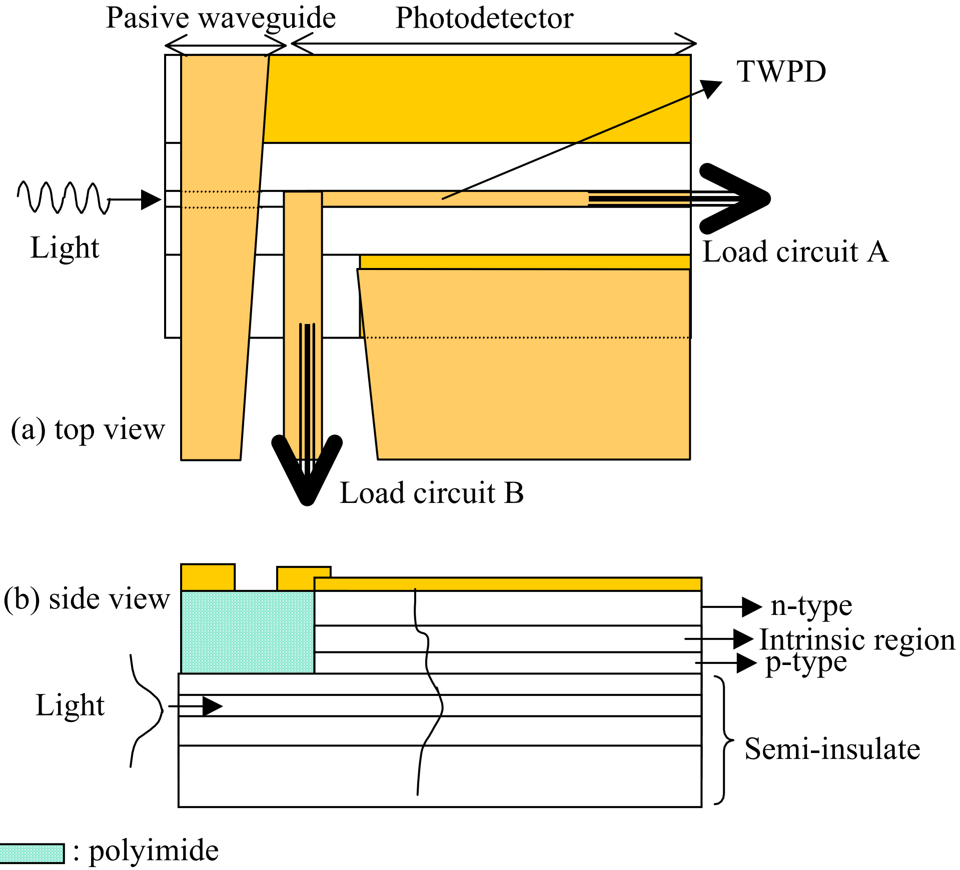

Figure6.4. The schematic of load circuit to eliminate the reflection from optical input

The passive waveguide region (Figures 6.2, 6.4) increases more flexibility in the designing the high-speed performance. Rather than matching the impedance at the optical input end, the load-circuit B (Figure 6.4) can be possibly made with lower impedance than the waveguide's one. The anti-resonate effect (a 180^0 phase shift at optical input end) can diminish the long tail of the optical impulse. Figure 6.5 plots the calculation of the influence on the load-circuit of the input end. The waveguide design is the same as the one in the Chapter 3. The open (reflection=1, triangle curve) and match (refltion=0, thin solid curve) cases reveal only a little change in the speed performance. However, if putting the low-impedance load, the optical pulses (circle and thick solid) are sharpened. Especially, when the load is short circuit (reflection=-1), the electrical pulse exhibits a sinusoid-like oscillation

with a half pulsewidth in the case of impedance-match. Using this concept, the microwave generation above the THz radiation may be possible.

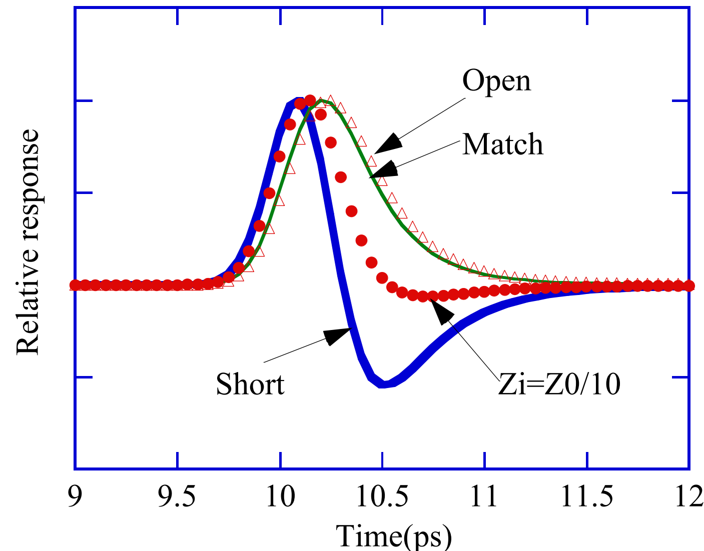

Figure6.5. The input resistance effects on the response.

6.3 Application

Figure 6.6 [15] plots the historical trends of optical fiber communications. Using WDM and OTDM techniques, the optical fiber communications show a tremendous growth in the channel bit rate (from the bit rate of 10 Mb/s in 1980's to 3 Tb/s in 1999's OFC conference). The photodetectors of bandwidth higher 100 GHz or even 1 THz are needed. The performance of high-speed photodetectors operated at the carrier-transit time regime is hard to overcome the 200 GHz barrier. However, the LT-GaAs TWPDs offer a significant advantage for the receivers above 500 GHz bandwidth. Although the efficiency is low due to the carrier trapping limitation, the high saturation power of LT-GaAs can compensate this. Also, the integration of optical amplifier with photodetector [13] or the high speed microwave amplifier with > 400GHz of f_{max} [14] make the implementation of receivers with above 500 GHz bandwidth plausible.

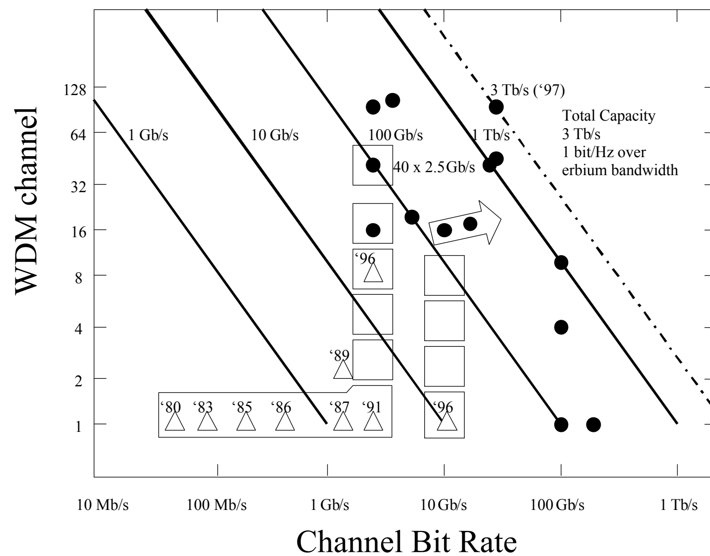

Figure 6.6. The historical trend of WDM channel with the Bit Rate since 1980

Reference:

(1)Woodall, J.M.; Janes, D.B.; Patkar, M.P. (Edited by: Scheffler, M.; Zimmermann, R.) 'Better Ohmic contacts and more device functionality through heavy doping'. 23rd International Conference on the Physics of Semiconductors, (vol.4) 1996. p.3259-66.

(2)Kumar, N.S.; Chyi, J.-I.; Peng, C.K.; Morkoc, H. 'GaAs metal-semiconductor field-effect transistor with extremely low resistance nonalloyed ohmic contacts using an InAs/GaAs superlattice '. Applied Physics Letters, vol.55, (no.8), 21 Aug. 1989. p.775-6.

(3)Nittono, T.; Ito, H.; Nakajima, O.; Ishibashi, T. 'Extremely low resistance non-alloyed ohmic contacts to n-GaAs using compositionally graded in $In_xGa_{1-x}As$ layers '. Japanese Journal of Applied Physics, Part 2 (Letters), vol.25, (no.10), Oct. 1986. p.L865-7.

(4)Katz, A.; Abernathy, C.R.; Pearton, S.J.; Weir, B.E.; Savin, W. 'Ohmic contacts to heavily carbon-doped p-$Al_xGa_{1-x}As$'. Journal of Applied Physics, vol.69, (no.4), 15 Feb. 1991. p.2276-9.

(5)Katz, A.; Abernathy, C.R.; Pearton, S.J. 'Pt/T ohmic contacts to ultrahigh carbon-doped p-GaAs formed by rapid thermal processing'. Applied Physics Letters, vol.56, (no.11), 12 March 1990. p.1028-30.

(6)Bottcher, E.H.; Bimberg, D. Millimeter wave distributed metal-semiconductor-metal photodetectors. Applied Physics Letters, vol.66, (no.26), 26 June 1995. p.3648-50.

(7)Kollakowski, S.; Bottcher, E.H.; Lemm, C.; Strittmatter, A.; Bimberg, D.; Krautle, H. 'Waveguide-integrated InP-InGaAs-InAlGaAs MSM photodetector

with very-high vertical-coupling efficiency'. IEEE Photonics Technology Letters, vol.9, (no.4), IEEE, April 1997. p.496-8.
(8)Y.C. Lim and R.A. Moore, ' Properties of alternately charged coplanar parallel strips by conformal mapping'. IEEE Trans. Electron Devices, vol-15, pp173-180, 1968.
(9)Bottcher, E.H.; Bimberg, D. 'Millimeter wave distributed metal-semiconductor-metal photodetectors'. Applied Physics Letters, vol.66, (no.26), 26 June 1995. p.3648-50.
(10)Ersoni, M.; Xiucheng Wu; Jessop, P.E.; Noad, J.P. 'Optical signal distribution in waveguide-coupled metal-smiconductor-metal detector arrays'. Journal of Lightwave Technology, vol.15, (no.2), IEEE, Feb. 1997. p.328-33.
(11)Chou, S.Y.; Liu, M.Y. 'Nanoscale tera-hertz metal-semiconductor-metal photodetectors'. IEEE Journal of Quantum Electronics, vol.28, (no.10), Oct. 1992. p.2358-68.
(12)Zhang, S.Z.; Yi-Jen Chiu; Abraham, P.; Bowers, J.E. '25 GHz polarization-insensitive electroabsorption modulators with traveling-wave electrodes'. IEEE Photonics Technology Letters, vol.11, (no.2), IEEE, Feb. 1999. p.191-3.
(13)Wake, D. 'A 1550-nm millimeter-wave photodetector with a bandwidth-efficiency product of 2.4 THz '. Journal of Lightwave Technology, vol.10, (no.7), July 1992. p.908-12.
(14)Lee, Q.; Agarwal, B.; Mensa, D.; Pullela, R.; Guthrie, J.; Samoska, L.; Rodwell, M.J.W. 'A>400 GHz f_{max} transferred-substrate heterojunction bipolar transistor IC technology'. IEEE Electron Device Letters, vol.19, (no.3), IEEE, March 1998. p.77-9.
(15) The plot is taken from the class notes of Prof. John Bowers.